University of Trento
Department of Physics

Thesis
Submitted to the
Doctoral School in Physics
by

Matteo Leonardi

In candidature for the degree of
Philosophiae Doctor - Dottore di ricerca

Development of a squeezed light source prototype for Advanced Virgo

Tutor: Prof. Giovanni Andrea Prodi

Co-Tutor: Prof. Jean-Pierre Zendri

XXVIII PhD cycle
Academic year 2015/2016

Contents

Introduction

A century after the prediction of the existence of gravitational waves by A. Einstein and after over fifty years of experimental efforts, gravitational waves have been detected at Earth directly [1, 2]. This result is a major achievement and opens new prospectives for the exploration of our universe. Gravitational waves carry different and complementary information about the source with respect to electromagnetic signals. In particular the first detection demonstrated the existence of stellar-mass black holes, binary systems of black holes and their coalescence.

The detection was made by the LIGO instruments which are twin kilometer-scale Michelson interferometers in the US. These detectors represent the second generation of gravitational wave interferometers and, for the first time, they achieved the outstanding strain sensitivity of $10^{-23}\mathrm{Hz}^{-1/2}$ between 90 Hz and 400 Hz. In the next months the LIGO network will be joined by another second generation detector: Advanced Virgo located near Pisa, Italy. The sensitivity of these advanced detectors is set by different noise sources. In particular, in the low frequency range (below 100 Hz) major contributions come from thermal noises, gravity gradient noise and radiation pressure noise; instead, the high frequency band (above $100 - 200$ Hz) is dominated by shot noise. Quantum noise (radiation pressure and shot noise) is expected to dominate the detector sensitivity in the whole frequency band at the final target laser input power.

To decrease the shot noise while increasing the radiation-pressure noise, or vice-versa, Caves [3] proposed in 1981 the idea of the *squeezed-state technique*. The LIGO collaboration demonstrated for the first time in 2011 [4] that the injection of a squeezed vacuum state into the dark port of the interferometer can reduce the shot noise due to the quantum nature of light. This result was achieved with the German-British interferometer GEO600 and was replicated in 2013 with the LIGO interferometer at Livingston [5]. After these results, the LIGO collaboration have pursued further the research in the squeezed-state technique [6, 7, 8] which is considered mandatory for third generation of ground based interferometric detectors.

In 2013, the Virgo collaboration started developing the squeezed-state technique. The subject of my thesis is the realization of a prototype of frequency independent squeezed vacuum state source to be injected in Advanced Virgo. This prototype is developed in collaboration with other Virgo groups.

This thesis is organized as in the following. In Chapter 1 I give an overview of gravitational wave and ground based interferometric detectors. In Chapter 2 I summarize the results of the theory of non linear optics of interest for the development of a squeezed vacuum source for Advanced Virgo. In chapter 3 I discuss the expected Advanced Virgo performances including the use of squeezed-state technique. In the second part of this work I describe my experimental work: in Chapter 4 I describe the prototype under development, in Chapter 5 the second harmonic generator and in Chapter 6 the Faraday isolator.

Part I

Theory

The darker the night,
the brighter the stars.
Crime and Punishment,
Fyodor Dostoevsky, 1866

Chapter 1

Gravitational wave and detectors

This chapter provides a brief introduction to gravitational waves (GW) and to the main GW sources accessible by ground based detectors. The second part reviews the optical-interferometric detectors for GW, focusing in particular on Advanced Virgo (AdV).

1.1 Gravitational waves

Gravitational waves are ripples in the space time. They are a special solution of the Einstein equations for weak gravitational field.

The Einstein equations can be written as (see [9]):

$$R_{ik} - \frac{1}{2} g_{ik} R = \frac{8\pi G}{c^4} T_{ik} \tag{1.1.1}$$

or alternatively

$$R_{ik} = \frac{8\pi G}{c^4} \left(T_{ik} - \frac{1}{2} g_{ik} T \right) \tag{1.1.2}$$

where R_{ik} is the Ricci curvature tensor, g_{ik} is the metric tensor, G is the Newton's gravitational constant, T_{ik} is the stress-energy tensor, R is the scalar curvature and $R_i^i = R = -\frac{8\pi G}{c^4} T$ with $T = T_i^i$.

In the vacuum space, $T_{ik} = 0$ and the Einstein equations reduce to

$$R_{ik} = 0 \tag{1.1.3}$$

Having a weak gravitational field means that the metric tensor can be expressed as a small perturbation to the Minkowski metric η_{ik}:

$$g_{ik} = \eta_{ik} + h_{ik} \tag{1.1.4}$$

where h_{ik} is the small perturbation. In this situation of weak gravitational field,

$$R_{ik} = \frac{1}{2} \Box h_{ik} \tag{1.1.5}$$

where $\Box$ is the D'Alembert operator: $\Box = -\eta^{lm} \frac{\partial^2}{\partial x^l \partial x^m} = \Delta - \frac{1}{c^2} \frac{\partial^2}{\partial t^2}$ Considering eq(1.1.5) with eq(1.1.3), choosing the Lorenz gauge and the transverse traceless gauge, we find

$$\Box h_{ik} = 0 \tag{1.1.6}$$

This equation is formally equivalent to the electromagnetic wave equation. Gravitational fields, like electromagnetic fields, propagate at the speed of light. Their properties can be derived from eq(1.1.6). All the details can be found in any general relativity textbook [9].

The gravitational waves are transverse waves which polarization is defined by a symmetric rank two tensor . The two polarization are usually identified as h_+ and $h_\times$; these differ from each other by a $\pi/4$ rotation in the plane perpendicular to the propagation direction.

Gravitational waves are emitted by accelerated masses. The lowest multipole term which can radiate a gravitational wave is the quardupole term. This means that mass distributions that exhibit a spherical symmetry cannot radiates GWs.

Examples of GWs sources of interest to ground based detectors are:

- **Compact binary systems:** [10] these systems are formed by two compact stars such as neutron stars or black holes orbiting around their center of mass. As demonstrated by Hulse and Taylor on a binary neutron star pulsar system, PSR B1913+16, massive binary rotating systems lose energy via GW radiation [11, 12, 13]. Up to coalescence, the frequency and the amplitude of the emitted GW increase as the orbit radius decrease. This results in a chirp signal.

- **Spherical asymmetric spinning massive objects:** these objects can be non-symmetric pulsars and neutron stars. The expected GW signal from this source is a continuous signal, whose frequency is proportional to the source rotating frequency. The GW signal strength increases as the degree of axial-asymmetry increases.

- **Stochastic background:** [14] in analogy to cosmic microwave background (CMB), also a cosmic gravitational wave background is expected as remnant of the Big Bang. Unlike the CMB that gives information of approximately 300000 years after the Big Bang, the stochastic background can give information from about 10^{-36}s after the Big Bang. In addition other GW backgrounds are expected from the overposition of many astrophysical emitters.

- **Supernovae:** [15, 16] stellar explosions that are not spherical symmetric are predicted to emit GWs.

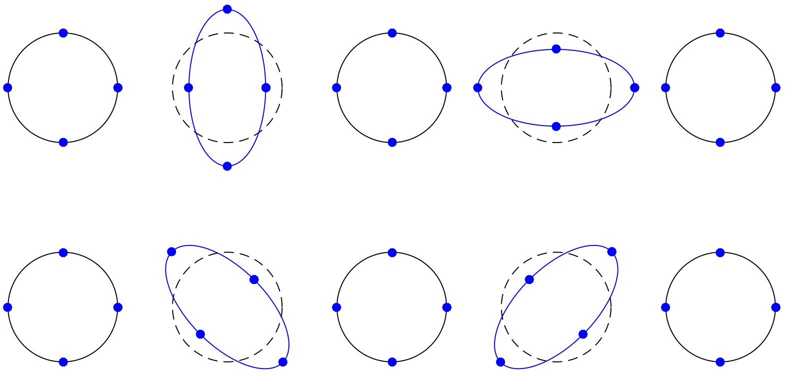

Figure 1.1: Effect of the two GW polarization on two rings of free falling test particles. The top strip shows the effect of an h_+ polarized GW while the bottom one shows the effect of an $h_\times$ polarized GW. In both cases the GW propagation direction is perpendicular with respect to the test masses ring plane. The horizontal axis is the phase of the GW with $\pi/2$ phase intervals.

The effect of a gravitational wave on an extended body is a modification of the relative distances between different positions. Fig.1.1 shows the effect of the two polarisations (h_+ and $h_\times$) of a passing gravitational wave on two rings of free-falling test particles.

The strength of a GW is usually measured in strain, that is the fractional length change it induces:

$$h = \frac{\delta L}{L} \tag{1.1.7}$$

where δL is the length variation induced by the GW and L is the original length. The largest astrophysical events are expected to have strains of the order of $h = 10^{-21}$.

1.2 GW detector: Advanced Virgo

The GW ground based detectors that have the highest sensitivity are the GW interferometric detectors. These detectors are based on the Michelson interferometer design.

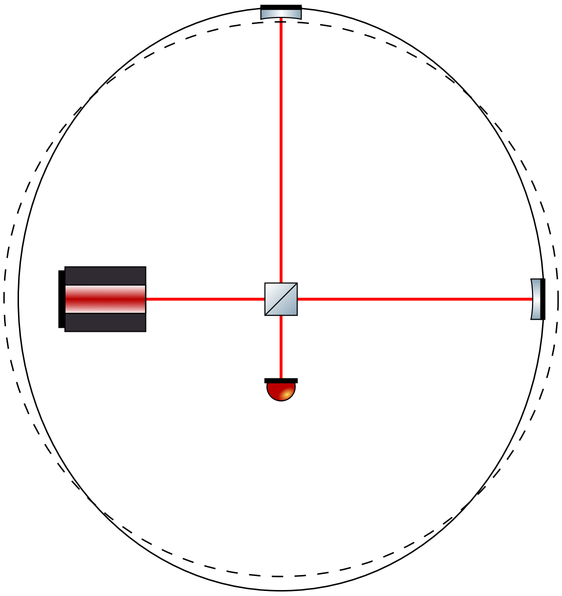

Figure 1.2: Basic scheme of a Michelson interferometer. The laser light is splitted at the beamsplitter and then, after traveling through the arms, it's recombined again at the beam splitter. The light detected at the photodetector carries the information of the relative displacement of the two end mirror. In this case, the two end mirrors are displaced by an h_+ polarized GW.

Fig.1.2 shows the basic scheme of a Michelson interferometer. The two end mirrors are displaced due to the passage of an h_+ polarized GW. The light detected at the photodetector carries the information of the relative displacement δL of the two mirrors.

To increase the sensibility to GW of a basic Michelson interferometer, several upgrades can be implemented: two Fabry-Perot cavities are inserted along the arms of the interferometer, a power recycling mirror is placed between the laser and the beam splitter and a signal recycling mirror is placed between the beam splitter and the photodetector. Moreover, an input mode cleaner (realized with a triangular cavity) is used to clean the input light frequency before injecting in the interferometer and, at the output, just before the photodetector, an output mode cleaner cleans the beam from spurious TEM modes and from control sidebands. Fig.1.3 shows the basic scheme of a GW interferometer.

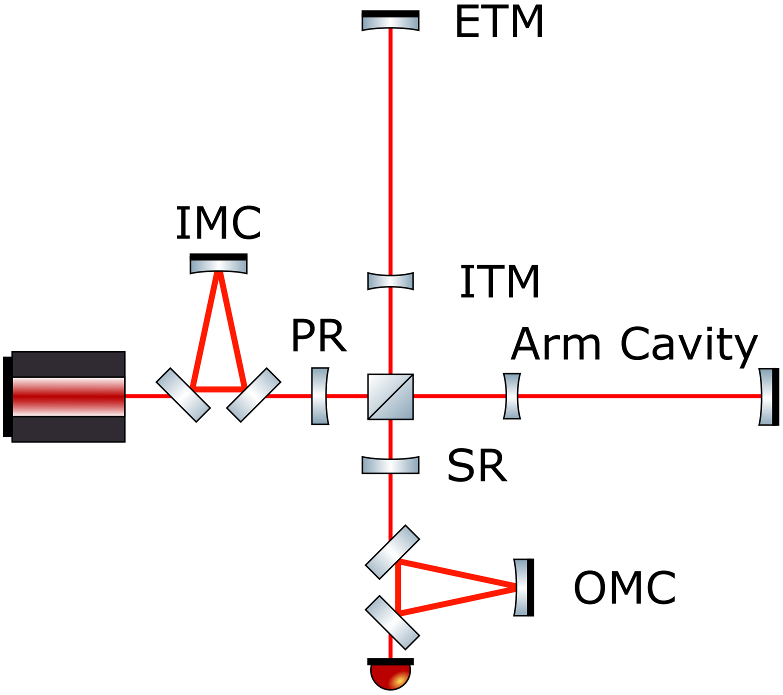

Figure 1.3: Basic scheme of a GW interferometric detector. In the figure IMC is the input mode cleaner, PR is the power recycling mirror, SR the signal recycling mirror, OMC is the output mode cleaner and each arm cavity is formed by the input test mass (ITM) and the end test mass (ETM). The length of the arm cavity is $L_{arm} \approx 3$ km for AdV and $L_{arm} \approx 4$ km for the two aLIGO.

In the near future, the network of ground based GW interferometric detectors will comprise the two LIGO detectors (LIGO Livingston and LIGO Hanford, both in the US), the Virgo collaboration detector (near Pisa, Italy), KAGRA detector (in Japan, at Kamioka), GEO-HF (near Hannover, Germany) and LIGO-India (joint India-US detector recently approved). Last year, in September, the first two second generation GW detectors (the two LIGO) started collecting science data, showing a strain sensitivity of $\approx 10^{-23}/\sqrt{\text{Hz}}$ within $100-500$Hz. The italian-french AdV detector is currently under construction and will join the world wide network before the end of this year.

In the following I detail the sensitivity curve expected for AdV pointing out the major noise sources. All the details of the following discussion can be found in [17, 18].

AdV is expected to reach the design sensitivity of $\approx 3 \times 10^{-24}/\sqrt{\text{Hz}}$ between $50-400$Hz. To reach this goal, a four steps upgrade process is planned by implementig the following configurations:

- power recycled, $P_{in} = 25$ W;
- dual recycled, $P_{in} = 25$ W, tuned signal recycling;
- dual recycled, $P_{in} = 125$ W, tuned signal recycling;

- dual recycled, $P_{in} = 125$ W, detuned signal recycling.

The input power P_{in} is measured after the IMC and *dual recycled* refers to the presence of both the PR and the SR mirrors.

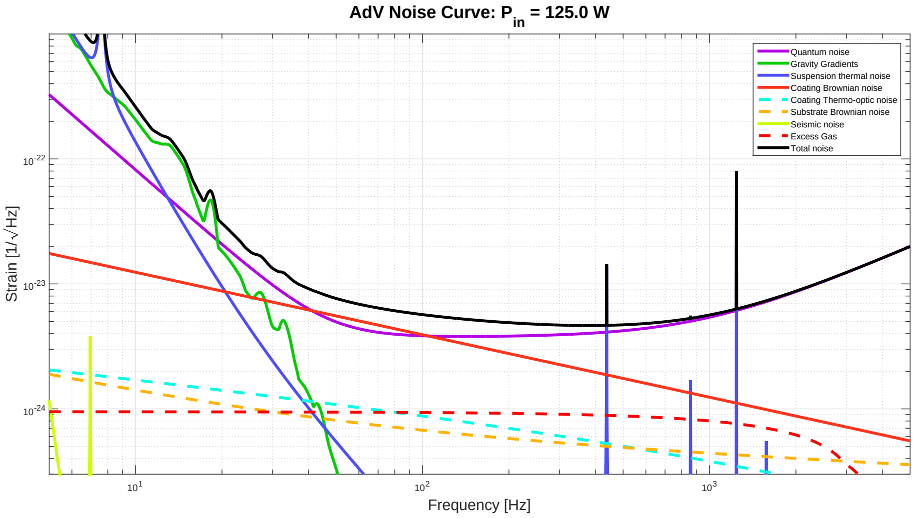

Figure 1.4: Dual recycled AdV noise curve with 125 W input power and tuned SR mirror. The simulation is performed using GWINC code.

Fig.1.4 shows an example of the expected noise budged of a dual recycled AdV with 125 W input power and tuned SR mirror. The sensibility of the GW detector is limited by several noise source for different frequency ranges.

Thermal noise

A motion of the reference surface of the test masses due to brownian motion can mimic the signal of an incoming GW. The two most limiting noises within this class are the coating brownian thermal noise and the suspension thermal noise (see Fig.1.4). The first arises from the brownian noise of the test masses coating, while the second is mainly due to the silica fibers that suspend the input test masses (ITMs) and the end test masses (ETMs). This noise can be reduced either improving the quality of the coating and fiber materials or heading to low temperature operations. Additional thermal noise sources come from thermo-optical processes in the coating, Brownian motion of the mirror substrate, thermo-elastic processes of the substrate and thermo-refractive processes in the output mode cleaner (OMC).

Seismic noise

Fig.1.5 shows the seismic noise of the central building floor (near the beam splitter) of AdV during the science run VSR4. This noise must be reduced usign seismic filtering stages. The AdV collaboration developed a passive multistage seismic attenuator (superattenuator or SAT) that attenuates the seismic motion by 140dB above 3Hz.

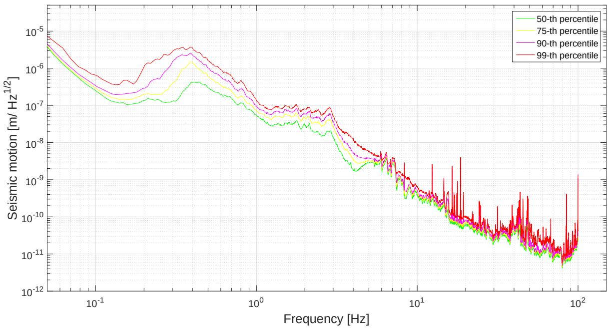

Figure 1.5: Horizontal ground motion measured on the floor of the AdV central building during science run VSR4 (see [19]) in the West direction.

Gravity gradient noise

This noise arises from the Newtonian gravitational attraction between masses, in particular between the detector test masses and nearby moving masses. Those moving masses can be either people, cars, trains, etc and also environmental density changes (e.g. atmospheric pressure, subterranean sediment settlement). This is one of the most tricky noise source of the ground based GW detectors and probably the hardest low frequency noise to be tackled. In AdV is expected to limit the sensitivity below $20-30$ Hz. Underground detectors can reduce the impact of this noise source, as e.g. KAGRA, and future third generation GW detectors.

Quantum noise

This noise source arises from the quantum nature of light. It is composed by the photon counting noise (phase noise or shot noise) at the photodetector and by the radiation pressure noise (that is the photon momentum transfer at the test masses). For the AdV case, the shot noise will limit the sensitivity for all the frequency above ≈ 300Hz while the radiation pressure noise will contribute to limit the low frequency sensitivity. This noise cannot be reduced in the whole frequency range by a brute force approach. The most promising approach is to build correlations between the shot noise and the radiation pressure noise in order to reshape the quantum noise. A method to build those correlation is to utilize a signal recycling technique. Another method is to substitute the coherent vacuum flactuation that enters from the dark port of the interferometer with a squeezed vacuum, in order to reduce one of the two quantum noises at the price of enhancing the other one. Since the shot noise and the radiation pressure noise limit the interferometer sensitivity in two different frequency ranges, the optimal solution is to inject a frequency dependent squeezed vacuum state whose ellipse rotates as function of frequency in order to reduce the radiation pressure noise at low frequency and the shot noise at high frequency.

The aim of the project which provides the framework for this thesis is to realize a squeezed vacuum source for AdV.

Other noises

There are a plethora of other noises that contribute to limit the AdV sensitivity to GWs, such as magnetic noise, alignment and control noises, excess gas noise and stray light noise.

1.3 Gravitational wave detection

On 14 September 2015 the first gravitational wave have been directly observed by the two LIGO observatories (LIGO Hanford and LIGO Livingston) [1]. This gravitational wave was originated by a coalescence of two black holes at a luminosity distance of distance of 410^{+160}_{-180} Mpc corresponding to a redshift $z = 0.09^{+0.03}_{-0.04}$. In the source frame, the initial black hole masses are $36^{+5}_{-4}M_{\odot}$ and $29^{+4}_{-4}M_{\odot}$, and the final black hole mass is $62^{+4}_{-4}M_{\odot}$, with the equivalent of $3.0^{+0.5}_{-0.5}M_{\odot}$ energy radiated in gravitational waves. These observations demonstrate the existence of gravitational wave, the existence of stellar-mass black holes with masses higher than $20M_{\odot}$, the existence of binary stellar-mass black hole systems and that those binary systems can coalesce. Fig.1.6 shows the coincident signal GW150914 detected by the two LIGO observatories.

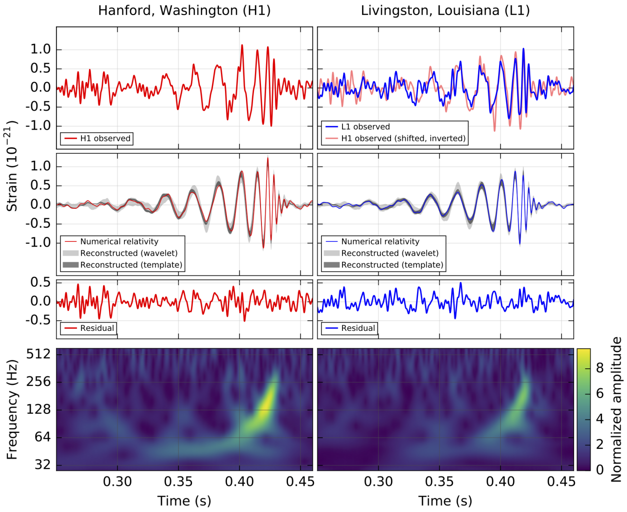

Figure 1.6: From [1]. The gravitational-wave event GW150914 observed by the LIGO Hanford (H1, left column panels) and Livingston (L1, right column panels) detectors. Times are shown relative to September 14, 2015 at 09:50:45 UTC. For visualization, all time series are filtered with a $35 - 350$Hz bandpass filter to suppress large fluctuations outside the detectors' most sensitive frequency band, and band-reject filters to remove the strong instrumental spectral lines. Top row, left: H1 strain. Top row, right: L1 strain. GW150914 arrived first at L1 and $6.9^{+0.5}_{-0.4}$ ms later at H1; for a visual comparison, the H1 data are also shown, shifted in time by this amount and inverted (to account for the detectors' relative orientations). Second row: Gravitational-wave strain projected onto each detector in the $35 - 350$Hz band. Solid lines show a numerical relativity waveform for a system with parameters consistent with those recovered from GW150914 [20] confirmed to 99.9% by an independent calculation based on [21]. Shaded areas show 90% credible regions for two independent waveform reconstructions. One (dark gray) models the signal using binary black hole template waveforms [22]. The other (light gray) does not use an astrophysical model, but instead calculates the strain signal as a linear combination of sine-Gaussian wavelets [23, 24]. These reconstructions have a 94% overlap, as shown in [22]. Third row: Residuals after subtracting the filtered numerical relativity waveform from the filtered detector time series. Bottom row: A time-frequency representation [25] of the strain data, showing the signal frequency increasing over time.

On December 26, 2015 at 03:38:53 UTC a second gravitational wave has been directly observed by the GW detectors network [2]. The signal, GW151226, persisted in the LIGO frequency band for approximately 1 s, increasing in frequency and amplitude over about 55 cycles from 35 to 450 Hz, and reached a peak gravitational strain of $3.4^{+0.7}_{-0.9} \times 10^{-22}$. The inferred source-frame initial black hole masses are $14.2^{+8.3}_{-3.7} M_\odot$ and $7.5^{+2.3}_{-2.3} M_\odot$, and the final black hole mass is $20.8^{+6.1}_{-1.7} M_\odot$. At least one of the component black holes has spin greater than 0.2. This source is located at a luminosity distance of 440^{+180}_{-190} Mpc corresponding to a redshift of $0.09^{+0.03}_{-0.04}$.

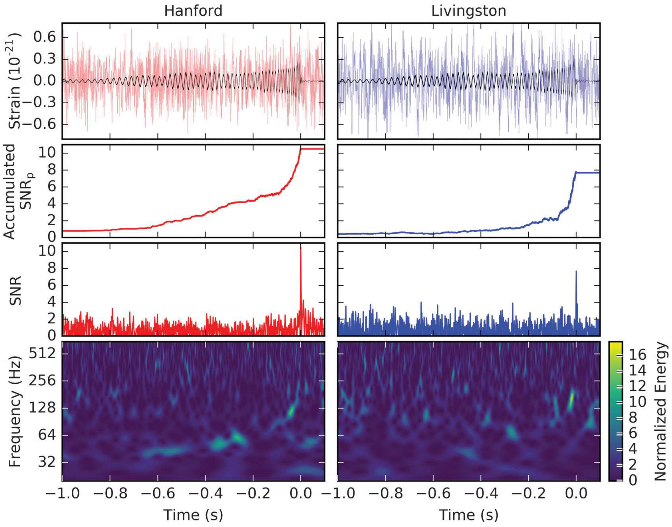

Figure 1.7: From [2]. GW151226 observed by the LIGO Hanford (left column) and Livingston (right column) detectors, where times are relative to December 26, 2015 at 03:38:53.648 UTC. First row: Strain data from the two detectors, where the data are filtered with a 30 − 600 Hz bandpass filter to suppress large fluctuations outside this range and band-reject filters to remove strong instrumental spectral lines [26]. Also shown (black) is the best-match template from a nonprecessing spin waveform model reconstructed using a Bayesian analysis [27] with the same filtering applied. As a result, modulations in the waveform are present due to this conditioning and not due to precession effects. The thickness of the line indicates the 90% credible region. Second row: The accumulated peak signal-to-noise ratio ($\mathrm{SNR_p}$) as a function of time when integrating from the start of the best-match template, corresponding to a gravitational-wave frequency of 30 Hz, up to its merger time. The total accumulated $\mathrm{SNR_p}$ corresponds to the peak in the next row. Third row: Signal-to-noise ratio (SNR) time series produced by time shifting the best-match template waveform and computing the integrated SNR at each point in time. The peak of the SNR time series gives the merger time of the best-match template for which the highest overlap with the data is achieved. The single-detector SNRs in LIGO Hanford and Livingston are 10.5 and 7.9, respectively, primarily because of the detectors' differing sensitivities. Fourth row: Time-frequency representation [25] of the strain data around the time of GW151226. In contrast to GW150914 [1], the signal is not easily visible.

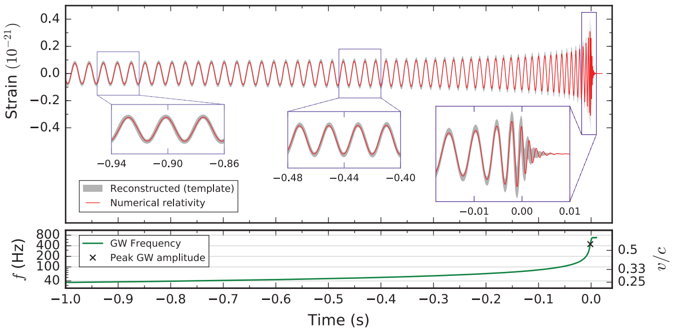

Figure 1.8: From [2]. Estimated gravitational-wave strain from GW151226 projected onto the LIGO Livingston detector with times relative to December 26, 2015 at 03:38:53.648 UTC. This shows the full bandwidth, without the filtering used for Fig.1.7. Top: The 90% credible region (as in [22]) for a nonprecessing spin waveform-model reconstruction (gray) and a direct, nonprecessing numerical solution of Einstein's equations (red) with parameters consistent with the 90% credible region. Bottom: The gravitational-wave frequency f (left axis) computed from the numerical-relativity waveform. The cross denotes the location of the maximum of the waveform amplitude, approximately coincident with the merger of the two black holes. During the inspiral, f can be related to an effective relative velocity (right axis) given by the post-Newtonian parameter $v/c = (GM\pi f/c^3)^{1/3}$, where M is the total mass.

Chapter 2

Classical and quantum optics

In this chapter I briefly overview the basics of non linear optics and quantum optics which are prerequisites for the thesis work. The electromagnetic field quantization and Heisenberg Uncertainty are used to introduce properties of coherent squeezed states and to the homodyne detection method to characterize them. Non linear media are discussed in the context of second harmonic generation and squeezed light generation.

2.1 Quantization of the electromagnetic field

The quantization of the electromagnetic field usually starts from the classical Hamiltonian of the field, that is:

$$\mathcal{H} = \frac{1}{2}\int_V \mathrm{d}\tau \left(\epsilon_0 E^2 + \frac{B^2}{\mu_0}\right) \tag{2.1.1}$$

where the integration is performed over the volume of the electromagnetic field and E is the electric field, ϵ_0 is the vacuum dielectric constant and B is the magnetic field and μ_0 is the vacuum magnetic permeability. Following [28], this Hamiltonian can be rewritten as

$$\mathcal{H} = \frac{1}{2}\sum_j \left(m_j \omega_j^2 q_j^2 + \frac{p_j^2}{m_j}\right) \tag{2.1.2}$$

where m_j is a constant with the dimension of mass, ω_j is the electromagnetic field angular frequency, q_j is the normal amplitude with the dimension of a length and $p_j = m_j \dot{q}_j$ is the canonical momentum of q_j.

The quantization of this Hamiltonian can be realized identifying q_j and p_j as operators which obey the commutation relations:

$$[q_j, p_{j'}] = \imath\hbar\delta(j - j') \qquad \text{and} \qquad [q_j, q_{j'}] = [p_j, p_{j'}] = 0 \tag{2.1.3}$$

Making the canonical transformation to operators a_j and $a_j^\dagger$ defined as follows

$$a_j = \frac{\mathrm{e}^{\imath\omega_j t}}{\sqrt{2m_j\hbar\omega_j}}\left(m_j\omega_j q_j + \imath p_j\right) \tag{2.1.4a}$$

$$a_j^\dagger = \frac{\mathrm{e}^{-\imath\omega_j t}}{\sqrt{2m_j\hbar\omega_j}}\left(m_j\omega_j q_j - \imath p_j\right) \tag{2.1.4b}$$

the Hamiltonian (2.1.2) becomes

$$\mathcal{H} = \hbar \sum_j \omega_j \left(a_j^\dagger a_j + \frac{1}{2} \right) \tag{2.1.5}$$

Using (2.1.3) the commutation relations between a_j and $a_j^\dagger$ are

$$[a_j, a_{j'}^\dagger] = \delta(j - j') \qquad \text{and} \qquad [a_j, a_{j'}] = [a_j^\dagger, a_{j'}^\dagger] = 0 \tag{2.1.6}$$

The operators a_j and $a_j^\dagger$ are usually addressed as the annihilation and the creation operators, respectively.

Starting from the annihilation and the creation operators of a single mode field, we define the quadrature operators X_+ and X_-:

$$X_+ = \left(a + a^\dagger\right) \qquad \text{and} \qquad X_- = -\imath \left(a - a^\dagger\right) \tag{2.1.7}$$

These two quadrature operator are usually called amplitude quadrature and phase quadrature [29]. A generic quadrature operator X_θ can be described using a linear combination of X_+ and X_-:

$$\begin{aligned} X_\theta &= a\mathrm{e}^{-\imath\theta} + a^\dagger \mathrm{e}^{\imath\theta} \\ &= X_+ \cos\theta + X_- \sin\theta \end{aligned} \tag{2.1.8}$$

where θ is the quadrature angle. Starting from (2.1.6) it is straightforward to demonstrate that

$$[X_+, X_-] = 2\imath \tag{2.1.9}$$

Another useful operator is the number operator defined as

$$N = a^\dagger a \tag{2.1.10}$$

Taking the mean number of photon of a state $\langle N \rangle$ and multiplying by the photon energy $\hbar\omega$ we have the optical power of the state

$$P_{opt} = \langle N \rangle \hbar\omega \tag{2.1.11}$$

2.1.1 Fock states

Fock or number states are eigenstates of the number operator:

$$N \left| n \right\rangle = n \left| n \right\rangle \tag{2.1.12}$$

The ground state or vacuum state is defined as

$$N \left| 0 \right\rangle = 0 \tag{2.1.13}$$

Combining eq.(2.1.5) and (2.1.13) we can calculate the energy of the vacuum state. We take the case of a single mode field.

$$\left\langle 0 \right| \mathcal{H} \left| 0 \right\rangle = \frac{1}{2}\hbar\omega \tag{2.1.14}$$

chosen $\langle 0|0 \rangle = 1$.

Starting from the vacuum state all the Fock state can be defined applying the creation operator. In general we have

$$|n\rangle = \frac{\left(a^\dagger\right)^n}{\sqrt{n!}} |0\rangle \tag{2.1.15}$$

The Fock states are orthogonal and complete:

$$\langle n|m\rangle = \delta_{nm} \qquad \text{and} \qquad \sum_{n=0}^{\infty} |n\rangle \langle n| = 1 \tag{2.1.16}$$

The variances of the quadrature operators on a Fock state are:

$$\begin{aligned} V(X_+) = (\Delta X_+)^2 &= \langle n| (X_+)^2 |n\rangle - (\langle n| X_+ |n\rangle)^2 \\ &= 1 + 2n \end{aligned} \tag{2.1.17}$$

and

$$\begin{aligned} V(X_-) = (\Delta X_-)^2 &= \langle n| (X_-)^2 |n\rangle - (\langle n| X_- |n\rangle)^2 \\ &= 1 + 2n \end{aligned} \tag{2.1.18}$$

In the case of the vacuum state $\Delta X_+ = \Delta X_- = \pm 1$.

2.1.2 Coherent states

An example of a coherent state is the light emitted by a stabilized and monochromatic laser.

A coherent state $|\alpha\rangle$ is a left eigenstate of the annihilation operator:

$$a |\alpha\rangle = \alpha |\alpha\rangle \tag{2.1.19}$$

where α is a complex number. The mean photon number of a coherent state is therefore

$$\langle\alpha| N |\alpha\rangle = |\alpha|^2 \tag{2.1.20}$$

and $\Delta N = |\alpha|$. This is characteristic of a Poissonian distribution.

Starting from the vacuum state, a coherent state can be defined using a displacement operator $D(\alpha)$:

$$|\alpha\rangle = D(\alpha) |0\rangle \qquad \text{with} \qquad D(\alpha) = \exp\left(\alpha a^\dagger + \alpha^* a\right) \tag{2.1.21}$$

The variances of the quadrature operators on a coherent state are $V(X_+) = V(X_-) = 1$ and therefore $\Delta X_+ = \Delta X_- = \pm 1$.

2.1.3 The Heisenberg uncertainty principle

The Heisenberg uncertainty principle [30] states that for two noncommuting Hermitian operators q and p one cannot simultaneously measure their physical quantities with arbitrary precision:

$$\Delta q \Delta p \geq \frac{1}{2} |\langle [q,p] \rangle| \tag{2.1.22}$$

Heisenberg uncertainty principle applied to the quadrature operators (eq.(2.1.9)) translates into

$$\Delta X_+ \Delta X_- \geq 1 \tag{2.1.23}$$

From the previous two paragraph we see that all coherent states and vacuum state fulfill the special case of the Heisenberg uncertainty principle

$$\Delta X_+ \Delta X_- = 1 \tag{2.1.24}$$

All states satisfying this equation are known as minimum uncertainty states.

2.1.4 Squeezed states

The Heisenberg uncertainty principle states that the product of the variances of two noncommuting operators has a minimum. However, it does not put any constrain on the individual component variances, thus if

$$(\Delta q)^2 < \frac{1}{2}\left|\langle[q,p]\rangle\right| \qquad \text{or} \qquad (\Delta p)^2 < \frac{1}{2}\left|\langle[q,p]\rangle\right| \tag{2.1.25}$$

but not simultaneously, the state is said to be squeezed.

In analogy to the coherent state, a squeezed state can be described applying a squeezing operator to a vacuum state. The squeezing operator $S(r,\theta)$ is defined as

$$S(r,\theta) = \exp\left(\frac{1}{2} r \mathrm{e}^{-2\imath\theta}(a)^2 - \frac{1}{2} r \mathrm{e}^{2\imath\theta}(a^\dagger)^2\right) \tag{2.1.26}$$

where r is the the squeezing factor and θ is the quadrature angle of the squeezing: $\theta = 0$ corresponds to amplitude squeezing and $\theta = \pi/2$ to phase squeezing.

The squeezed vacuum is thus obtained applying the squeezing operator to the vacuum state

$$|0,r,\theta\rangle = S(r,\theta)\,|0\rangle \tag{2.1.27}$$

while a bright squeezed state is defined as

$$|\alpha,r,\theta\rangle = D(\alpha)S(r,\theta)\,|0\rangle \tag{2.1.28}$$

For an amplitude squeezed state ($\theta = 0$), application of the number operator will yield

$$\langle\alpha,r,0|\,N\,|\alpha,r,0\rangle = |\alpha|^2 + \sinh^2(r) \tag{2.1.29}$$

On the same state, the variance of the quadrature operators X_+ and X_- are

$$(\Delta X_+)^2 = \mathrm{e}^{-2r} \qquad \text{and} \qquad (\Delta X_-)^2 = \mathrm{e}^{2r} \tag{2.1.30}$$

On the other hand, for a phase squeezed state ($\theta = \pi/2$) the variance of the quadrature operators X_+ and X_- are

$$(\Delta X_+)^2 = \mathrm{e}^{2r} \qquad \text{and} \qquad (\Delta X_-)^2 = \mathrm{e}^{-2r} \tag{2.1.31}$$

The squeezed state described previously are minimum uncertainty states. Imperfect processes, such as loss, will result in a state that is not a minimum uncertainty state. We therefore can define the squeezing purity P as

$$(\Delta X_+)^2(\Delta X_-)^2 = P \tag{2.1.32}$$

A pure state will have a purity of $P = 1$, as does the vacuum. A pure state is a minimum uncertainty state.

2.2 Linearized quantum theory

Let's consider the single mode annihilation operator a and let's break into two different contributions:

$$a = \alpha + \delta a(t) \tag{2.2.1}$$

where α is a complex number representing the single frequency part of the mode and $\delta a(t)$ are the fluctuations and modulations (therefore representing the continuum of modes surrounding the single frequency carrier.

The number operator becomes

$$\begin{aligned} N = a^\dagger a &= (\alpha^* + \delta a^\dagger(t))(\alpha + \delta a(t)) \\ &\approx \alpha^2 + \alpha(\delta a^\dagger(t) + \delta a(t)) \\ &\approx \alpha^2 + \alpha \delta X_+(t) \end{aligned} \tag{2.2.2}$$

where we have taken the arbitrary phase of α real and linearized by assuming the fluctuation are small and hence neglecting higher than first order terms in the fluctuations. We see that we are effectively measuring the quadrature operator $\delta X_+(t) = \delta a^\dagger(t) + \delta a(t)$. For this reason δX_+ is referred to as the amplitude quadrature operator.

2.2.1 Photodetection

Combining eq.(2.2.2) with eq.(2.1.11) we have that the optical power of a beam can be written as

$$P_{opt} \approx \hbar\omega(\alpha^2 + \alpha \delta X_+(t)) \tag{2.2.3}$$

A common measurement of the optical power of a beam involves a photodiode. As a consequence of the Photoelectric Effect, incident photons hitting a photosensitive medium are a source of freely moving electrons. The produced photocurrent i, is given by

$$i = \rho P_{opt} = \frac{e\eta_{pd}}{\hbar\omega} P_{opt} \tag{2.2.4}$$

where ρ is the responsivity of the photodetector (in units of A/W), η_{pd} is the quantum detection efficiency of the detection medium, $\hbar\omega$ the energy per photon, and e is the modulus of the electron charge. Using eq.(2.2.3) in eq.(2.2.4) in the case of an ideal photodiode ($\eta_{pd} = 1$) we have

$$i \approx e(\alpha^2 + \alpha \delta X_+(t)) \tag{2.2.5}$$

The first term of eq.(2.2.5) is a non-fluctuating term that is directly proportional to the optical intensity of the incident light, while the second term is a fluctuating term proportional to the amplitude quadrature times the coherent amplitude.

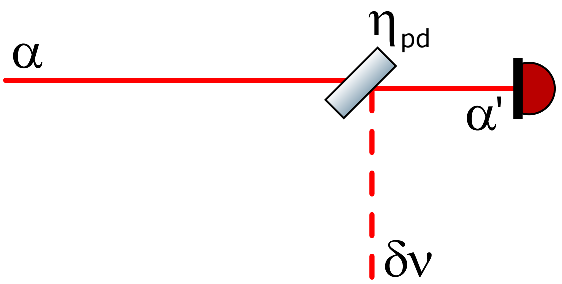

Figure 2.1: Model of a real photodiode with quantum efficiency η_{pd}. One of the two input power of the beam splitter is occupied by the input beam, while the other is occupied by the vacuum state. The light that reaches the ideal photodiode is a linear combination of the two input of the beam splitter.

The case of $\eta_{pd} < 1$ can be modeled considering a beam that go through a beam splitter with reflectivity η_{pd} before being detected by an ideal photodiode (see Fig.2.1). The beam that is detected by the ideal photodiode is the linear combination of the two beam splitter input beams, that are the beam that we want to measure and the vacuum. In this case, the photocurrent generated by the photodiode is

$$i \approx e\eta_{pd}\alpha^2 + e\alpha\left(\eta_{pd}\delta X_+^\alpha(t) + \sqrt{\eta_{pd}(1-\eta_{pd})}\delta X_+^v(t)\right) \tag{2.2.6}$$

The photocurrent in this case differs by eq.(2.2.5) in both the fluctuating and the non-fluctuating term: the non-fluctuating term is scaled by the quantum efficiency of the photodiode and the fluctuating term is a linear combination between the amplitude quadrature fluctuation of the input beam ($\delta X_+^\alpha(t)$) and the amplitude quadrature fluctuation of the vacuum state ($\delta X_+^v(t)$).

2.2.2 Balanced homodyne detection

As seen in the previous paragraph, non perfect quantum efficiency is a limitation to the measurement of quantum noises of light. Measuring the quantum noise requires that all classical noise terms, such as laser intensity noise and electronic noise, are reduced to a level well below the noise level of interest. To perform these measurements, a commonly used method is the balanced homodyne detection (see Fig.2.2).

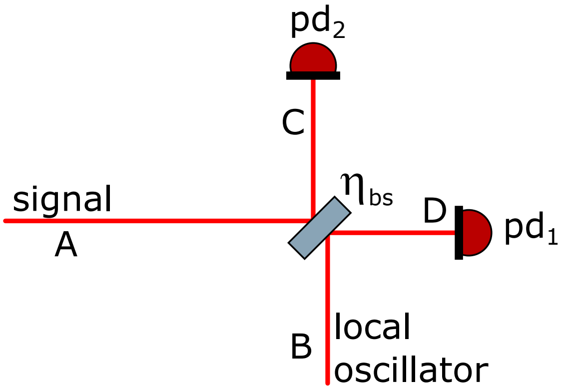

Figure 2.2: Scheme of an ideal balanced homodyne detector. The local oscillator (LO) and the signal beams are mixed on the beam splitter. The two resulting beams are detected by two ideal photodiodes pd$_1$ and pd$_2$.

The two inputs of the homodyne detector are the signal beam $A = \alpha + \delta a$ and the local oscillator (LO) beam $B = \beta + \delta b$. The quantum properties of the signal beam are measured by recording the difference of the two photodiodes' photocurrents.

The two output beams of the beam splitter (C and D) are

$$C = \sqrt{1-\eta_{bs}}A + \sqrt{\eta_{bs}}B\mathrm{e}^{\imath\theta} \tag{2.2.7a}$$

$$C = \sqrt{\eta_{bs}}A - \sqrt{1-\eta_{bs}}B\mathrm{e}^{\imath\theta} \tag{2.2.7b}$$

where η_{bs} is the splitting ratio of the beam splitter and θ is the relative phase of the two input beams and it has been chosen to ensure that the coherent amplitude terms of the fields are real. Assuming ideal photodiodes, the two photocurrents are

$$i_1/e = (1-\eta_{bs})A^\dagger A + \eta_{bs}B^\dagger B + \sqrt{\eta_{bs}(1-\eta_{bs})}\left(A^\dagger B\mathrm{e}^{\imath\theta} + B^\dagger A\mathrm{e}^{-\imath\theta}\right) \tag{2.2.8a}$$

$$i_2/e = \eta_{bs}A^\dagger A + (1-\eta_{bs})B^\dagger B - \sqrt{\eta_{bs}(1-\eta_{bs})}\left(A^\dagger B\mathrm{e}^{\imath\theta} + B^\dagger A\mathrm{e}^{-\imath\theta}\right) \tag{2.2.8b}$$

and the difference of the two photocurrent is

$$(i_1 - i_2)/e = (1 - 2\eta_{bs})A^\dagger A + (2\eta_{bs} - 1)B^\dagger B + 2\sqrt{\eta_{bs}(1 - \eta_{bs})}\left(A^\dagger B e^{\imath\theta} + B^\dagger A e^{-\imath\theta}\right) \tag{2.2.9}$$

Using eq.(2.2.2) we can approximate $A^\dagger A \approx \alpha^2 + \alpha\delta X_+^A$ and $B^\dagger B \approx \beta^2 + \beta\delta X_+^B$ where $\delta X_+^A = \delta a + \delta a^\dagger$ and $\delta X_+^B = \delta b + \delta b^\dagger$ are the amplitude quadrature of the signal and the LO beam respectively. Therefore, eq.(2.2.9) can be approximate as follow:

$$\begin{aligned}(i_1 - i_2)/e \approx &(1 - 2\eta_{bs})(\alpha^2 + \alpha\delta X_+^A) + (2\eta_{bs} - 1)(\beta^2 + \beta\delta X_+^B) + 2\sqrt{\eta_{bs}(1 - \eta_{bs})}\times \\ &\left[2\alpha\beta\cos\theta + \alpha(\delta X_+^B\cos\theta - \delta X_-^B\sin\theta) + \beta(\delta X_+^A\cos\theta + \delta X_-^A\sin\theta)\right]\end{aligned} \tag{2.2.10}$$

In most of the cases of interest, the LO is much brighter than the signal field ($\beta \gg \alpha$). This condition is particularly true when the signal beam is a vacuum state. In those cases, all the terms of eq.(2.2.10) where β is not present can be neglected. Therefore we have that

$$\begin{aligned}(i_1 - i_2)/e \approx &(2\eta_{bs} - 1)(\beta^2 + \beta\delta X_+^B) + \\ &2\sqrt{\eta_{bs}(1 - \eta_{bs})}\left[2\alpha\beta\cos\theta + \beta(\delta X_+^A\cos\theta + \delta X_-^A\sin\theta)\right]\end{aligned} \tag{2.2.11}$$

Supposing an ideal splitting ratio of 50% we finally have

$$(i_1 - i_2)/e \approx 2\alpha\beta\cos\theta + \beta(\delta X_+^A\cos\theta + \delta X_-^A\sin\theta) \tag{2.2.12}$$

The first term of eq.(2.2.12) is a DC term that describes the interference between the two fields as the phase between the signal and the local oscillator is varied. The second term contains the quantum properties of the signal beam that are amplified by the coherent amplitude of the LO beam. By choosing the phase between the signal and the LO to be $\theta = 0$, the output of the homodyne detector is proportional to the signal amplitude quadrature, while choosing $\theta = \pi/2$ the output is proportional to the signal phase quadrature.

2.3 Squeezed state and losses

In section 2.2.1 we shown how in the non ideal case of a photodiode, the quantum properties of a state are mixed with the quantum properties of the vacuum state. In general, any losses (such as transmission losses, absorption, non ideal quantum efficiency, mode mismatching, etc) can be modeled with the introduction of a partially reflective beam splitter which couples the vacuum state noises into the beam quantum properties. After the virtual beam splitter we will have

$$a' = \sqrt{\eta}a + \sqrt{1 - \eta}\delta v \tag{2.3.1}$$

where $1 - \eta$ are the generic “losses” and hence η is the transmittivity of the virtual beam splitter. Therefore we also have

$$a'^\dagger a' = \eta(\alpha^2 + \alpha\delta X_+^a) + \sqrt{\eta(1 - \eta)}\alpha\delta X_+^v \tag{2.3.2}$$

where δX_+^v is the vacuum amplitude quadrature fluctuation and the input beam is linearized as did in the previous sections. The variance of the photon number $V_{a'}$ can be calculated as

$$V_{a'} = \eta V_a + (1 - \eta)V_v \tag{2.3.3}$$

being V_a the photon number variance of the state before the beam splitter and V_v the photon number variance of the vacuum state. Since $V_v = 1$ and $\eta \in [0, 1]$, the higher are the losses, the closer is $V_{a'}$ to V_v.

For a squeezed state the variance of the two quadrature X_+ and X_- are given respectively by (2.1.30) for an amplitude squeezed state and by (2.1.31) for a phase squeezed state. Fig.2.3 shows the effect of losses on a pure squeezed state. The resulting state is a minimum uncertainty state just for $\eta = 0$ and $\eta = 1$.

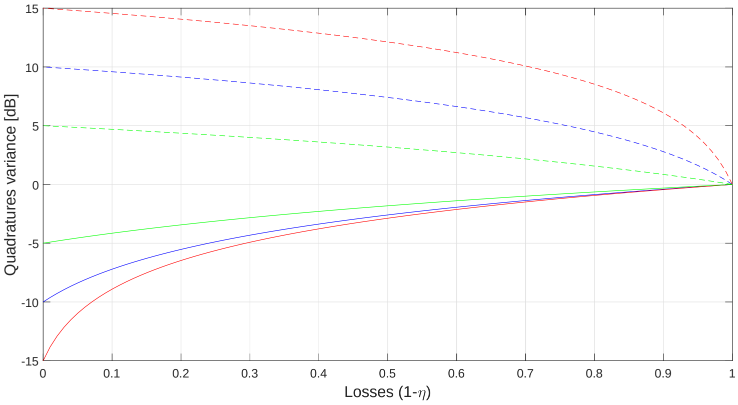

Figure 2.3: Effect of losses on a pure amplitude/phase squeezed state. For an amplitude squeezed state the continue lines represent the variance of X_+ and the dashed lines are the variance of X_-; for a phase squeezed state the variances are just switched. The X_+ and X_- quadrature variances are plotted as a function of the losses in three different situations: red curves refer to a state with 15 dB of amplitude/phase noise suppression and 15 dB of phase/amplitude noise enhancement in the loss-less case; blue (green) curves show the same information for a state with 10 dB (5 dB) squeezing in the loss-less case.

2.3.1 Squeezing ellipse phase fluctuations

Another effect that decreases the noise enhancement/suppression of a squeezed state is the coupling of the X_+ and X_- quadrature variances due to the squeezing ellipse phase fluctuations. As function of the rms phase fluctuations $\bar{\theta}$, the measured variances are

$$V(X'_{+,-}) = V(X_{+,-})\cos^2\bar{\theta} + V(X_{-,+})\sin^2\bar{\theta} \tag{2.3.4}$$

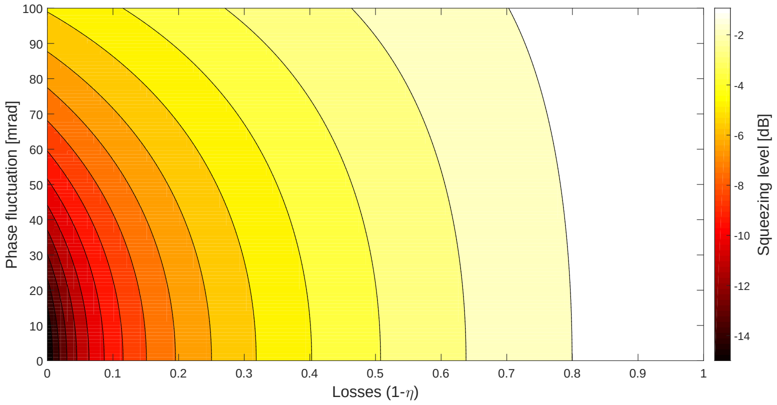

Figure 2.4: Degradation of the squeezing level of a pure 15 dB squeezed state due to the combined effect of losses and squeezing ellipse phase fluctuations.

The combined effect of losses and phase fluctuations is shown in Fig.2.4. This figure shows the degradation of the squeezing level starting from a pure 15 dB squeezed state.

2.4 Non linear optics

The beginning of the field of non linear optics is often taken to be the discovery of second-harmonic generation by Franken et al.(1961) [31], shortly after the demonstration of the first working laser by Maiman in 1960.

For most of the materials the induced polarization $P(t)$ depends linearly on the strength $E(t)$ of an applied optical field:

$$P(t) = \epsilon_0 \chi^{(1)} E(t) \tag{2.4.1}$$

where $\chi^{(1)}$ is the linear susceptibility and ϵ_0 is the permittivity of free space. In general, this approximation does not hold true. In fact, for intense electric field, eq(2.4.1) is generalized by expressing the polarization $P(t)$ as a power series in the field strength $E(t)$:

$$\begin{aligned} P(t) &= \epsilon_0 \left[\chi^{(1)} E(t) + \chi^{(2)} E^2(t) + \chi^{(3)} E^3(t) + \dots\right] \\ &\equiv P^{(1)}(t) + P^{(2)}(t) + P^{(3)}(t) + \dots \end{aligned} \tag{2.4.2}$$

The quantities $\chi^{(2)}$ and $\chi^{(3)}$ are known as the second- and third-order nonlinear optical susceptibilities, respectively. In my work only second-order processes are present.

Let's take the case where the electric field can be written as $E(t) = E_0 \mathrm{e}^{-\imath\omega t} + \mathrm{c.c.}$ In this case, the second-order polarization of eq.(2.4.2) is

$$P^{(2)}(t) = \epsilon_0 \chi^{(2)} \left[E_0^2 \mathrm{e}^{-2\imath\omega t} + \mathrm{c.c.}\right] + \epsilon_0 \chi^{(2)} \left[2 E_0 E_0^*\right] \tag{2.4.3}$$

This equation lead to the production of two different field, one at twice the frequency of the input electric field and one at zero frequency. The two processes involved in this situation are known as second harmonic generation (SHG) and optical rectification (OR) respectively. If the input electric field is composed by two or more frequency components, the second-order nonlinear optical susceptibility leads also to sum and difference frequency generation (SFG and DFG respectively).

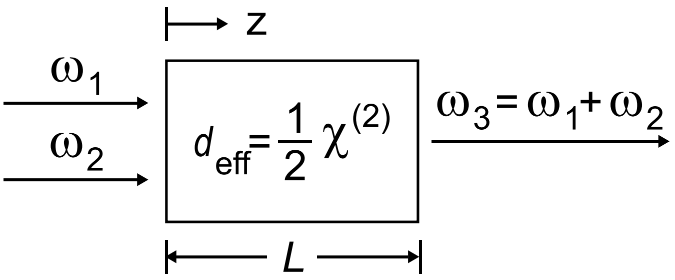

Figure 2.5: Sum-frequency generation.

Let's take the case of SFG. Fig.2.5 shows the scheme of the process. The generic wave equation for nonlinear optical media can be written as in [32]:

$$\nabla^2 \mathbf{E}_n - \frac{\epsilon^{(1)}(\omega_n)}{c^2} \frac{\partial^2 \mathbf{E}_n}{\partial t^2} = \frac{1}{\epsilon_0 c^2} \frac{\partial^2 \mathbf{P}_n^{NL}}{\partial t^2} \tag{2.4.4}$$

where $\mathbf{E}_n$ is the electric field of the n-th mode, ω_n is the angular frequency of the mode, $\mathbf{P}_n^{NL}$ in the nonlinear part of the polarization and $\epsilon^{(1)}(\omega_n)$ is the linear part of the relative permittivity, which is different for each material. This equation holds true for the case of an isotropic, dissipationless material.

For simplicity, let's take the case of plane wave propagating in the $+z$ direction. In this case, the inputs and the output beams of Fig.2.5 can be written as:

$$E_i(z,t) = E_i \mathrm{e}^{\imath\omega_i t} + \text{c.c.} \qquad \text{where} \quad E_i = A_i \mathrm{e}^{\imath k_i z} \tag{2.4.5}$$

with $i = 1, 2, 3$. We also write the nonlinear source term appearin in eq(2.4.4) as

$$P_3(z,t) = P_3 \mathrm{e}^{\imath\omega_3 t} + \text{c.c.} \qquad \text{where} \quad P_3 = 4\epsilon_0 d_{eff} E_1 E_2 \tag{2.4.6}$$

having $d_{eff} = \chi^{(2)}/2$.

Without going into details, combining eqs(2.4.4), (2.4.6) and (2.4.5) in the slowly varying amplitude approximation, we end up with three coupled differential equations that describes the spatial dependences of A_i:

$$\frac{\mathrm{d}A_1}{\mathrm{d}z} = \frac{2\imath d_{eff}\omega_1^2}{k_1 c^2} A_3 A_2^* \mathrm{e}^{-\imath\Delta k z} \tag{2.4.7a}$$

$$\frac{\mathrm{d}A_2}{\mathrm{d}z} = \frac{2\imath d_{eff}\omega_2^2}{k_2 c^2} A_3 A_1^* \mathrm{e}^{-\imath\Delta k z} \tag{2.4.7b}$$

$$\frac{\mathrm{d}A_3}{\mathrm{d}z} = \frac{2\imath d_{eff}\omega_3^2}{k_3 c^2} A_1 A_2 \mathrm{e}^{\imath\Delta k z} \tag{2.4.7c}$$

where $\Delta k = k_1 + k_2 - k_3$ which is called the wavevector mismatch. Eqs(2.4.7) can be solved in the simplified case of no-pump depletion, that means that A_1 and A_2 can be taken as constants. In this situation, for $\Delta k = 0$, the amplitude A_3 increases linearly with z, and consequently its intensity increases quadratically with z. When the $\Delta k = 0$ condition is not fulfilled, eq(2.4.7a) can be solved by direct integration (between $z = 0$ and $z = L$):

$$A_3(L) = \frac{2\imath d_{eff}\omega_3^2 A_1 A_2}{k_3 c^2} \int_0^L \mathrm{e}^{\imath\Delta k z}\,\mathrm{d}z = \frac{2\imath d_{eff}\omega_3^2 A_1 A_2}{k_3 c^2} \left(\frac{\mathrm{e}^{\imath\Delta k L} - 1}{\imath\Delta k} \right) \tag{2.4.8}$$

The intensity of the generated wave is given by the magnitude of the time-averaged Poynting vector, which is given by

$$I_i = 2 n_i \epsilon_0 c |A_i|^2 \qquad i = 1, 2, 3 \tag{2.4.9}$$

We thus obtain

$$I_3 = \frac{8 n_3 \epsilon_0 d_{eff}^2 \omega_3^4 |A_1|^2 |A_2|^2}{k_3^2 c^3} \left| \frac{\mathrm{e}^{\imath\Delta k L} - 1}{\Delta k} \right|^2 \tag{2.4.10}$$

Note that the effect of wavevector mismatch is entirely included in the squared modulus term. This term can be rewritten as

$$\left| \frac{\mathrm{e}^{\imath\Delta k L} - 1}{\Delta k} \right|^2 = L^2 \operatorname{sinc}^2(\Delta k L/2) \tag{2.4.11}$$

Fig.2.6 shows the effect of wavevector mismatch on the sum frequency generation efficiency. The wavevector mismatch is usually called phase matching.

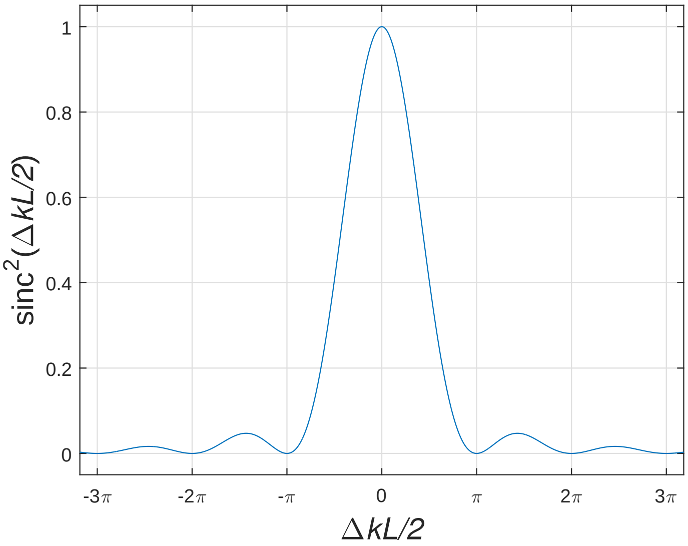

Figure 2.6: Effect of wavevector mismatch on the sum frequency generation efficiency.

2.4.1 Phase matching

The phase matching condition is a general condition that does exist not only for SFG (and therefore for SHG) but also for DFG. This condition is usually not easy to achieve. That's because, commonly, materials shows an effect known as normal dispersion: the refractive index increases as function of frequency. Therefore, the condition for perfect phase matching with collinear beams

$$\frac{n_1\omega_1}{c} + \frac{n_2\omega_2}{c} = \frac{n_3\omega_3}{c} \tag{2.4.12}$$

where $\omega_1 + \omega_2 = \omega_3$ cannot be achieved. The most common procedure for achieving phase matching is to make use of the birefringence displayed by many materials. Birefringence is the dependence of the refractive index on the direction of polarization of the optical radiation.

Three different techniques are commonly used to perform the phase matching. The first two described make use of the birefringence, while the third allows the phase matching condition to be fulfilled even for non birefringent materials:

Type I phase matching: the two input fields (at ω_1 and ω_2) have the same polarization and the produced field is orthogonally polarized. This can be achieved by adjusting the angle of incidence, changing the crystal temperature or both. The phase matching is said to be noncritical if the refractive indices are matched for light fields propagating in the plane which is orientated 90° with respect to the optical axis of the crystal.

Type II phase matching: the two input fields (at ω_1 and ω_2) have orthogonal polarization and the harmonic field has the same polarization as one of the fundamental fields. Again this can be achieved by adjusting the angle of incidence, changing the crystal temperature or both. Independently of the relative values of ω_1 and $\omega 2$, type I phase matching is easier to achieve than type II.

Quasi phase matching: it is done via a periodic manipulation of the accumulated relative optical phase. The crystal's domain is inverted periodically on short length scales resulting in a phase mismatch of

$$\Delta k_{QPM} = k_1 + k_2 - k_3 - \frac{2\pi}{\Lambda} \tag{2.4.13}$$

where Λ is the crystal inversion period. Due to the periodic poling term, there is no requirement of the refractive index being equal for the fundamental and harmonic fields. An advantage of the periodic poled (PP) materials is that phase matching can be achieved at room temperature over a very wide temperature range compared to the other two phase matching methods and the phase matching temperature depends on Λ. Periodically poling allows to exploit additional terms of the nonlinear susceptibility matrix which are larger than those used in type I and type II phase matching. Using quasi-phase matching, the constant d_{eff} of eqs(2.4.7) must be substituted with $d_{QPM} = (2/\pi)d_{eff}$.

2.5 Squeezed state generation

The very first generation of a squeezed state was realized in 1985 by Slusher et al. [33] using nondegenerate four-wave mixing. The actual most commonly used process to generate a squeezed state is the degenerate parametric down conversion in an optical cavity, as used firstly by Wu et al. in 1986 [34]. The degenerate parametric down conversion is a particular case of DFG where the pump field at $\omega_3 = \omega_p$ create via nonlinear interaction a signal field at $\omega_1 = \omega_2 = \omega_s = \omega_3/2$ (see [32]).

In the rotating wave approximation, the Hamiltonian of a degenerate parametric down conversion process can be written as in [28]:

$$\mathcal{H} = \hbar\kappa(a^\dagger a^\dagger b + aab^d agger) \tag{2.5.1}$$

where $a, a^\dagger$ and $b, b^\dagger$ are the annihilation/creation operators for the signal field and the pump field respectively and κ is a constant which depends upon the second-order susceptibility tensor that mediates the interaction. Let's assume the pump field is a coherent state and let's approximate b as $\beta \exp(-\imath\phi)$ where β is the real amplitude of the pump field and ϕ is the relative phase between the pump and the signal beams. In this case, eq(2.5.1) can be rewritten as

$$\mathcal{H} = \hbar\kappa\beta(a^\dagger a^\dagger \mathrm{e}^{-\imath\phi} + aa\mathrm{e}^{\imath\phi}) \tag{2.5.2}$$

The evolution operator associated to this process is therefore

$$U(t,0) = \exp(-\imath\mathcal{H}t/\hbar) = \exp\left[-\imath\kappa\beta t(a^\dagger a^\dagger \mathrm{e}^{-\imath\phi} + aa\mathrm{e}^{\imath\phi})\right] \tag{2.5.3}$$

This operator looks like exactly as the squeezing operator defined in eq(2.1.26).

Chapter 3

Squeezing applied to GW detectors

In this chapter I describe the advanced Virgo simulated noise budget with the injection of a squeezed vacuum into the dark port of the interferometer.

Injecting a squeezed vacuum state into an interferometer, modifies the quantum noises of the detector with respect to the case where no squeezing is injected. A detailed explanation of the quantum noises of a GW interferometer can be found in [35]. The injection of frequency independent squeezed vacuum into a GW interferometer have already demonstrated to reduce the detector shot noise [4, 5].

3.1 Squeezing applied to AdV

The tool developed by the LIGO-Virgo collaboration to compute the expected noise budget for a GW detector is called GWINC. According to [17], the detector design sensitivity will be achieved following a step by step process. Within this process, three different interferometer configurations are identified:

1. Power recycled interferometer: in this situation the power recycling (PR) mirror is installed while the signal recycling mirror (SR) is not. This is the first step foreseen by the AdV collaboration and will be implemented with an input power of 25 W.
2. Tuned dual recycled interferometer: both the two recycling cavities (PR and SR) are installed in this configuration and the signal recycling cavity is tuned.
3. Detuned dual recycled interferometer: the only difference of this configuration from the one previous is that the signal recycling cavity is detuned. The choice of the detuning angle allows to tailor the spectral sensitivity of the detector.

Since the squeezing injection is expected to impact only on the quantum noises of the interferometer, in the following, all the non quantum noises are considered altogether and shown as one overall contribution.

Within the collaboration, the sensitivity of the detectors is usually expressed in observable ranges for specific GW sources, in units of Mpc. This quantity expresses the expected maximum distance at which an emitted GW can be measured with a SNR≥ 8. The two more common GW signals that are used to compute ranges are the emission from the coalescence of two neutron stars (NS) with mass $M_{NS} = 1.4M_\odot$ and the coalescence of two black holes (BH) with mass $M_{BH} = 30M_\odot$.

The expected NSNS and BHBH ranges for AdV in the various configuration as function of the input power and the signal recycling mirror detuning are shown in the following, using optimization routines that I developed to post-process the results from the GWINC code.

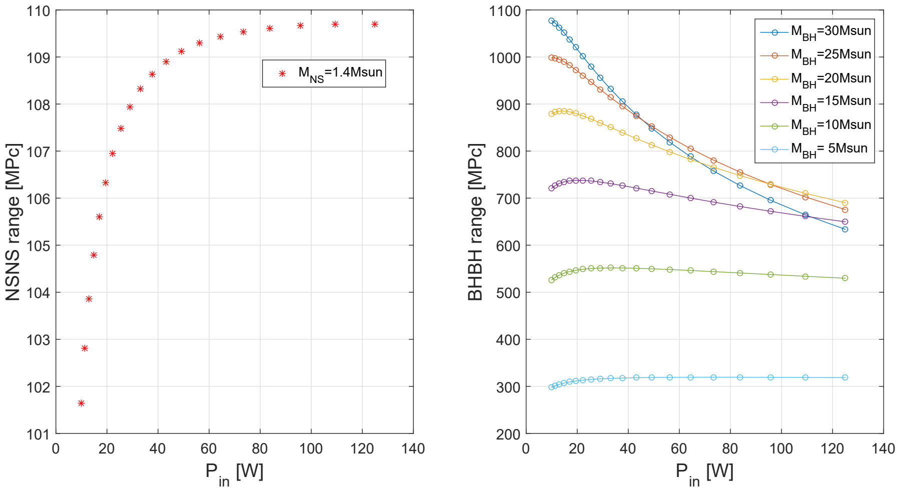

Figure 3.1: Binary coalescences ranges for configuration 1 as function of the input power. The NSNS range increases as function of input power, while, for black holes of mass $M_{BH} = 30M_\odot$ the detection range decrease as the input power increases. For BH with small masses, this behavior changes and for $M_{BH} = 5M_\odot$, the same behavior of the NSNS ranges is obtained.

Fig.3.1 shows the expected ranges for NSNS and BHBH coalescence as function of the injected power ($10 - 125$ W): the NSNS ranges increases as function of the injected power reaching the maximum of 109.7 Mpc with $P_{in} = 125$ W. On the other hand, the BHBH range for $M_{BH} = 30M_\odot$ decreases as the input power increases and the maximum range is 1078 Mpc with $P_{in} = 10$ W. This difference is entirely due to the fact that the radiation pressure noise gets higher as the input power increases and this spoils the detector low frequencies performances. Fig.3.2 shows the AdV sensitivity curves in this two cases.

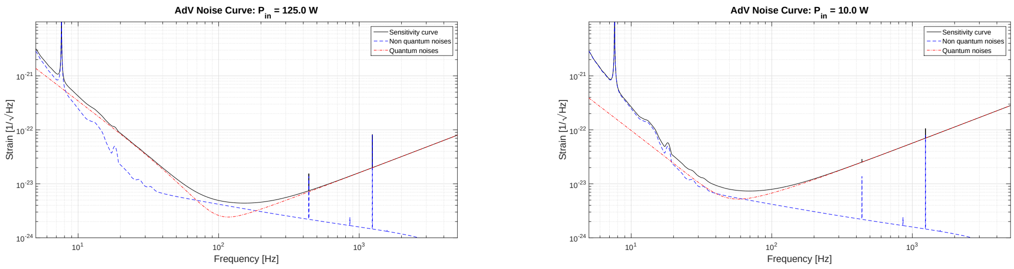

Figure 3.2: The sensitivity curves I computed for configuration 1 in the case of $P_{in} = 125$ W (left) and $P_{in} = 10$ W (right) are shown.

For configuration 2 and 3 I computed the binary system ranges (in this case $M_{BH} = 30M_\odot$) as function of the input power and of the signal recycling cavity detuning. Fig.3.3 shows the ranges of the dual recycled interferometer as function of the input power and the SR detuning. The best NSNS range (145.6 Mpc) is obtained with $P_{in} = 125$ W and a SR detuning of 0.2565 rad, that is 14.69° and the best BHBH range (1381 Mpc) is obtained with $P_{in} = 10$ W and a SR detuning of 1.282 rad, that is 73.47°. As in the configuration 1 case, the difference between this two sets of parameters are the low frequency performances of the interferometer.

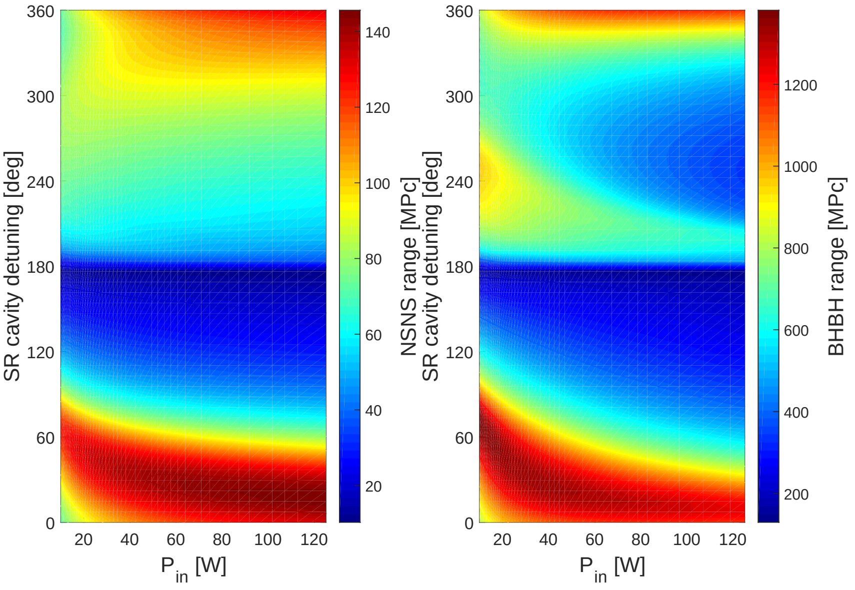

Figure 3.3: Binary coalescences ranges for a dual recycled interferometer as function of the input power and the SR detuning, configurations 2 and 3

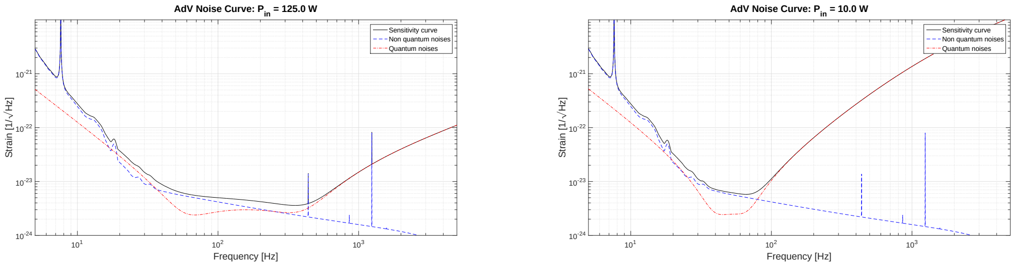

Figure 3.4: The sensitivity curves for configuration 3. (left) input power and SR tuning are optimized to maximize the NSNS range: $P_{in} = 125$ W and SR detuning is 0.2565 rad; (right) input power and SR tuning are optimized to maximize the BHBH range: $P_{in} = 10$ W and SR detuning is 1.282 rad.

Now I consider the effect of injecting frequency independent squeezing into configuration 1. The computation has been performed supposing to start with a pure squeezed state (i.e. phase squeezed state with the squeezing degree equal to the anti-squeezing degree) and then the degradation of the squeezed state due to losses and phase noise are computed. The AdV squeezing working group set a challenging but not optimistic target for the squeezing input losses equal to 20%. Those losses take into account the OPO escape efficiency and absorption, Faraday isolators transmission losses, mode matching between the squeezed vacuum and the interferometer, OMC absorption and mode matching, AdV photodetector non perfect quantum efficiency. For the phase noise a conservative value equal to 30 mrad has been chosen as target.

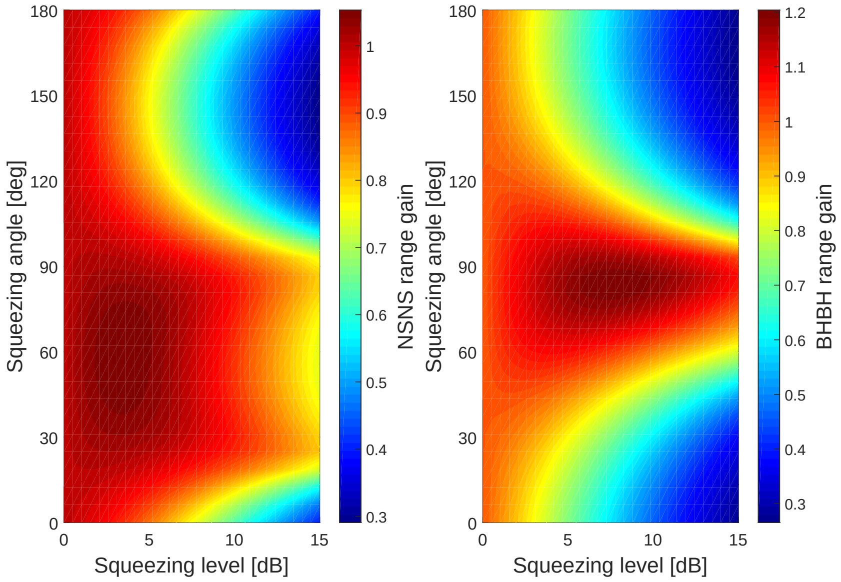

Figure 3.5: NS (left) and BH (right) coalescence ranges gain for configuration 1 with $P_{in} = 25$ W as function of the frequency independent squeezing level and angle.

Fig.3.5 shows the ranges gain for configuration 1 with $P_{in} = 25$ W as function of the squeezing level and the squeezing angle. The ranges are normalized on the ranges obtained with the same configuration and input power but without squeezing injection. For both the NS and BH ranges, the squeezing injection enhance the interferometer sensitivity. In particular, the NSNS range has a maximum of 113.1 Mpc with an injection of 3.6 dB of squeezing and a squeezing angle of 62.1°, while, for BHBH range, a maximum of 1183 Mpc is achieved with the injection of 7.8 dB of squeezing at a squeezing angle of 86.9°. These two ranges are higher compared to the best ranges obtained with configuration 1 without any squeezing injection. It is worth to notice that injecting a phase squeezed state at a squeezing angle close to 90° means that we are injecting an amplitude squeezed vacuum state.

The result of injecting a frequency independent phase squeezed vacuum state in an interferometer in configuration 2 (that is dual recycled interferometer with tuned signal recycling cavity) is an enhancement of both the NSNS and BHBH ranges with respect to the ranges obtained in the same configuration but without squeezing. An example for $P_{in} = 25$ W is in Fig.3.6.

In all the previous cases, the ranges are maximized without considering that this maximization usually spoils the high frequency performances of the interferometer. To increase the BHBH and NSNS ranges injecting a squeezed vacuum state while preserving the high frequency performances of the detector, frequency dependent squeezing must be taken into account.

A frequency dependent squeezed vacuum can be obtained starting from a frequency independent squeezed vacuum and injecting it into a detuned Fabry-Perot cavity, the cavity reflection

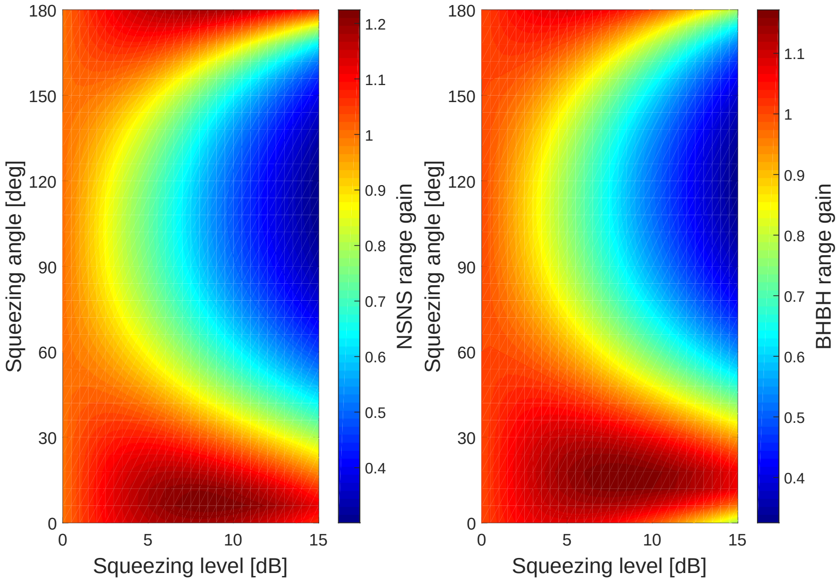

Figure 3.6: Binary ranges for configuration 2 with $P_{in} = 25\,\mathrm{W}$. The highest ranges are: 118.55 Mpc for NSNS systems with an injection of 8.5 dB of squeezing at a squeezing angle of 6° and 1197.9 Mpc for BHBH systems with an injection of 8 dB of squeezing at a squeezing angle of 18°.

is a frequency dependent squeezed vacuum. This cavity is usually called *filter cavity* (FC). To obtain a squeezed ellipse optimal rotation for a GW interferometer, two filter cavities are needed [36].

The study of the injection of a frequency dependent squeezed vacuum into a GW interferometer is not the aim of my work. However, as a view into future developments for a GW detector with squeezing, I computed the sensitivity curve for the particular case of the injection of 10 dB of frequency dependent squeezing with optimal angle rotation into a configuration 2 interferometer with $P_{in} = 125$ W (see Fig.3.7).

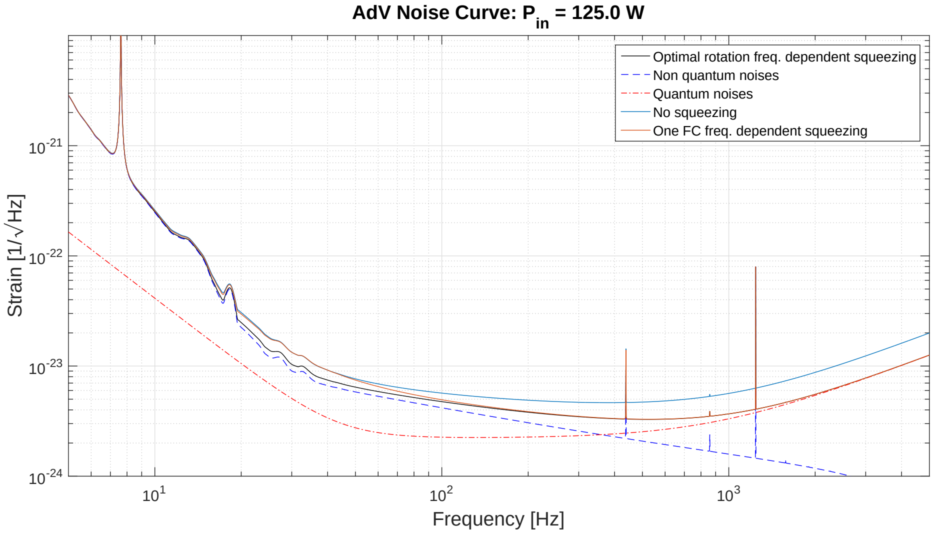

Figure 3.7: AdV noise budged in configuration 2 with $P_{in} = 125$ W with the injection of different types of frequency dependent squeezing. The light blue curve is the AdV noise budget without any squeezing injection, the orange curve is the noise budget with the injection of a non optimal frequency dependent squeezing (as can be realized with just one FC) and the black curve is the noise budget with the injection of a frequency dependent squeezing with optimal ellipse rotation. The blue curve is the noise contribution due to the sum of all non quantum noises; the red curve is the noise contribution due to the sum of quantum noises in the case of frequency dependent squeezing with optimal ellipse rotation.

The FC parameters used to perform the simulations of Fig.3.7 are: length of 100 m with losses of 1ppm/m and end mirror power transmittivity of 1ppm. From the figure is evident that injecting frequency dependent squeezing with optimal ellipse rotation produces limited benefits because of the presence of non quantum noises below ≈ 100 Hz. The non quantum noises that contribute mainly to limit the squeezing benefits are the suspension thermal noise, gravity gradient noise and coating thermal noise. However, the red curve of Fig.3.7 shows that there is large room for improving the AdV sensitivity provided one can reduce the non quantum noises below 100 Hz.

Part II

Experiment

The better is enemy of the good.
Proverbi italiani,
Orlando Pescetti, 1603

Chapter 4

Advanced Virgo squeezed vacuum source

This chapter describes the optical layout along with the electronics and controls of the AdV squeezed vacuum source, with special focus on the parts which I worked on during this thesis. The realization of the first AdV squeezed vacuum source is a collaborative effort involving many italian Virgo laboratories: INFN Napoli, INFN Roma1 (LaSapienza) and INFN Roma2 (TorVergata), INFN Pisa, INFN Genova, INFN Padova-Trento. My group, Padova-Trento, delivered some key subsystems as the Second Harmoic Generator, the Phase Locked Loops, Infrared Mode Cleaner and took a wider responsibility on the implementation of controls and on the integration of the several parts.

Considering the results of the LIGO and GEO600 experiments [4, 5], the collaboration decided to set the following requirements:

- 12 dB frequency-independent squeezed vacuum in the AdV detection band (that is between 10 Hz and 10 kHz). This requirement is as produced, i.e. before measurement losses.
- 10 mrad rms phase noise
- up to 5% losses without taking into account the measurement losses.

4.1 Squeezed vacuum source optical layout

The optical layout of the squeezed vacuum source is schematized in Fig.4.1. The setup can be divided into four main blocks:

Laser sources: it contains three IR laser sources and two phase locked loops (PLL). The main laser (ML) is used to pump the second harmonic generator and to provide the local oscillator for the homodyne detector. The first auxiliary laser (AUX1) provides the coherent control field used to stabilize the squeezed ellipse angle, while the second auxiliary laser (AUX2) is used as the optical parametric oscillator (OPO) length control beam. Two PLLs lock the phase of the two auxiliary laser to the main laser, each one with a different frequency detuning.

Second harmonic source: this block contains a second harmonic generator (SHG), a Mach-Zehnder interferometer (MZ) and a triangular cavity (MCgr). The SHG provides the green

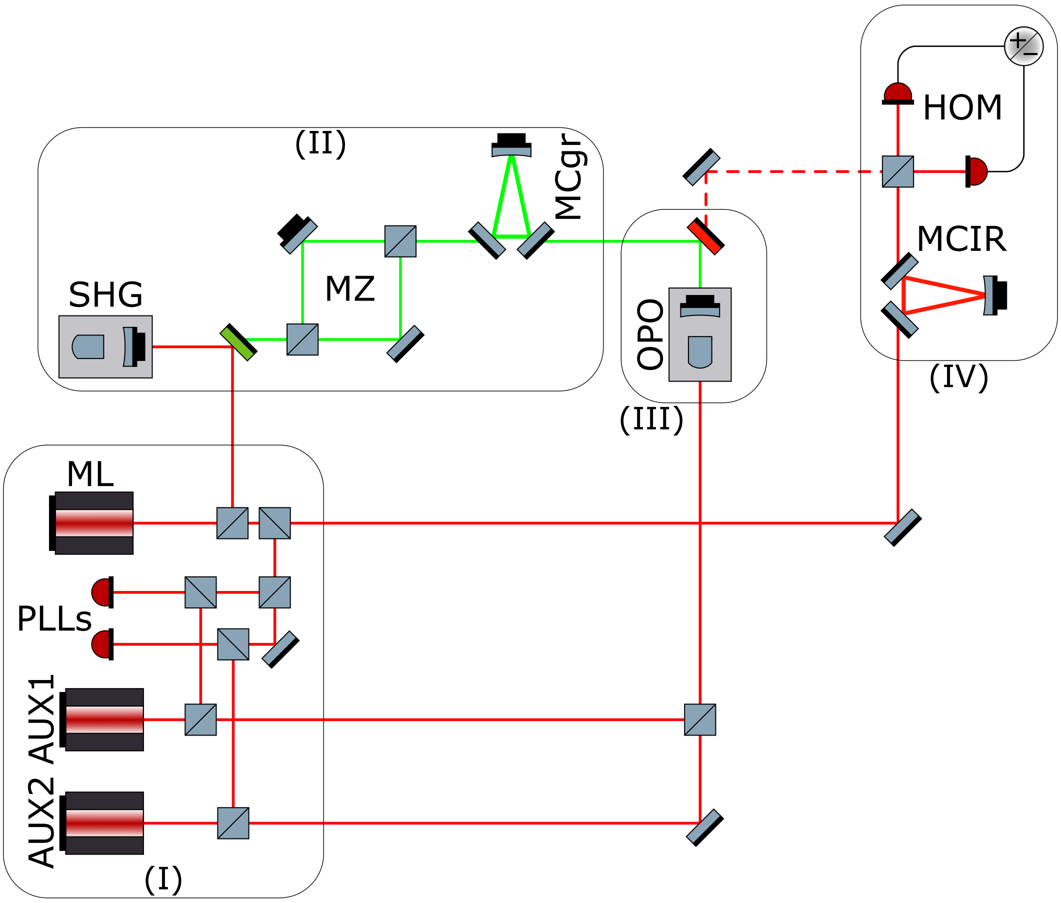

Figure 4.1: Building block scheme of the squeezed vacuum source: (I) is the laser sources, (II) is the second harmonic source, (III) is the squeezed light source and (IV) is the squeezed light detector. To be operational in AdV, the bench main laser (ML) must be phase locked to the AdV laser: this additional PLL is not shown in the picture.

pump power for the OPO, while the MZ stabilizes the pump power and the MCgr stabilizes the phase of the pump field at high frequency[1] and defines the mode shape.

Squeezed light source: it contains the OPO cavity. This cavity, driven below threshold, generates the squeezed vacuum state of light.

Squeezed light detector: this block contains a triangular cavity (MCIR) and the homodyne detector (HOM). The MCIR is used to clean and define the mode shape of the HOM local oscillator and the HOM is used to characterize the produced squeezed vacuum state.

The Napoli group was in charge to develop the Mach-Zehnder interferometer and the green mode cleaner, the Roma1 group developed the homodyne electronic board, the Roma2 group was in charge to realize the OPO cavity, the Pisa group provided a DSP board and the Padova-Trento group was in charge to realize the second harmonic cavity, the infrared mode cleaner and to develop all the electronics and controls needed in the optical bench.

The SHG is fully described in Chapter 5. Here I describe the other main parts of the squeezed vacuum source. The controls of the optical system are described in Section 4.2. Here I just anticipate that two versions of the controls and electronics were implemented during this work and which I call *phase one* and *phase two*.

Fig.4.2 shows a picture of the squeezed vacuum source optical bench as it was at the beginning of May 2016.

4.1.1 Mach-Zehnder (MZ)

The Mach-Zehnder (MZ) interferometer is used to stabilize the power of the green pump to a fixed value. This is needed since a fluctuation of the green pump will lead to a fluctuation of the degree of produced squeezing. Fig.4.3 (left) shows a photo of this setup: it was produced by INFN-NA and I took care of its characterization and control. The MZ consists of two high reflectivity mirrors and two beam splitters.

Fig.4.3 (right) shows the scheme of the electric fields in the MZ interferometer: E_{in} is the input electric field. Referring to this picture, E_R and E_T can be written as

$$\begin{aligned} E_R &= \left(r_1 r_2 - t_1 t_2 \mathrm{e}^{2\pi\imath\frac{\Delta L}{\lambda}+\phi}\right) E_{in} \\ E_T &= \imath\left(r_1 t_2 + t_1 r_2 \mathrm{e}^{2\pi\imath\frac{\Delta L}{\lambda}+\phi}\right) E_{in} \end{aligned} \tag{4.1.1}$$

where r_1 and r_2 are the amplitude reflectivities of the first and the second beam splitter respectively, t_1 and t_2 are the amplitude transmittivities of the first and the second beam splitter respectively, ΔL is the length difference of the two interferometer paths, λ is the light wavelength and ϕ is the difference of the Gouy phases of the two beams at the recombination point.

Usually the contribution of the Gouy phase can be neglected; in particular, it is negligible when $\Delta L \ll z_R$ where z_R is the Rayleigh length of the beam. This term becomes important when the interferometer has length unbalanced arm or if the beam is heavily focused. Our MZ is not in such situations, so in the following we can neglect the Gouy phase contribution.

Our MZ has beam splitters' power reflectivities[2] $R_1 = R_2 = 0.1$ for p-polarized light and $R_1 = R_2 = 0.01$ for s-polarized light. Fig.4.4 shows the MZ total power reflection and power

---

[1] A cavity acts as a low pass filter with a frequency cut equal to the half of its FWHM. Therefore the MCgr stabilizes the phase of the green pump field for frequency greater than the half of its FWHM.

[2] Remind that

$$R = |r|^2 \quad \text{and} \quad R + T + \Sigma = 1$$

where R, T and Σ are respectively the power reflectivity, power transmittivity and losses of a generic surface, and where r is the amplitude reflectivity.

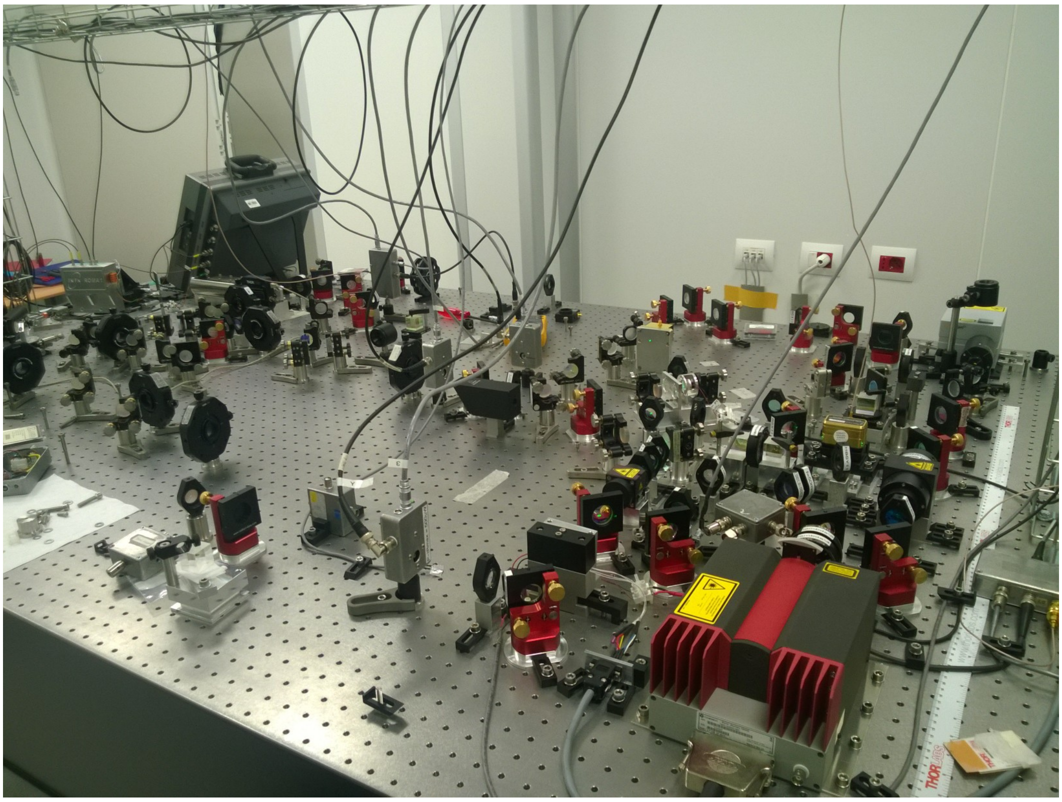

Figure 4.2: Picture of the squeezed vacuum source optical bench as it was at the beginning of May 2016.

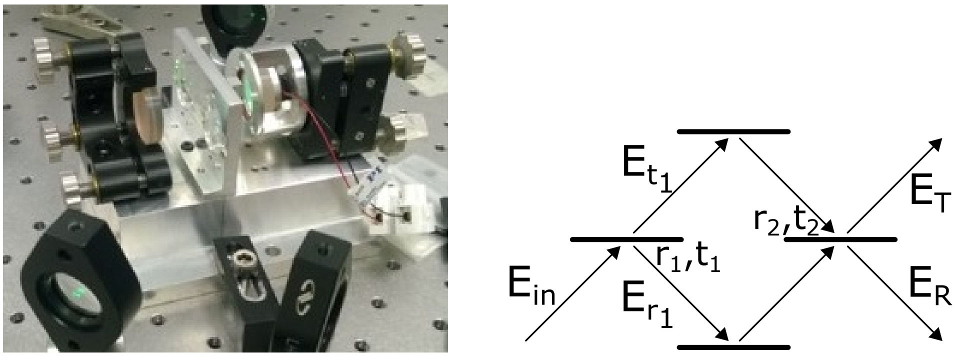

Figure 4.3: (left) Picture of the installed MZ. (right) Working principle scheme of the MZ

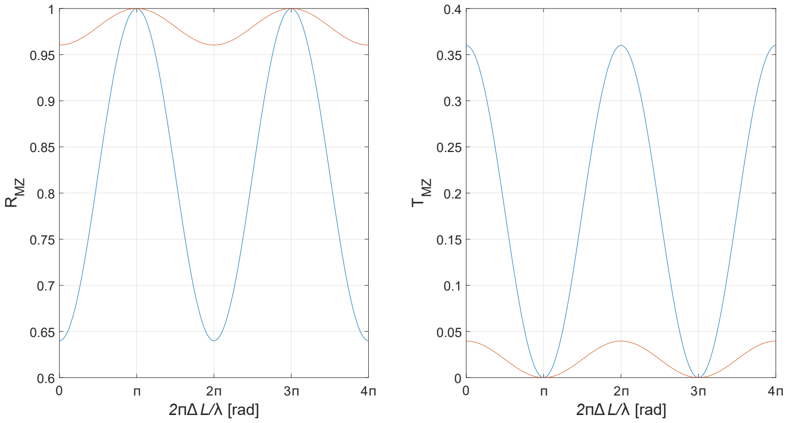

Figure 4.4: Simulation of total power reflection and transmission of the MZ as function of the path length difference. Blue curve is for p-polarized light while orange curve is for s-polarized light.

transmission (defined as $R_{MZ} = |E_R/E_{in}|^2$ and $T_{MZ} = |E_T/E_{in}|^2$). For p-polarized light the mean reflection is $R_{MZ}^{mean} = 0.82$ while for s-polarized light $R_{MZ}^{mean} = 0.98$.

To control the MZ, one of the two mirrors is placed on a piezoelectric ceramic. Acting on the piezo, the difference path length can be actively modified. The error signal is provided by a photodiode that samples the MZ reflected signal (i.e. the beam used as pump for the OPO). The optimal working point to the control loop is when the MZ reflection is linear with the steepest slope, that is, $R_{MZ}^{opt} = R_{MZ}^{mean}$. A scheme of the control loop is in Fig.4.5. The measurements of the MZ transfer function and the MZ open loop transfer function are presented in Fig.4.6 and Fig.4.7 respectively.

The target pump power stability is set at 1% of the power entering the OPO. Fig.4.8 shows a two day measurement of the green pump stability. To perform this measurement, the voltage of the in loop photodiode and the out of loop photodiode (see Fig.4.5) are acquired. The out of loop channel represents the beam that will be injected into the OPO, therefore this channel is the one where the requirement must be fulfilled. After the MZ the measured residual pump power fluctuation is 1.9%. The target is not yet fulfilled; this is mainly due to a low gain of the feedback at low frequency. In the next version of the control, the digital filter will be redesigned

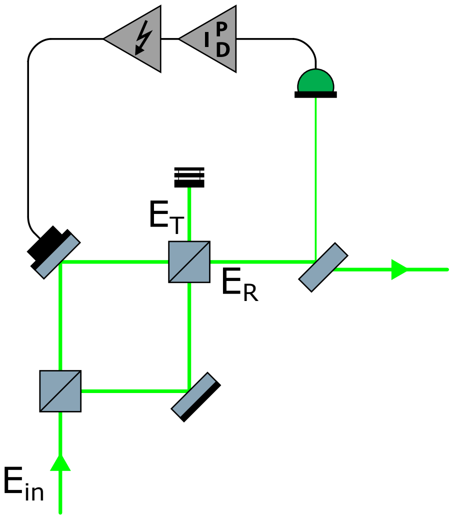

Figure 4.5: Scheme of the MZ control loop. The beam reflected by the second beam splitter of the MZ interferometer is sampled by a beam splitter (with 700ppm reflectivity and diverted to a (in loop) photodiode: the difference of the developed signal with respect to a reference signal is used to control the MZ arm length difference. For the measurements of Fig.4.8, the beam transmitted by the sampling beam splitter was collected by a (out of loop) photodiode.

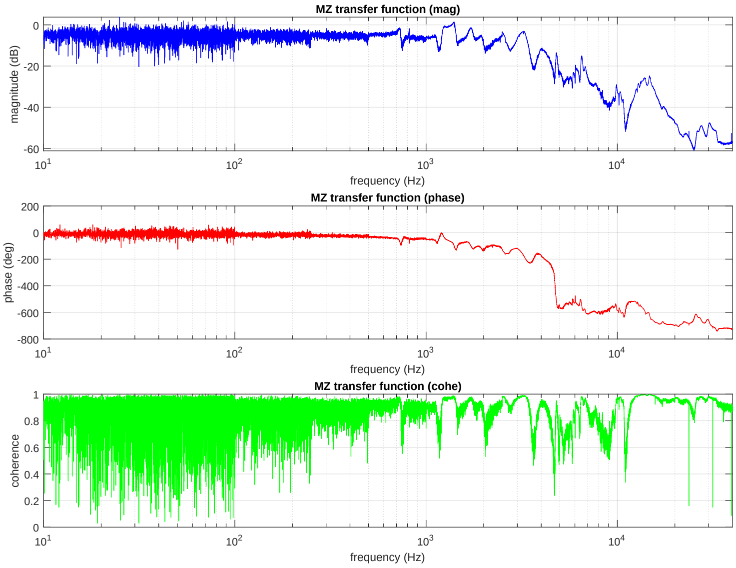

Figure 4.6: Measurement of the MZ transfer function. This transfer function includes the entire control loop except for the servo. A structure is present at high frequency, likely due to mechanical resonances of the MZ interferometer supports.

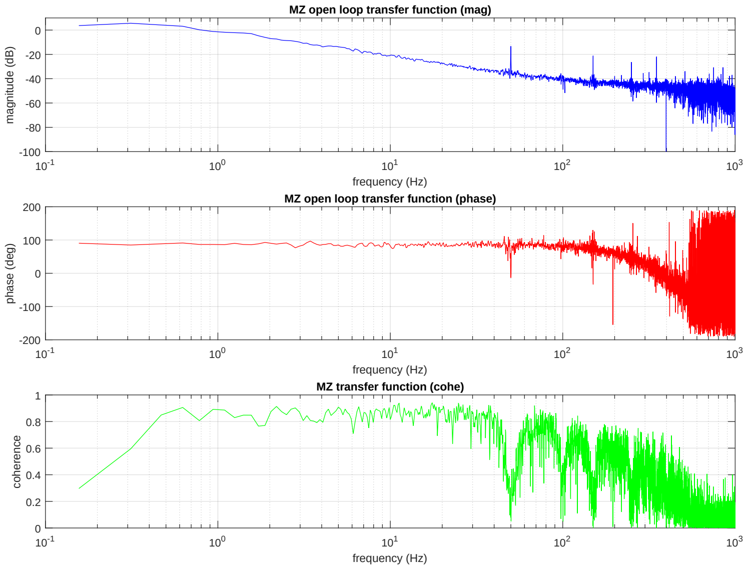

Figure 4.7: Measurement of the MZ open loop transfer function. The unitary gain frequency is approximately 1 Hz and the servo is a standard PI.

to reach the target power stability.

4.1.2 Infrared mode-cleaner (MCIR)

The infrared mode cleaner (MCIR) is one of the two traveling wave cavities present on the optical bench. This resonator is used as an optical low pass filter for high frequency phase noise, moreover it provides mode spatial filtering on the incoming beam and it also works as a polarization filter.

This cavity is placed along the homodyne local oscillator beam path, as close as possible to the homodyne detector. As illustrated in Fig.4.9 (left), this resonator is set up as a three mirror Fabry-Perot ring cavity. Fig.4.9 (right) shows a picture of the IR mode cleaner mounted on the optical bench. The input and output cavity mirror are two identical plano-plano polished mirror with power transmittivity $T_p = 1.25\%$ for p polarized light and $T_s = 700$ppm for s polarized light both at an incidence angle $\theta_i = 45° \pm 2°$. The third cavity mirror is a polished, curved mirror with a radius of curvature of 1 m and a transmittivity of $T = 300$ppm for both light polarizations. The round trip length is 545 mm. The two plano-plano mirror are mechanically attached to a monolithic invar[3] spacer and the curved mirror is mechanically attached to a piezoelectric ceramic, in turn attached to the same invar spacer. This design was adopted to guarantee high mechanical stability and low length fluctuation due to thermal variation. The computed waist size is 389.4 µm in the transverse or horizontal plane and 389.6 µm in the sagittal or vertical plane with respect to the plane identified by the cavity path. The cavity finesse $\mathcal{F}_{s,p}$ can be

---

[3] Invar, also known generically as FeNi36, is a nickeliron alloy notable for its low coefficient of thermal expansion ($\alpha_{th} = 1.2 \times 10^{-6}\mathrm{K}^{-1}$).

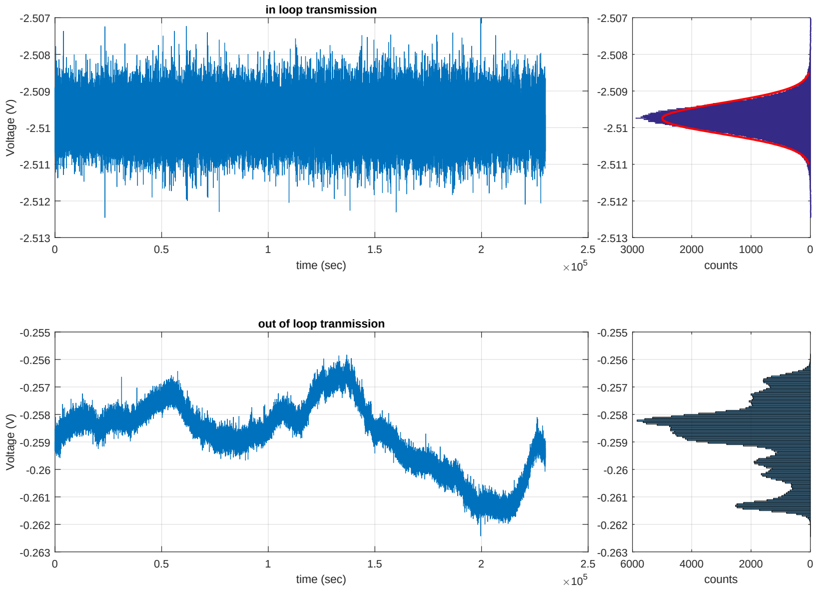

Figure 4.8: Measurement of the green power stability over two days.

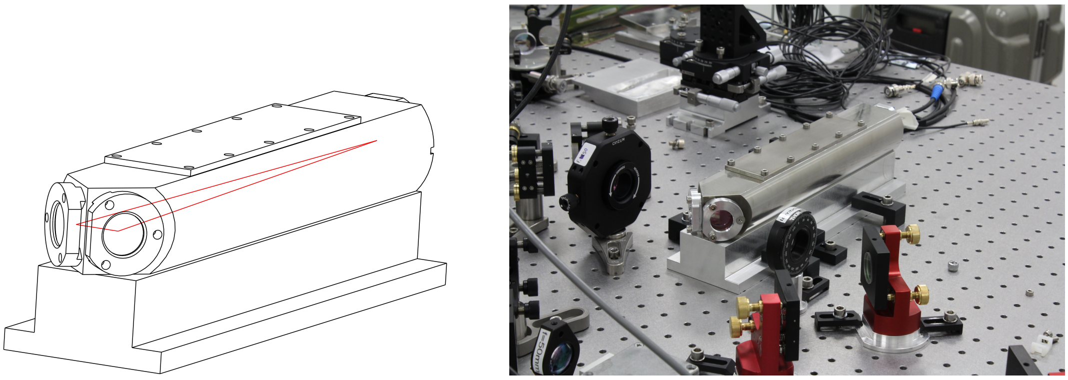

Figure 4.9: (left) Schematic of the IR mode cleaner; in red the optical path of the IR light inside the mode cleaner. (right) Picture of the IR mode cleaner mounted on the optical bench inside the cleanroom at Virgo site.

computed, for s and p polarization respectively, via

$$\mathcal{F}_{s,p} = \frac{\pi (R_1 R_{2s,p}^2)^{1/4}}{1 - \sqrt{1 - R_1 R_{2s,p}^2}} \tag{4.1.2}$$

where R_1 is the power reflectivity of the curved mirror and $R_{2s,p}$ are the power reflectivity of the plano-plano mirrors for the s and p polarization respectively.

In our case, eq(4.1.2) gives $\mathcal{F}_s \approx 3700$ for s polarized light and $\mathcal{F}_p \approx 247$ for p polarized light. Considering the free spectral range (FSR), that is 550 MHz, the cavity linewidth (FWHM) is

149 kHz for s polarization and 2.23 MHz for p polarization.

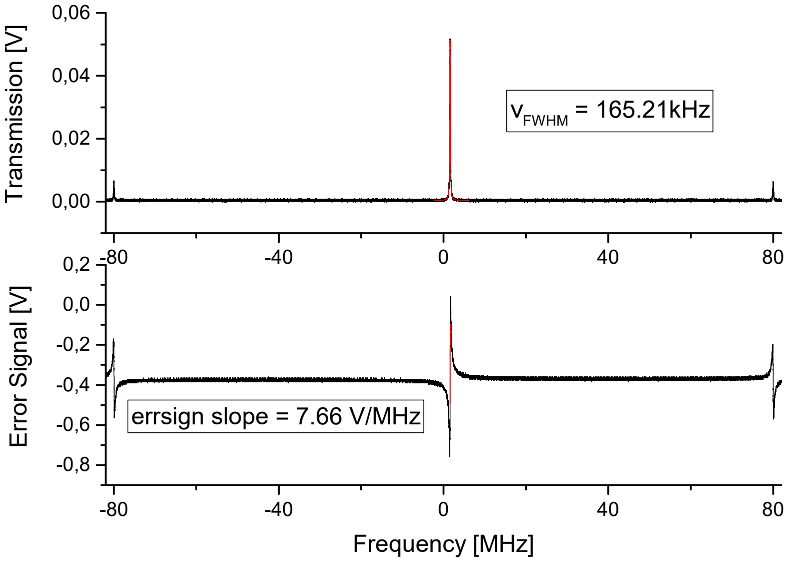

Figure 4.10: Cavity scan near the s pol TEM_{00}. The top line shows the cavity transmission, while the bottom one is the error signal obtained by demodulating at 80 MHz the cavity reflection signal. The transmission peak has been fitted and the FWHM is reported (ν_{FWHM} = 165.21 kHz). The linear part of the error signal has been also fitted to calibrate the error signal.

Fig.4.10 shows a cavity scan of the s pol TEM_{00}. The fitted cavity linewidth is slightly higher than expected. This results in a finesse for s polarization of $\mathcal{F}_s = 3330$. The finesse for p polarization was also measured, giving $\mathcal{F}_p = 205$. Also in this case the finesse is slightly lower than expected.

The infrared mode cleaner is held on resonance to the main laser field using a standard PDH technique. The laser light is phase modulated by an EOM with a frequency of 80 MHz by the same EOM which provides the modulation for the SHG cavity. The cavity reflection signal is acquired by a photodetector and analogically demodulated. The bottom trace of Fig.4.10 shows the demodulated signal obtained with *phase one* electronics.

Fig.4.11 shows the cavity scan of the p pol TEM_{00} demodulated reflection, that is the p pol error signal used to lock the cavity length. The orange curve is the fit of the data performed using equations of [37]. The fit is in good agreement with the experimental data.

Fig.4.12 shows the cavity transfer function of the infrared mode cleaner with *phase one* electronics. On this cavity the *phase two* electronics was tested. In particular the transmission and reflections photodetectors have been upgraded and we migrated the control loop from the commercial PXI system to the SAT group board (see Section 4.2.2).

Fig.4.13 shows the cavity transfer function of the infrared mode cleaner with *phase two* electronics. Comparing this transfer function with the one of Fig.4.12, few differences are visible: the low frequency gain decreased from ≈ 60 dB to ≈ 50 dB and a low pass filter have been removed; all the high frequency features are still present. Since the only component of the loop that hasn't changed is the cavity itself, we can infer that the high frequency resonances are mechanical resonances of the invar spacer and of the piezoelectric ceramic. The red line shown in the top and central panels of the figure, represents the fit of the cavity transfer function. This fit does not take into account the resonances and the model is two first order low pass filter. The

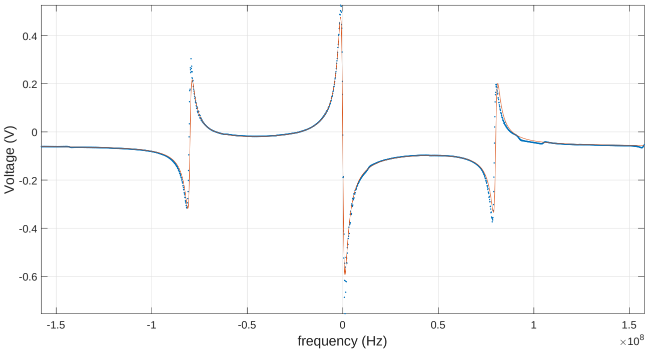

Figure 4.11: Cavity scan of the p pol TEM_{00} demodulated reflection. The blue dot are the acquired data; the orange curve is the fit of the data performed using equations of [37].

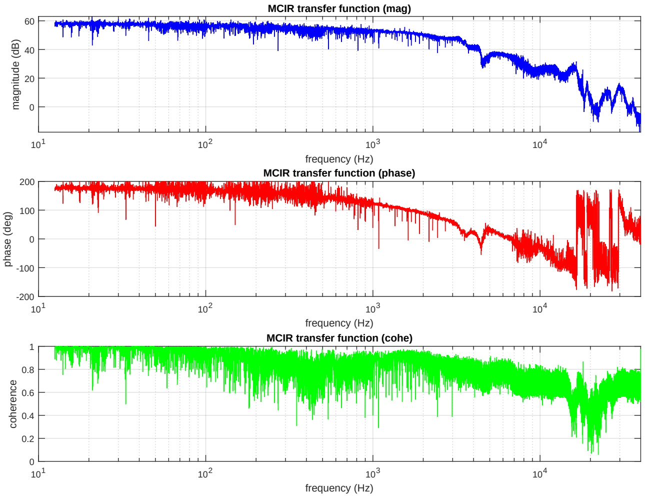

Figure 4.12: Infrared mode cleaner cavity transfer function. For frequencies higher than 2 kHz, some resonances are visible. Those resonances can limit the unitary bandwidth of the control loop. The transfer function is acquired with the cavity locked on p polarization light.

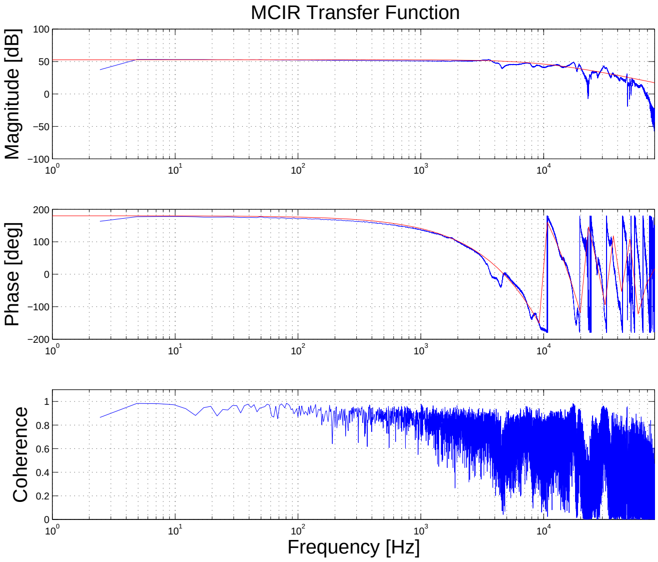

Figure 4.13: Infrared mode cleaner cavity transfer function using *phase two* electronics and controls. The blue curve are experimental data, while the red curve is a fit of the transfer function supposing two first order low pass filter (the two cut frequencies are 6.4 kHz and 17.5 kHz.

cut frequencies are 6.4 kHz and 17.5 kHz; the two low pass filters are due to the high voltage piezo driver. The third low pass filter that was present in the transfer function of Fig.4.12 (with a frequency cut of ≈ 1 kHz) was due to an RC filter after the demodulation stage of the *phase one* electronics.

Fig.4.14 shows the infrared mode cleaner open loop transfer function. The red line is the modeled open loop transfer function and it shows a good agreement with the data. The controller implemented with the SAT board is constituted by a pole at $f_{pole} = 1$ mHz and a zero at $f_{zero} = 2$ kHz and a DC gain of 1000.

4.1.3 Balanced homodyne detector

The balanced homodyne detector is used as diagnostic tool to measure the vacuum squeezing level produced by the OPO. As said at the beginning of the chapter, the development of the electronic board of the homodyne detector has been developed by the Rome1 INFN group. I took care of its integration in the squeezed light source optical bench, the electronic debugging and characterization of the board.

Two typical schemes to realize an homodyne detector are the variable gain design (left panel of Fig.4.15) and the current self subtracting design (right panel of Fig.4.15). In the first one, the two photocurrents are amplified separately by two transimpedence gain stages with different gain, then the two outputs are subtracted. The gain between the two detectors can be varied to optimize balance when subtracting the photocurrents electronically, allowing for the compensation of uneven optical powers and differences in the photodiode responses. In the second design, the two photocurrents are firstly subtracted and then the difference is amplified by a transimpedence gain stage. In this case, the balancing of the optical power and photodiode response differences must be done optically. The advantage of the current self subtracting design with

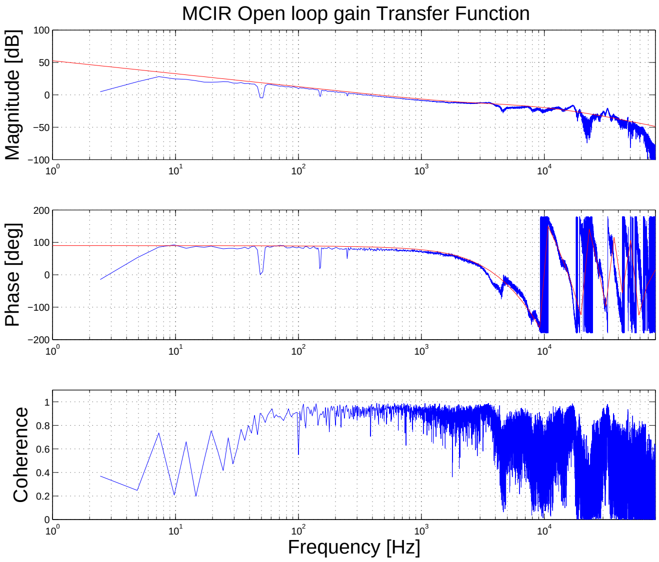

Figure 4.14: Infrared mode cleaner open loop transfer function using *phase two* electronics and controls. The red curve is the model of the open loop transfer function obtained using the cavity transfer function fit of Fig.4.13 and a controller with a DC gain of 1000, a pole at a frequency of $f_{pole} = 1$ mHz and a zero at a frequency of $f_{zero} = 2$ kHz.

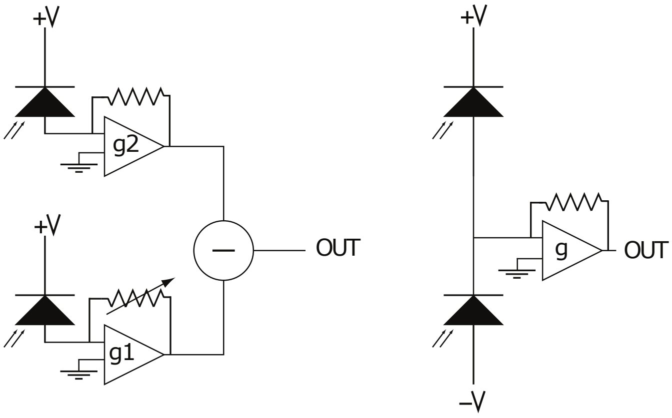

Figure 4.15: Two different electrical schemes for the balanced homodyne detector. (left) Variable gain design: the photocurrents generated by the two photodiodes are amplified separately by two transimpedence gain stages, g1 and g2, then the two outputs are subtracted. (right) Current self subtracting design: the two photocurrent are firstly subtracted and the difference is amplified by a transimpedence gain stage.

respect to the variable gain design is that the second one has reduced classical noise due to the fact that all of the electronic components after the photodiodes are common. The chosen design for our balance homodyne detector is the current subtracting design.

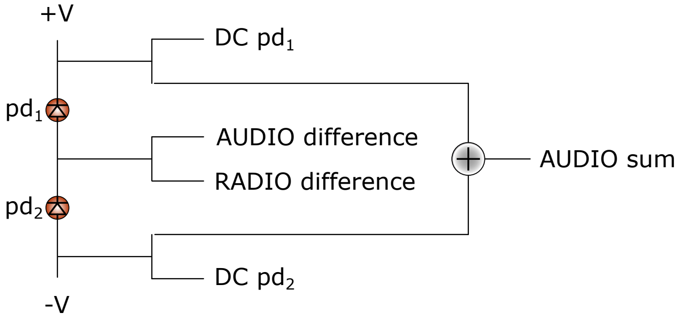

Figure 4.16: Conceptual scheme of the circuit design: the two photodiodes (pd_1 and pd_2) work in reverse bias. Each photodiode has its own DC readout. These two output are used mainly for alignment purpose. The photocurrents of the two photodiodes are selfsubtracted and then amplified. The AUDIO difference channel is band pass filtered between 10 Hz and 10 kHz while the RADIO difference is band pass filtered between 1 MHz and 120 MHz. The AUDIO sum channel electronically sum the two photocurrents after separate amplification and is band pass filtered between 10 Hz and 10 kHz.

Fig.4.16 shows the conceptual scheme of the homodyne circuit design. The homodyne board provides five output channels. Two DC output, one for each photodiode; this two outputs are used uniquely for alignment purpose. An AUDIO difference output; this channel will be used to measure the produced squeezing between 10 Hz and 10 kHz. A RADIO difference output; this channel is band pass filtered between 1 MHz and 120 MHz; this channel will be used to measure the produced squeezing in the RF range and will be also used in the coherent control loop to stabilize the phase of the squeezed field with respect to the local oscillator phase. The AUDIO sum output is the sum of the two photocurrents between 10 Hz and 10 kHz; this channel is used to compute the common mode rejection ratio (CMRR) of the homodyne detector [38].

I will not go into details about the board design since this was not part of my thesis. On the contrary I collaborated into the board debugging and characterization, which I describe in the following. All the characterization has been performed using only the local oscillator beam as input to the homodyne beam splitter, while the other beam splitter input is the coherent vacuum (see Fig.4.1).

Fig.4.17 shows the characterization of one of the two DC channel. The channel shows a saturation for input powers greater than ≈ 7 mW. Below the saturation point the response is linear with a coefficient of 0.33 V/mW. The other DC channel shows the same behavior of the one presented in the figure, but with the linear coefficient equal to -0.33 V/mW and a saturation voltage of -2.55 V. Both outputs are low pass filtered on the board with a $f_{cut} \approx 0.7$ Hz.

I characterized the band pass filter of the two AUDIO outputs. Despite of the designed values, both channels exhibit a high pass frequency cut of 7.1 Hz and a low pass frequency cut of 106 kHz.

To cancel the common mode noise of the two photodetectors (that is the amplitude noise of the local oscillator), the optical power of the two beams after the beam splitter must be balanced. This balancing has been performed adjusting the polarization of the local oscillator with an halfwaveplate. The splitting ratio of the beam splitter depends weakly on the incoming polarization, therefore, the power of the two beam after the beamsplitter can be finely adjusted.

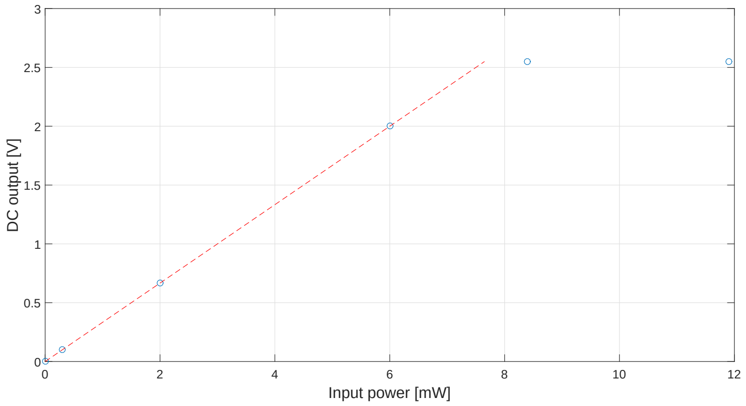

Figure 4.17: Measured output of the DC channel relative to pd_2 of Fig.4.16 as function of the input power measured before the homodyne beam splitter (see Fig.4.1). The data shows a clear saturation of the channel for input powers greater than ≈ 7 mW. Below the saturation point the response is linear with a coefficient of 0.33 V/mW.

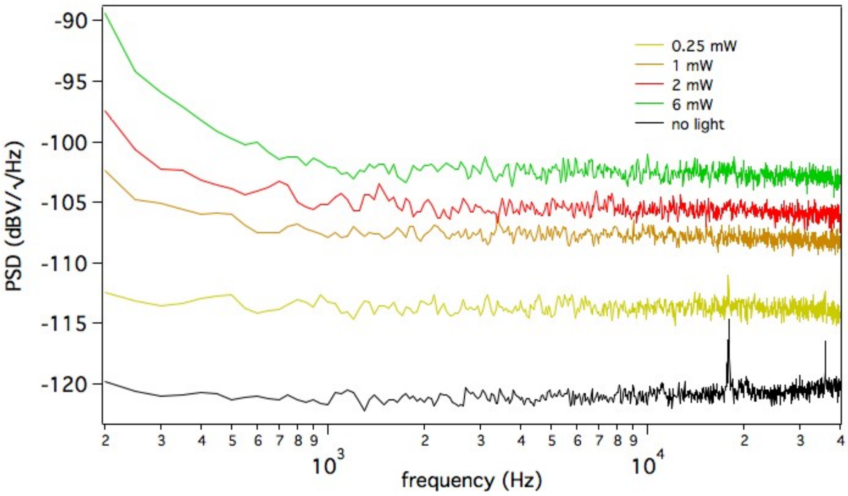

Figure 4.18: Power spectral density of the AUDIO difference output for different local oscillator input power.

The value that measures the common mode noise cancellation is usually called common mode rejection ratio (CMRR) [38]. For our setup, the CMRR is defined as the ratio between the AUDIO difference output and the AUDIO sum output. I measured a flat CMRR of ≈ -80 dB in the whole frequency range of the channel.

Fig.4.18 shows the power spectral density of the AUDIO difference output for different local oscillator input power. The traces are flat as expected from a shot noise limited signal and they scale linearly with the input power. Below ≈ 500 Hz a non stationary noise is present. This noise is due to air flow on the beam after the beam splitter and to stray light. To suppress this two noise sources, the homodyne detector will be housed in a box.

4.2 Controls and electronics

The requirement of a moderate and stable degree of squeezing in the audio band translates into quite high requirements on the controls and electronics both on the noise level and the long term stability. Moreover, when the squeezed light source will be installed in AdV, only remote controls will be allowed. For this reason and to allow maximum flexibility, we chose to use digital electronics for the controls together with analog electronics for the photodetection and the high frequency demodulation. The controls of the bench are listed in the following:

Pound Drever Hall (PDH): four PDH controls are needed (SHG, OPO, MCIR, MCgr);

Temperature stabilization: both the SHG and OPO nonlinear crystal need to be thermally stabilized;

Phase Locked Loop (PLL): two PLLs need to be implemented, one to lock AUX1 to ML and the second to lock AUX2 to ML;

Pump power stabilization: The MZ must be controlled so to stabilize the green field power;

Coherent Control Loop (CCL): this loop stabilizes the low frequency angular drifts of the squeezing ellypse.

Within the electronics, several components need to be realized or optimized:

DC photodiode: low frequency photodiodes are needed as monitor as well as triggers for various loops;

RF photodiode: high frequency photodiodes with embedded demodulation are used for the PDH loops, for the PLLs and for the CCL;

Direct Digital Synthesizer (DDS): DDS provides the RF signals that are necessary for the EOMs, for the RF photodiodes' mixers and for the PLLs;

High Voltage piezo driver (HVpiezo): HVpiezo amplifies by a factor of 100 the correction signal of the PDH loops, the pump power stabilization loop and the CCL.

The electronics and controls of the squeezer optical bench was realized by a two step process:

Phase one: digital commercial electronics based on Labview, integrated by custom electronics;

Phase two: custom and AdV compatible controls and electronics.

In the followings, the two phases are explained.

4.2.1 Phase one: Labview based controls and custom PLL and DDS

The phase one is based on a commercial PXI system. This system is constituted by several components:

- PXI-8106: 2.53 GHz Dual-Core Embedded Controller for PXI;
- PXI-1042Q: General-Purpose 8-Slot Chassis for PXI;
- PXI-4110: Triple-Output Programmable DC Power Supply ;
- APS-4100: Auxiliary Power Source for PXI Programmable Power Supplies;
- cDAQ-9178: USB Data Acquisition Systems;
- NI-9219: Universal Analog Input, 24-Bit, 100 S/s/ch, 4 Ch Module;
- PXI-6259: 16-Bit, 1 MS/s (Multichannel), 1.25 MS/s (1-Channel), 32 Analog Inputs, 4 analog outputs (2.8 MS/s);
- BNC-2110: Shielded Connector Block with BNC.

During this thesis, I implemented various control loop on this system. The temperature stabilization loops and environmental temperatures monitoring involve two NI-9219 units and the PXI-4110 unit. All thermistors are read at a sampling frequency of 1 Hz in 4-wire configuration and the Peltier cell is used as heater never reversing the current source. The loop is based on a standard PID controller and the results are presented in Fig.5.19.

The PDH length stabilization loops are realized with the PXI-6259 unit and two BNC-2110 units. For each cavity (i.e. SHG, MCIR, MCgr and OPO) a photodiode in transmission of the cavity and an analog demodulated photodiode in reflection of the cavity are sampled at a frequency of 10 kHz. The photodiode in transmission is used as trigger for the loop to switch from the cavity scan regime, where the cavity length is linearly changed to scan the FSR, to the locked cavity regime, where the cavity length is locked. The error signal for the locked cavity regime, provided by the analog demodulated photodiode in reflection, is digitally filtered using a PID controller and then fed back to the HV amplifier that drives the cavity piezoelectric actuator. The open loop transfer function of the SHG cavity is presented in Fig.5.14. The other two cavities (MCgr and OPO) have not been locked with the *phase one* electronics.

The MZ length control is realized with the same units of the PDH length stabilization. The aim of this control is to stabilize the green power, produced by the SHG, at a fixed level. After the MZ, the beam is sampled by a beam splitter and the slow frequency signal developed at a DC photodiode is acquired. The error signal of the loop is the difference between the DC photodiode voltage level and a fixed voltage value. This signal is processed by a standard PID controller and then fed back to the HV amplifier that drives the piezoelectric actuator that changes the relative length of the two MZ arms. The measured MZ open loop transfer function is in Fig.4.7 and the green pump stability is presented in Fig.4.8.

The custom electronics developed for the phase one is mainly constituted by the DDS and the PLL board. For this phase, the HVpiezo was supplied by EGO electronic workshop.

The DDS board was developed in collaboration with the INFN-PD electronic workshop and the first version is based on the Analog Devices AD9959 evaluation board. AD9959 chip provides four synchronized DDS channels at 500 MS/s and four 10-bit programmable DACs. The evaluation board of this chip has all the features of the chip itself and is provided with PC evaluation software for control and measurement of the AD9959, USB interface and graphic user interface software (Windows based). The power supply of the board was furnished by a standard NIM rack. AD9959 needs a system clock source that, in our case, is a Wenzel Sprinter Plus 500 MHz oscillator. The channels that drive the EOMs are amplified using MiniCircuit ZHL-3A+ amplifier.

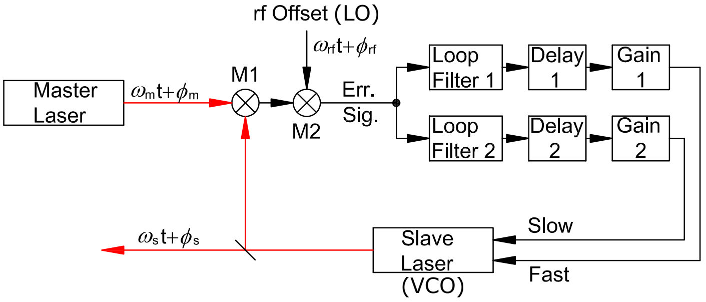

Figure 4.19: Conceptual scheme of an OPLL between two laser.

Before describing the PLL board, I explain how a PLL works. Fig.4.19 represents an ideal optical PLL (OPLL). The target of this control loop is to maintain the frequency and the phase of a slave laser locked to the frequency and the phase of a main laser, possibly with a frequency and phase detuning. In figure, the mixer M1 represent the photodiode where the beat note between the two laser is detected; the mixer M2 compare the beat note to the RF signal that represents the detuning signal. In an ideal and locked OPLL the conditions $\omega_s = \omega_m + \omega_{rf}$ and $\phi_s = \phi_m + \phi_{rf}$ hold true. While the optical part of this system can be simple, the electronic part may be tricky. For the optical part, the beat note signal amplitude is influenced by several parameters; in particular, to maximize the beat note signal the two beams must overlapp: same beam waist and waist position, the wavevectors must be parallel and the two beams must be in the same polarization state. The beat note of the two laser is compared to a signal or local oscillator (LO) using a phase frequency detector (PFD), whose output is proportional to the phase difference. The basic scheme of a PFD is in Fig.4.20 (left). U1 and U2 components are two D ("data" or "delay") flip-flops and U3 is an AND port. The left part of the circuit (before the charge pump) works in the following way: if the output of the two flip-flops is 0 for both, the charge pump is not activated, while if both two outputs are 1, the AND port resets both the flip-flops and again the charge pump is not activated; when the output of the two flip-flops are different, the charge pump is driven and the current flows from V_P to CP or from CP to CPGND depending on which flip-flop is in the 1 state. The charge pump is formed by a voltage generator and two transistors that are driven from the output of U1 and U2. The current pulses generated by the charge pump are converted to voltage by a filter that can be either an active or passive filter or a mixture of both; Fig.4.20 (right) is an example of a passive type of filtering and is the one implemented in our board. The voltage signal generated is fed back to the VCO (voltage controlled oscillator) controls, in our case, the piezoelectric actuator of the slave laser.

Our PLL board was developed in collaboration with University of Bologna and LENS electronic workshop and it is based on the ADF4002 chip. This chip is a Phase Detector/Frequency Synthesizer. It has a bandwidth of 400 MHz and programmable charge pump currents. The filter after the charge pump implemented in this board is a passive filter, formed by the parallel between a capacitor ($C_1 = 33$ nF) and the series of a resistor ($R_1 = 55\boldsymbol{\nabla} \cdot 150\ \Omega$ depending on the setup) and a capacitor ($C_2 = 216$ nF), see right panel of Fig.4.20. The output of this filter

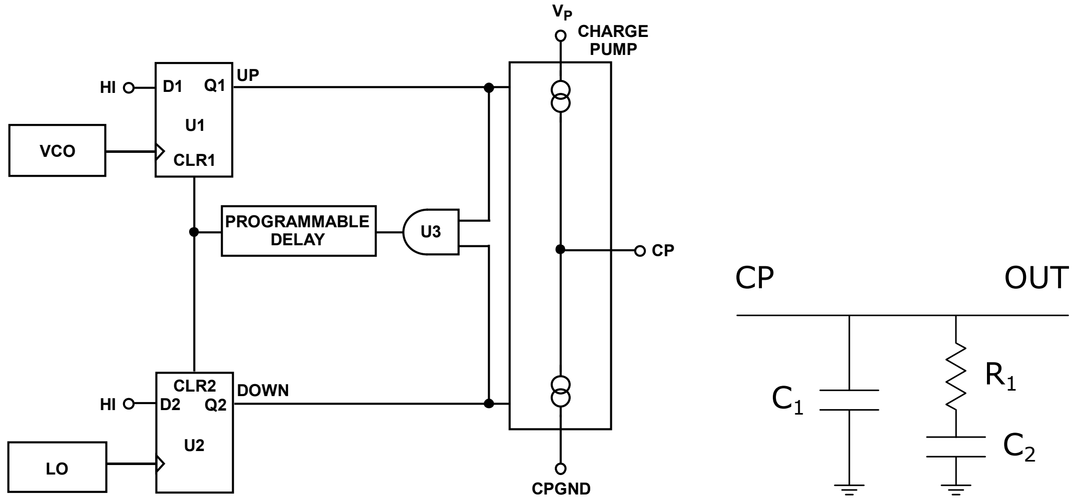

Figure 4.20: (left) PFD basic scheme. (right) passive filtering implemented in the OPLL board after the charge pump.

is then fed to the piezoelectric control of the slave laser. The maximum frequency shift that can be corrected with this setup is defined by the minimum between this two numbers: the laser piezoelectric tuning range, that for our lasers is 130 MHz, and the maximum PFD output voltage multiplied by the laser piezoelectric tuning coefficient, that is 9 V × 2 MHz/V = 18 MHz. Considering that, for stabilized room temperature, the frequency drift of our lasers is of the order of 45 MHz/h, the maximum frequency shift that we can correct is really small. To cure this problem, the SLOW laser control needs also to be used. This control acts on the laser's crystal temperature by means of a Peltier cell, with a tuning coefficient of 3 GHz/V and a frequency bandwidth of $\approx$ 1 Hz. The output of the PFD is sampled by the ADC of the micro-controller ATmega328. Inside the micro-controller, the PFD output signal is maintained in the middle of its dynamic range by a digital PI. The generated correction signal is converted by a 16-bit DAC (AD5663) and fed to the laser SLOW control. With all the above implemented the PLL board, the long term stability of the loop is ensured. A long term measurement is presented in Fig.4.21.

The residual phase noise target for the PLL is $\phi_{res} < 10$ mrad rms integrated between 8 Hz and 100 kHz. The residual phase noise is the integral below the power spectral density of the photodetector output after being analogically demodulated at the LO frequency by a mixer. The PLL ϕ_{res} has been measured for two different conditions and the results are presented in Fig.4.22. In the figure, three sets of measurement are presented; they are taken with two different setups of the PLL board (setup A, B), the two differ by the charge pump current ($I_{cpA} = 1.91$ mA and $I_{cpB} = 1.22$ mA) and the filter resistance ($R_{1A} = 150\ \Omega$ and $R_{1A} = 55\ \Omega$), see Fig.4.20 (right). Moreover, the simulation of both the configuration is shown. In the setup B, the expected residual phase noise is 17.6 mrad while the measured one is 19.2 mrad; in the setup A, the expected residual phase noise is 7.9 mrad while the measured is 11.4 mrad for the measurement A1 and 9.3 mrad for the measurement A2.

4.2.2 Phase two: AdV compatible controls and electronics

The main target of phase two is the migration from the PXI based system, to a custom and AdV compatible system. Since this migration is currently ongoing, in this thesis I present it shortly.

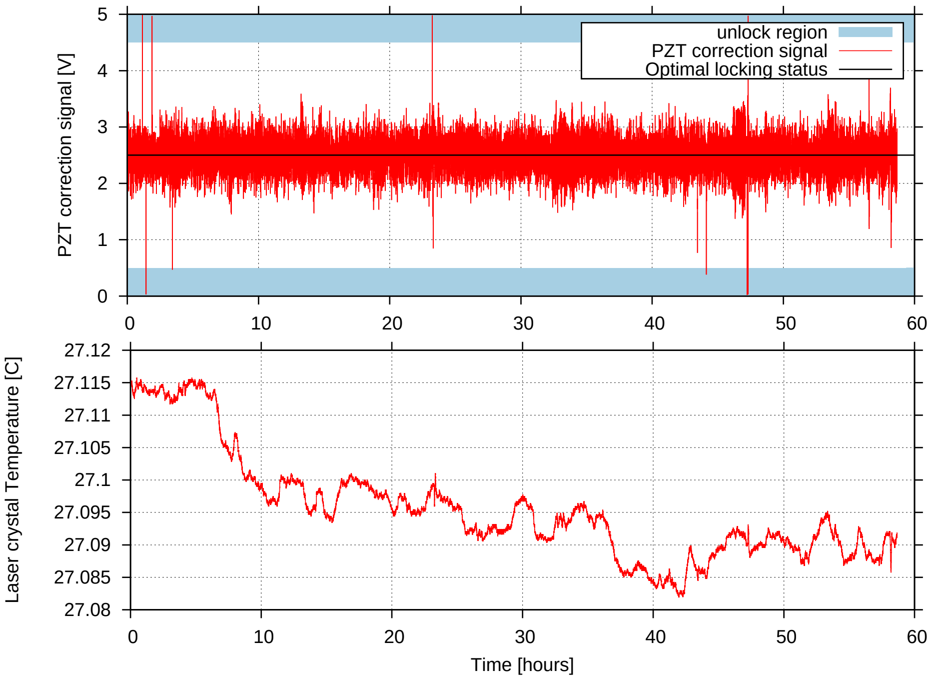

Figure 4.21: Long term stability measurement of the PLL board. The upper time stream is the PFD output sampled by the micro-controller, while the bottom one is the laser's crystal temperature.

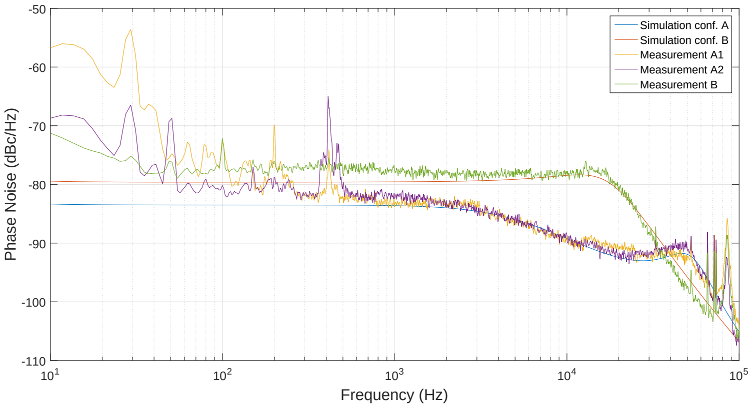

Figure 4.22: Residual phase noise of the OPLL.

In phase one, the PDH loops and the pump power stabilization loop were implemented using the PXI system. In this phase, these loops will be realized using a board developed by the AdV SAT group (INF-PI). This board was independently developed for the control of the mechanical degree of freedom of the AdV superattenuators (SAT) by the AdV INFN Pisa group.

The SAT board crucial components are: a commercial DSP and two FPGA, 6 DAC and 6 ADC (differential, 24-bit at 320 kS/s each) and a fiber transceiver. The communication to the AdV data acquisition (DAQ) system is performed via fiber but all the computations are performed internally (mainly in the DSP and in one of the two FPGA while the other FPGA take care of the communication with the ADC and DAC). The boards are programmed using a code developed by the SAT group and the communication is via Ethernet connection.

The temperature control of the nonlinear crystals, that in phase one was performed by the PXI system, in phase two will be performed by stand-alone boards. The basic scheme of this board (named Peltier driver) is presented in Fig.4.23. The NTC thermistor is inserted into a voltage divider with a resistence R. The aim of this voltage divider is to linearize the response of the thermistor in the range of temperatures where $R_{NTC}(T) \approx R$. In our board $R = 9.1$ kΩ ($\pm 0.05\%$, ± 10ppm/°C), thus the operating temperature is $T_0 = 30$ °C.

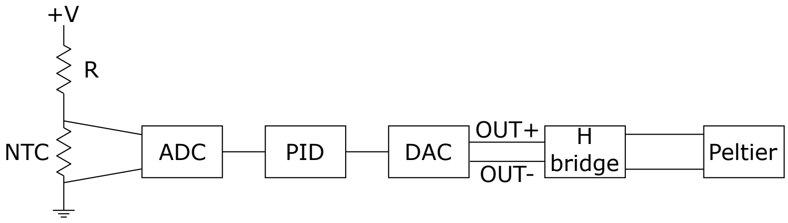

Figure 4.23: Basic scheme of the Peltier driver.

The voltage difference across the NTC thermistor is digitized using a 24-bit ADC (AD7745) and acquired by an ATmega328 micro-processor. The acquired voltage signal is transformed into a temperature signal and processed by a digital PID filter. The 16-bit DAC (AD5667R) outputs the correction signal to the Peltier cell as a PWM signal. The used DAC has two different output so that the Peltier cell can either be heated up or cooled down. On the contrary of what done with the PXI system, the Peltier is used as heater as well as cooler. The current flow is reversed by the H bridge that is driven by the DAC two outputs.

The second version of the DDS is based on the AD9910 chip. Compared to AD9959, this chip provides only one DDS channel at 1 GS/s and one 14-bit programmable DAC. Moreover it has better phase noise performances and longer word to define phase and frequency of the channel (32 bit instead of 24 bit). On each new board, four AD9910 have been installed and PLL locked between each other (channel 2 is the master channel). As in the previous version, the power supply of the board is provided by a standard NIM rack and the channels that drive EOMs are amplified using MiniCircuit ZHL-3A+ amplifier. Since the phase noise performances of the DDS are influenced by the phase noise performances of the system clock source, the Wenzel Sprinter Plus 500 MHz oscillator has also been upgraded. The two main issues that degrade the phase noise performances of the majority of local oscillator are the thermal stabilization of the crystal and the power supply fluctuations. Wenzel oscillators have embedded stabilization of the crystal temperature; to cure the power supply fluctuation, in phase two we installed a low noise voltage regulator (LNVR-15-12-2-1) that provides 12 V with few nV/$\sqrt{\text{Hz}}$ voltage noise. Fig.4.24 shows the phase noise measurement of the latest DDS board.

In the new version of the PLL board, few upgrades will be implemented. The major one is the auto-lock system. A spectrum analyzer will be added to the board so to extend the

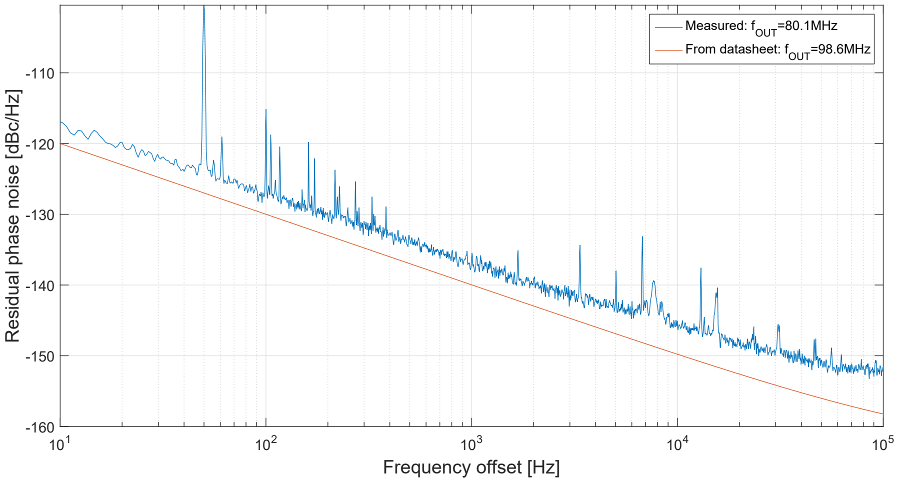

Figure 4.24: Residual phase noise of the DDS board based on AD9910 chip. The measurement is performed at $f_{OUT} = 80.1$ MHz (blue trace), while the orange trace is the residual phase noise of the chip at $f_{OUT} = 96.8$ MHz as expected from the AD9910 datasheet.

"capturing range" of the signal up to ≈ 5 GHz. Another upgrade will be the implementation of a 5-th order bandstop filter on the laser's piezoelectric correction signal. The aim of this filter is to decrease the amplitude of the correction signal in the frequency range where piezo's mechanical resonances are present (100 kHz – 200 kHz) so to have the possibility to extend the PLL frequency bandwidth. This filter was present also in the first version of the board, but was never used. Another thing that limits the PLL bandwidth is the filter after the charge pump. In this version, an optimization of this part of the circuit will be performed.

Chapter 5

Second Harmonic Generator

The Second Harmonic Generator (SHG) is one of the two non-linear stages of the experiment and is used to convert energy from frequency ω_0 to the new frequency $2\omega_0$. The working principle was first demonstrated in 1961 with a Q-switched ruby laser with a conversion efficiency of $2 \cdot 10^{-8}$ [31]. Since then the technique has advanced and conversion efficiency up to 89% have been demonstrated for continuous wave systems[39].

In this thesis we use the same SHG scheme of [39] because it has been demonstrated to have high conversion efficiency, high frequency stability and excellent long-term stability [4].

Another benefit of the SHG scheme with an IR cavity is that the latter provides a spatial filtering of the IR beam, if the higher order modes are not degenerate with the TEM_{00} mode. This translates into spatial filtering of the green field since it inherits the spatial features of the IR beam.

5.1 SHG requirements

The IR source of the SHG is provided by a Mephisto Coherent laser with nominal output power of $1W$. The OPO threshold power will be in the range of $70mW$. From the experience of the GEO group [40], we expect that after years of continuous operation, the non-linear gain of the non-linear crystal inside the OPO will drop and the OPO threshold power will increase. For this reason, and to have the possibility to run the OPO above-threshold, we require our SHG to provide at least $100mW$ of green ($532nm$) power in the TEM_{00}.

In our setup we use a periodically poled crystal to exploit the possibility to have a high non-linear susceptibility and low phase matching temperature[1]. For audio band squeezers, the most used PP material is the periodically poled potassium titanyl phosphate (PPKTP - KTiOPO_4) which has been demonstrated to have good long term performances and to be robust against green induced infrared absorption (GRIIRA) [41]. PPKTP is thus our choice; typically the poling period is $9\mu m$ which corresponds to a phase matching temperature of $\approx 310K$.

Low IR contamination

As said, the green field produced inside the SHG pumps the OPO. Therefore a crucial issue is the IR contamination of the green beam[2]. To avoid this problem we use two different solutions.

---

[1] This point will be crucial in the case of a vacuum compatible setup.

[2] An IR field entering the OPO through the green beam will act as a seed for the squeezer cavity and it will introduce low frequency noise in the squeezed field.

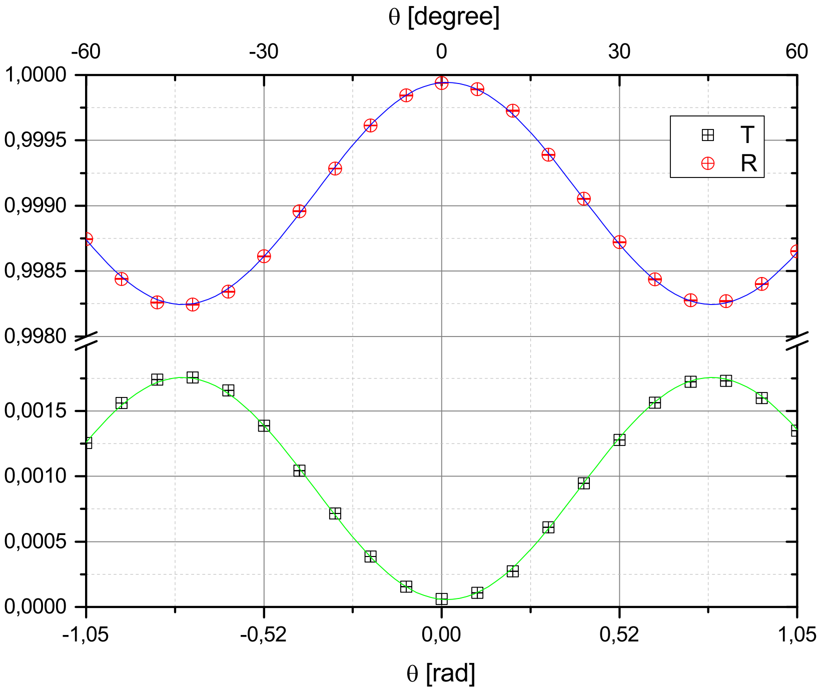

Figure 5.1: Measurements on HBSY11 (Thorlabs). The IR ($1064nm$) power reflectivity and trasmittivity are plotted as function of the polarization angle θ of the incident field. s-polarized light is at $\theta = 0$. The lowest IR transmittivity ($56 \pm 5ppm$) is achieved for s-polarized beam.

Dichroic mirror cascade Dichroic mirrors (also called harmonic beamsplitter) are widely used to separate spatially light beams of different frequency. Fig.5.1 shows measurements on an harmonic beam splitter (Thorlabs - HBSY11). Depending on the polarization of the incident beam (at 45° incident angle), this component exhibits very low IR transmittivity, with a minimum of (56 ± 5)ppm for vertically polarized field. In the AdV squeezer, a cascade of dichroic mirrors will follow the SHG cavity along the green field path. The first dichroic mirror after the SHG cavity is one of the two steering mirrors used to align the cavity itself. Three mirrors are necessary to reduce the IR contamination of the green field below 10^{-13}W for 1 W of IR input power. This is enough to reduce to a negligible level the noise introduced into the squeezed state by the IR seed. Three dichroic mirrors are also used in the GEO600 squeezer [42].

Cavity reflection tuning Ref.[43] shows that the values of several parameters can change the IR reflection from a cavity enhanced SHG. In particular, we tune the IR power reflection of the cavity incoupling mirror.

In our setup we use both the *Dichroic mirror cascade* and the *Cavity reflection tuning* methods in order to lower the IR contamination of the green beam.

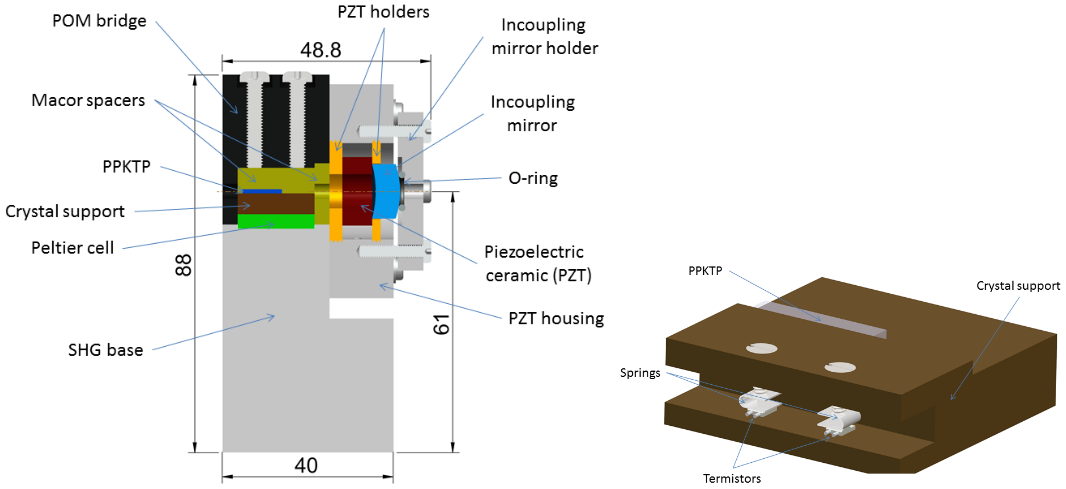

Figure 5.2: SHG cavity mechanics. Left: SHG vertical section. The cut plane contains the cavity optical axis. Right: Dry assembly of the two termistor.

5.2 Mechanics

The main target of the mechanical mount of the SHG cavity is to provide a mechanically stable housing for the PPKTP crystal and for the incoupling mirror. Since the length fluctuations cause phase fluctuations both on the IR beam and therefore on the green produced light, a robust mechanical housing is required. Moreover, a good thermal stabilization is required for the nonlinear crystal phase matching condition.

To ensure a good thermal contact, the crystal is placed on a OFHC copper element that is thermally connected to the Peltier element. Moreover, the crystal is surrounded by a indium foil and an indium foil has been inserted between the Peltier cell and the copper element. This two last solutions ensure a good thermal conductivity from the Peltier to the PPKTP. Two NTC thermistors are mechanically attached to the copper element. Since greases and glues needs to be avoided, the thermal contact between the thermistors and the copper element is ensured by two copper-berillium springs (see Fig.5.2 right).

The incoupling mirror of the cavity is placed on a piezoelectric actuator. The elastic element that act against the piezo is a viton o-ring. The cavity length can be manually changed moving the two brass spacers that keep the piezo in position, this degree of freedom allows a length change up to 3 mm but is feasible only before aligning the cavity.

To proper align the incoupling mirror and crystal optical axis, the aluminum piezo housing component must be moved perpendicularly to the laser propagation axis. This movement is ensured by the presence of a teflon foil between the piezo housing and the SHG base attached to the POM bridge. Once the cavity is aligned, the mechanical stability holds thanks to four screws that keep the piezo housing in position respect to the SHG base and POM bridge.

In Table 5.1 all the pieces and relative materials are listed.

Object name	Material
SHG base	Aluminum
Crystal support	Oxygen-free high thermal conductivity (OFHC) copper
Macor spacers	Macor
POM bridge	Polyoxymethylene (POM)
PZT holders	Brass
Incoupling mirror holder	Aluminum
O-ring	Viton
PZT housing	Aluminum
Springs	Copper-Berillium

Table 5.1: List of different pieces and relative materials composing the SHG cavity holder. The pieces' name refers to Fig. 5.2.

5.3 Double pass measurements

To obtain the parameter used to realize the in cavity SHG, the single-pass nonlinear conversion efficiency must be measured. From [44] this parameter is defined as follows

$$E_{NL} = \frac{P_2}{P_1^2} \tag{5.3.1}$$

where P_1 is the fundamental pump power (1064 nm) and P_2 is the second harmonic generated power (532 nm). Unfortunately, due to the fact that our PPKTP crystal has an high-reflectivity (HR) coating on the curved side, E_{NL} must be measured performing a double pass SHG.

For the double-pass scheme, the second-harmonic power is represented as [45]

$$P_2 \propto \left| \int_0^L \left[\frac{e^{\imath \Delta k z}}{1 - 2\imath \dfrac{z - z_0}{b}} + e^{\imath\phi + \imath \Delta k L} \frac{e^{\imath \Delta k z}}{1 - 2\imath \dfrac{z - (L - z_0)}{b}} \right] \mathrm{d}z \right|^2 \tag{5.3.2}$$

where L is the crystal length, z_0 is the distance between the entrance surface of the crystal and the beam waist, $b = k w_0^2$ is the confocal parameter, w_0 is the radius of the beam waist and ϕ is the phase shift between the first and the second harmonics.

For plane waves ($b \to \infty$), the second harmonic produced power is

$$P_2 = 4 P_2^{max,SP} \operatorname{sinc}^2 \left(\frac{\Delta k L}{2} \right) \cos^2 \left(\frac{\phi + \Delta k L}{2} \right) \tag{5.3.3}$$

where $P_2^{max,SP}$ represents the maximum second harmonic power achievable in the single pass configuration (once defined L and Δk). Fig.5.3 shows eq(5.3.3) for different phases ϕ.

Our case is slightly more complicated since we cannot use the approximation of plane wave and the HR coated surface of the crystal is curved ($RoC = 8$ mm). Boyd and Kleinman demonstrated [46] that for focused beam, the optimum second harmonic conversion is obtained with $z_0 = L/2$ and $b = L/2.84$ that in our case means a beam waist equal to $w_0 = 23.55$ µm. Fig.5.4 shows the second harmonic production as function of the beam waist position inside the crystal. As expected, the maximum is reached with the waist in the middle of the crystal. The simulation takes into account also the effect of the curvature of the HR surface.

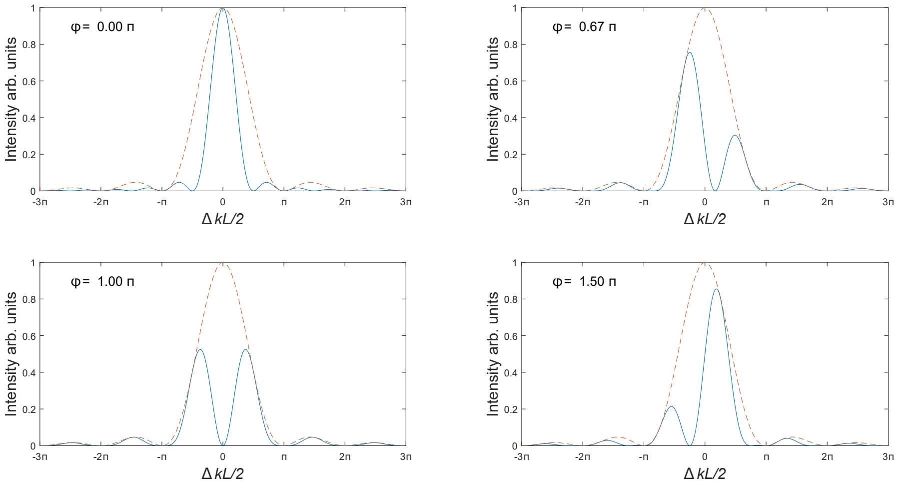

Figure 5.3: Double pass quasi phase matching for different ϕ (eq(5.3.3)). Dashed curve is the single pass phase matching multiplied by a factor of 4.

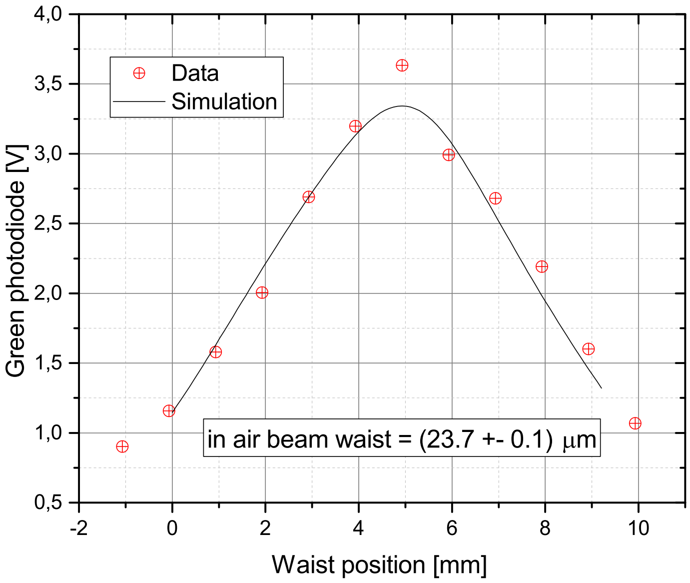

Figure 5.4: Green production as function of beam waist position inside the PPKTP. The black line is the numerical solution of eq(5.3.2) as function of the waist position inside the crystal (z_0).

Having the beam waist dimension and position optimized, the phase ϕ has been optimized overlapping the reflection from the HR coated surface with the entering IR beam. The results are shown in Fig.5.5. This figure represent the quasi phase matching of the double pass second harmonic generation. The optimal crystal temperature is $T_{opt} = 305.2$ K. Since the conversion

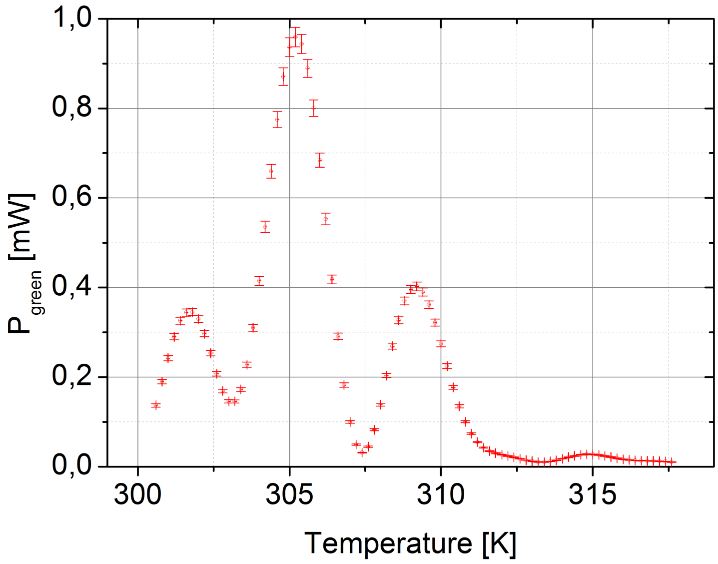

Figure 5.5: Double pass quasi phase matching after alignment and waist position optimization. The quasi phase matching is obtained varying the temperature of the PPKTP crystal using the peltier cell. The temperature is measured by an out of loop thermistor. IR pump power $P_1 = 200 \pm 11$ mW

efficiency is pretty low, therefore the green absorption and the consequent crystal heating are negligible, T_{opt} remain constant over all the range of input IR power used to characterize the double pass SHG.

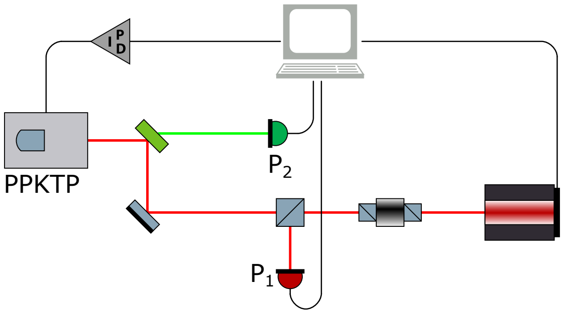

Figure 5.6: Double pass scheme basic experimental setup. *Descrivere il setup.*

The input power has been changed feeding a DC signal to the pump diode of the IR laser. A basic scheme of the measure is presented in Fig. 5.6. Using this setup, the green produced light has been measured while varying the crystal temperature in a small range across T_{opt} and varying also the pump diode current of the laser. The measure has been performed in a steady state regime.

The results are in Fig.5.7. The fit of the data with eq(5.3.1) results in $E_{NL} = (2.33 \pm 0.01) \cdot 10^{-2}$ W^{-1}

with a reduced-$\chi^2 = 0.35$.

In the figure are clearly visible three "bumps" that are not compatible with the fitted law. The explanation of this behavior is demanded to the next section.

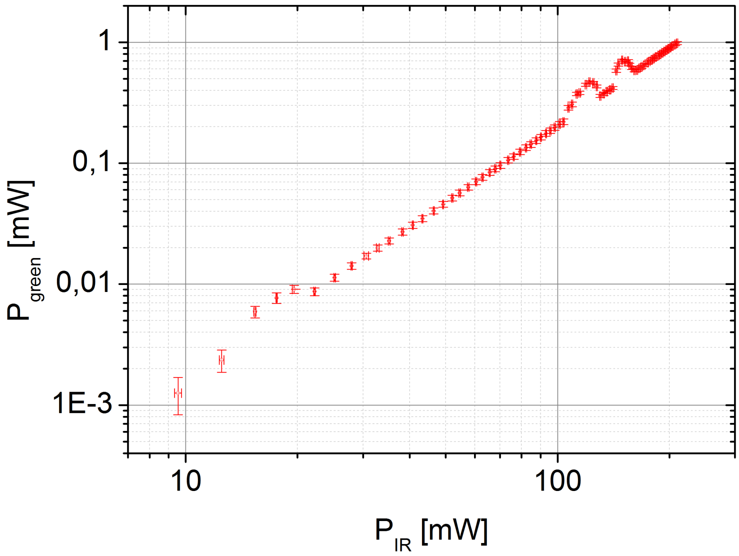

Figure 5.7: Double pass green production. Fitting the data with eq(5.3.1) results in $E_{NL} = (2.33 \pm 0.01) \cdot 10^{-2}\ \mathrm{W}^{-1}$ with a reduced-$\chi^2 = 0.35$. The three bumps have been excluded from the fit. They originate from a different process, as explained in Sec.5.3.1.

5.3.1 Multimode SHG

Here I consider the multimode SHG and, following the explanation found in [47], I focus on the case of a two mode laser ($N = 2$): i.e. a laser whose output is the sum of two frequency component.

Let's have ω_1 and ω_2 the frequencies of the two laser mode ($\omega_2 > \omega_1$). We neglect the variation of the transverse beam profile over the range of frequencies contained in the fundamental beam. This means that all modes are assumed to have the same transverse spatial structure. We define

$$\omega_0 = \frac{\omega_1 + \omega_2}{2} \qquad \text{and} \qquad \Delta\omega = \omega_2 - \omega_1 \tag{5.3.4}$$

therefore ω_1 and ω_2 can be rewritten as

$$\begin{aligned} \omega_1 &= \omega_0 - \Delta\omega/2 \\ \omega_2 &= \omega_0 + \Delta\omega/2 \end{aligned} \tag{5.3.5}$$

To describe the fundamental and the second harmonic generated field inside the crystal, it is convenient to introduce a dimensionless field amplitude α_m and a fractional mode power p_m for the mth mode in the fundamental beam by

$$p_m = |\alpha_m|^2 = \frac{\epsilon_0 c n_f \pi w_0^2}{4P} |E_m|^2 \qquad \text{with} \quad m = 1, 2 \tag{5.3.6}$$

where n_f is the refractive index of the crystal at the frequency of the fundamental beam ($n(\omega_1) = n_f \approx n(\omega_2)$), w_0 is the beam waist and P is the total power of the fundamental beam. The second harmonic field E_{sh} must obey the equation

$$\frac{\partial E_{sh}}{\partial z} = \frac{\imath \omega_0 d}{n_{sh} c} \sum_{m=1}^{N} \sum_{m'=1}^{N} E_m E_{m'} e^{\imath \Delta k_{mm'} z} \times \delta(\omega_m + \omega_{m'} - \omega_{sh}) \tag{5.3.7}$$

where n_{sh} is the crystal refractive index at the second harmonic frequency and $\Delta k_{mm'} = k_m + k_{m'} - k_{sh}$. In the summation of eq(5.3.7), only those modes for which $\omega_m + \omega_{m'}$ has a definite value ω_{sh} contribute. In our case

$$\omega_{sh}^{(1)} = 2\omega_1 \qquad = 2\omega_0 - \Delta\omega \tag{5.3.8a}$$
$$\omega_{sh}^{(2)} = 2\omega_2 \qquad = 2\omega_0 + \Delta\omega \tag{5.3.8b}$$
$$\omega_{sh}^{(3)} = \omega_1 + \omega_2 \qquad = 2\omega_0 \tag{5.3.8c}$$
$$\omega_{sh}^{(4)} = \omega_2 + \omega_1 \qquad = 2\omega_0 \tag{5.3.8d}$$

therefore, there are three different second harmonic modes produced while pumping the process with two distinct fundamental modes. If $p_1 = p_2 = 0.5$, half of the total second harmonic power is hosted in the central mode ($\omega_{sh} = 2\omega_0$) and the other half is equally divided into the other two modes. Now let's consider the phase matching of the process. If we suppose that the second harmonic process' phase matching is optimized for the central frequency ω_0, like in [47], it exists an optimal bandwidth for which the phase matching condition is nearly fulfilled for all the modes. Using the data for the refractive index variation of the PPKTP [48], the acceptance bandwidth is 10^{11} rad/s, that is 16 GHz; as we will see in few moments, the frequency distance of our modes is $\Delta\nu \approx 3GHz$.

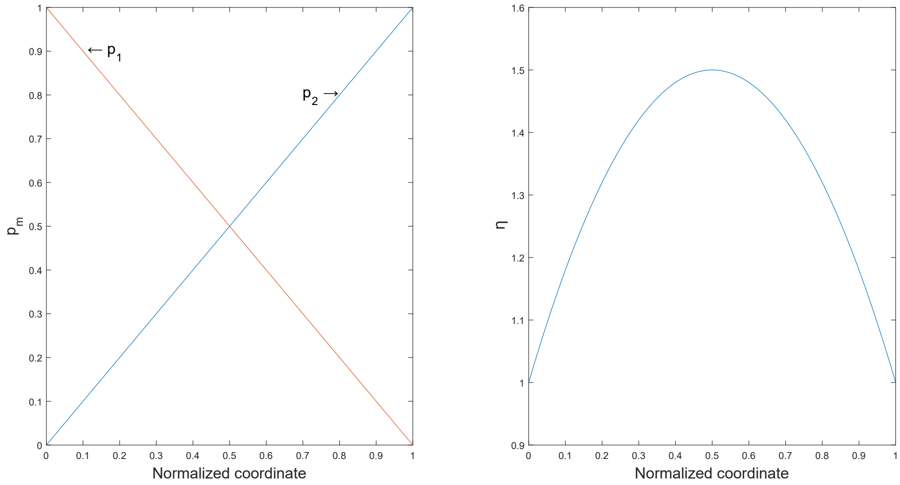

Figure 5.8: Mode hop model. In the left panel, the power transfer from the mode at ω_1 to the one at ω_2 is shown. In the chosen set of coordinates, $p_1(x) = 1 - x$ and $p_2(x) = x$. In the right panel, the enhanced second harmonic efficiency (see eq(5.3.10)) is computed as function of x.

Now we can compute the ratio η of the multimode second harmonic generation over the single mode second harmonic generation. We suppose that mode phases are uncorrelated and randomly distributed over the range $[0, 2\pi]$.

$$\eta = \frac{P_{mm,sh}}{P_{sm,sh}} = 1 + \sum_{\substack{m=1\\ m\neq m'}}^{N} \sum_{m'=1}^{N} |\alpha_m|^2 |\alpha_{m'}|^2 \tag{5.3.9}$$

In our case

$$\eta = 1 + 2|\alpha_1|^2|\alpha_2|^2 \tag{5.3.10}$$

In the special case of $|\alpha_1|^2 = |\alpha_2|^2 = 1/2$, we have from eq(5.3.10) that $\eta = 1.5$.

Now, let's imagine a case where the source starts lasing single mode at ω_1 and ends lasing a single mode at ω_2. Let's define a normalized coordinate x so that the process of power transfer from the mode at ω_1 to the one at ω_2 starts at $x = 0$ with $p_1(0) = 1$ and ends at $x = 1$ with $p_2(1) = 1$. The power transfer must obey the condition $p_1(x) + p_2(x) = 1\ \forall x$; we suppose that process like in the left panel of Fig.5.8. For the model described above, eq(5.3.10) has been computed and it is shown on the right panel of Fig.5.8. In such a coordinate system, eq(5.3.10) becomes $\eta = 1 + 2x - 2x^2$.

Using the setup described in the previous chapter, we measured the SHG green production at fixed input power, fixed PPKTP crystal temperature and varying the laser NPRO crystal temperature: acting on it, the frequency of the laser is changed by approximately 3 GHz/K (see Fig.5.9).

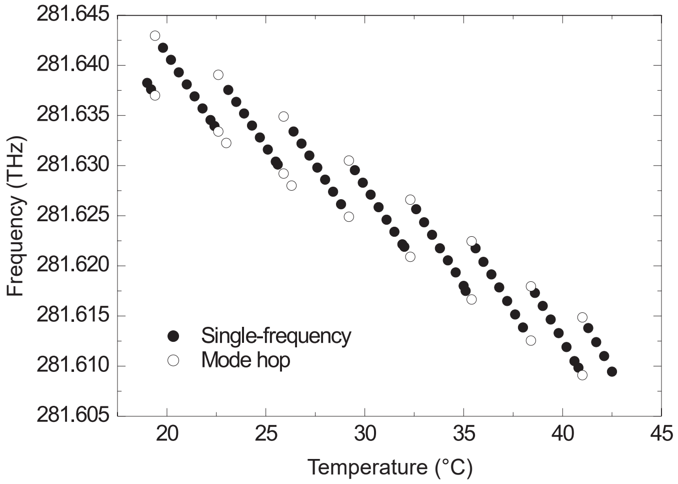

Figure 5.9: Standard Mephisto slow control. Taken from 'Coherent, Mephisto/Mephisto S' datasheet.

As shown by Fig.5.9, in some ranges of temperatures, the laser is not single mode but two different modes coexist. This process is commonly known as *mode hop.* Fig.5.10 (left) shows the produced green as function of the NPRO crystal temperature. These measurements show four temperature ranges where the second harmonic generation is enhanced. The spacing between them is compatible with the temperature difference between two laser mode hops and the second harmonic production enhancement η (see eq(5.3.10)) is compatible with the developed model of two different modes with a linear power transfer between each other.

I have also performed measurements of the produced green as function of the laser crystal temperature for different laser diode current, that means, for different IR input power into the

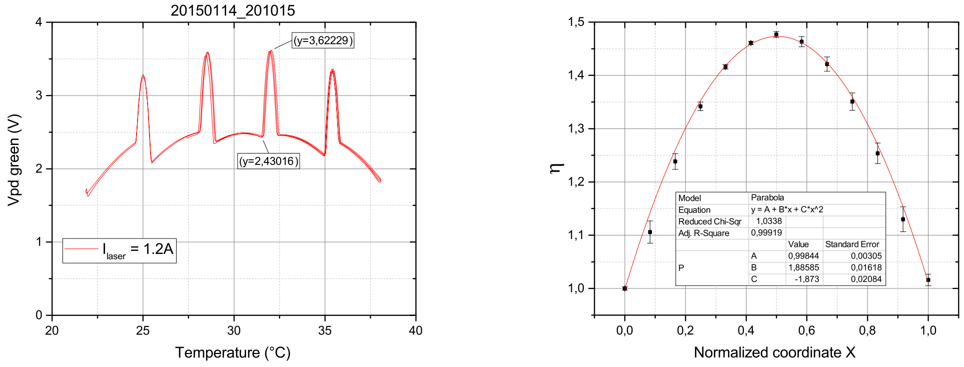

Figure 5.10: SHG green production at fixed PPKTP crystal temperature (304.4 K) and at fixed input power. In the left panel, the produced green as function of the laser NPRO crystal temperature. Four temperature ranges of enhanced green production are clearly visible. On the right panel, a zoom of one of the enhanced green production areas. To compare the data with the model, the ratio of the multimode second harmonic generation over single mode second harmonic generation has been computed and the NPRO temperature is converted in the x coordinate using $x = (T_{NPRO} - T_0)/\Delta T$ where T_{NPRO} is the temperature of the laser crystal, T_0 is the mode hop starting temperature, in the case of the measurement present in the right panel $T_0 = 31.6°C$; ΔT is the temperature width of the mode hop process ($\Delta T = 0.9°C$). The data are fitted according to eq.(5.3.10) with $\eta = a + bx + cx^2$ resulting in $a = 0.998 \pm 0.003$, $b = 1.89 \pm 0.02$ and $c = -1.87 \pm 0.02$.

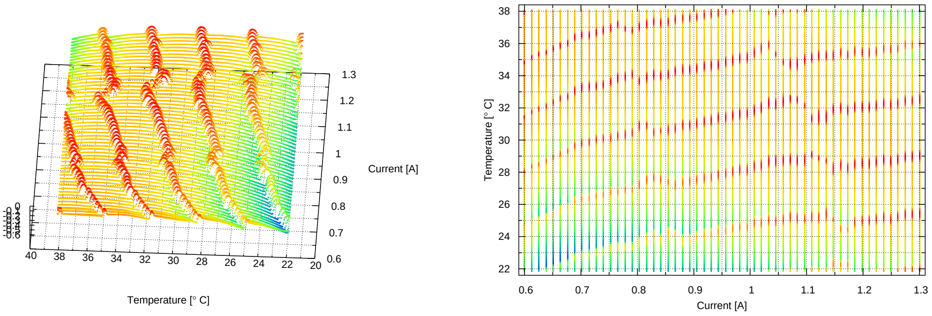

Figure 5.11: 3D and 2D maps of the green production as function of laser diode current (I) and NPRO crystal temperature (T). The enhanced green production due to the coexistence of 2 laser mode (during the mode hop) has been mapped.

double pass SHG. Results are presented in Fig.5.11. Each measurement at fixed diode current, has its own color map, this has been done for visual purpose. The right panel of Fig.5.11 shows the laser mode hop map. In Fig.5.7, for three different IR pump power ranges, an enhanced green production is present. For each of this three "bumps", the best green enhancement is approximately a factor of 1.5. By looking Fig.5.11 for any NPRO crystal temperature, the mode hop lines are crossed at least once while scanning the laser diode pump current, thus, we can conclude that the three "bumps" present in Fig.5.7 are due to the presence of the laser mode hops.

5.4 In cavity SHG

In this section, the in cavity SHG is described and characterized. Fig.5.12 (right) shows a picture of the SHG cavity.

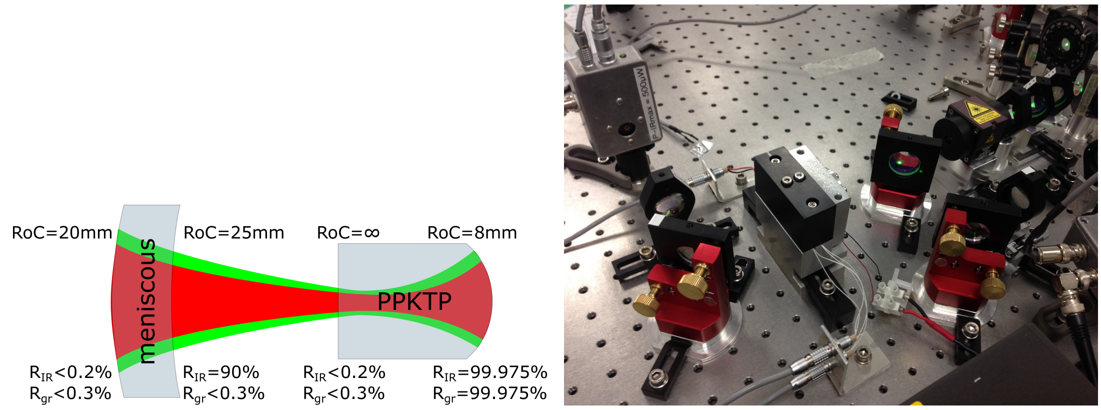

Figure 5.12: (left) SHG cavity scheme. All the power reflectivities and the curvature radii are listed. (right) Picture of the working SHG cavity.

The cavity is constituted by the PPKTP crystal and an in-coupling mirror. The non linear crystal has dimension 1 mm × 1.5 mm × 9.3 mm; the back surface of the crystal has a radius of curvature of 8mm and is high reflection coated ($R = 99.975$ % for both green and IR wavelength) whereas the other surface of the crystal is flat and it is anti-reflection coated ($R < 0.2$ % for IR wavelength and $R < 0.3$ % for green wavelength). The other part of the cavity is a partially reflective meniscus lens with the inner surface reflectivities of $R = 90$ % at 1064 nm, $R < 2$ % at 532 nm and a radius of curvature of 25 mm. This results in a finesse of the cavity at the fundamental wavelength of $\mathcal{F} = 54$, a free spectral range (FSR) of approximately 3.8 GHz and a full width half maximum (FWHM) of approximately 71 MHz. The outer surface of the meniscus is anti-reflection coated for both wavelengths and has a radius of curvature of 20 mm. The meniscous is mounted on a piezoelectric actuator (see Fig.5.2). The power reflectivities for all the surfaces and the radii of curvatures are summarized in Fig.5.12. The optical simulation are performed in detail in A.1.

The SHG cavity length has been locked to the IR laser source by a standard PDH technique. The incoming field at 1064 nm is phase modulated at 80 MHz using a commercial electro-optic modulator (EOM). The reflected light is detected and analogically demodulated at 80 MHz. The demodulated signal is acquired and processed by a commercial PXI system and the processed signal is then fed back to the piezoelectric ceramic that moves the incoupling mirror of the SHG cavity. The measured open-loop transfer function of the SHG cavity length control loop is plotted in Fig.5.14. The unitary gain frequency is approximately equal to 600 Hz. The transfer function of all the loop but the PXI controller is plotted in Fig.5.15.

For the second version of the control electronics the RF photodiode has been replaced with a new version (detail in appendix) and the PXI system by the SAT board. Fig.5.16 shows a

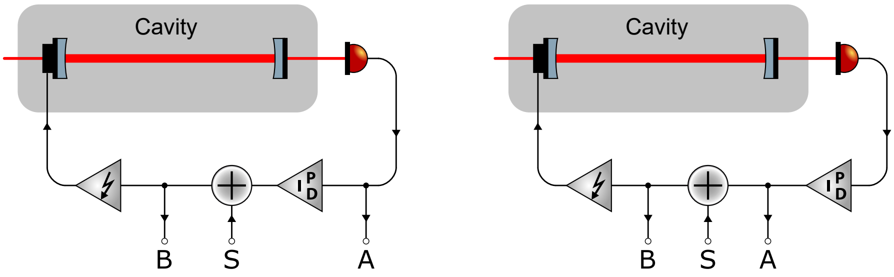

Figure 5.13: Schematic of measuring the transfer function of a cavity (left) and the open loop transfer function of the same cavity with the servo (right). The cavity TF is the ratio between the PSDs measured at node A over the one measured at node B, while injecting noise at the node S. The open loop transfer function is minus the ratio between the PSDs measured at node A over the one measured at node B, while injecting noise at the node S. The noise injected must be the dominant signal source of the loop, otherwise the measure is meaningless.

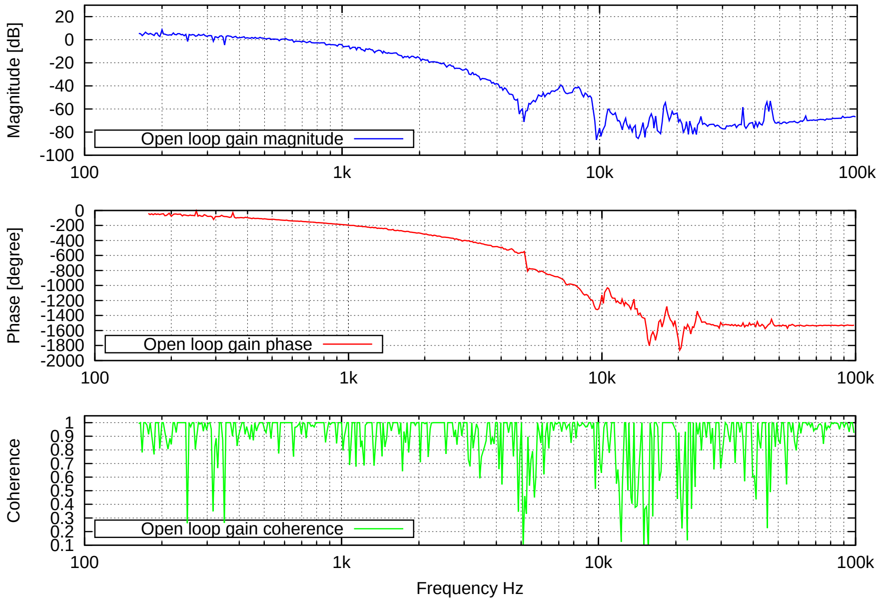

Figure 5.14: Measurement of the open-loop transfer function of the SHG cavity with the first version of control electronics. The unitary gain frequency is approximately equal to 600 Hz.

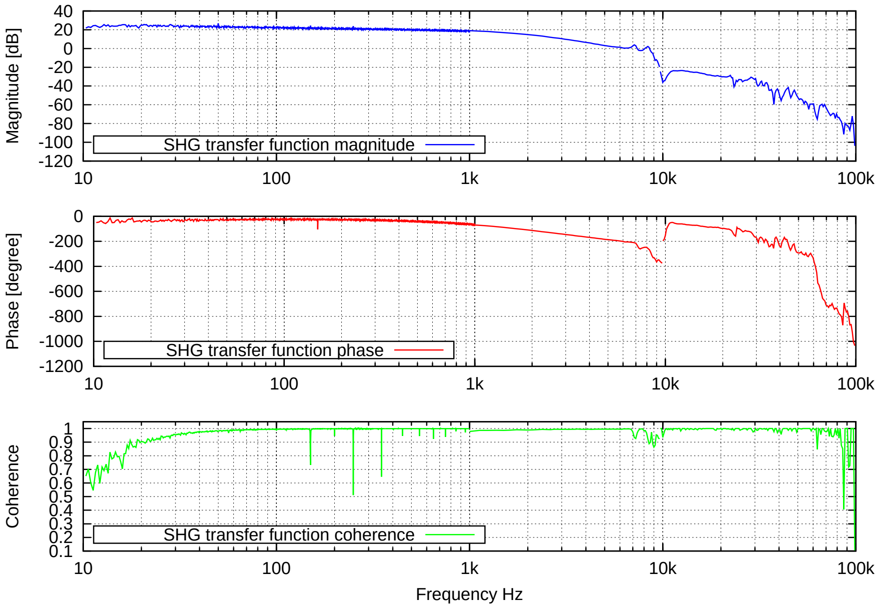

Figure 5.15: Measurement of the transfer function of all the loop but the PXI controller with the first version of photodetector and demodulator.

comparison between the dark noises of the old RF photodetector plus the demodulation stage compared with the dark noise of the new version RF photodetector with the embedded demodulation: the noise of the new photodetector is at least one order of magnitude (up to more than two order of magnitude) better than its older version.

5.4.1 Alignment and mode matching

The SHG cavity must be aligned so that the optical axis inside of the mirror and the crystal matches. To properly align the SHG cavity I found this procedure particularly appropriated. The procedure consists in few steps.

1. Prepare a beam with the beam waist needed to couple the SHG cavity entering from the back side of the PPKTP crystal and mark two positions of the beam with two iris along the path.

2. Insert between the two iris the PPKTP entering from its curved side with the crystal housed inside its mounting and placed over a multi-axis micrometric stage, move the crystal so that the beam direction is not changed by the presence of the crystal and, at the same time, the reflected ray from the curved side of the crystal must overlap with the incoming beam.

3. Place the meniscus mirror in place and move it on a plane perpendicular to the beam path while scanning with the piezo the cavity length. Adjust the position of the meniscus to have proper cavity modes in transmission and keep adjusting it until all the high order mode are suppressed.

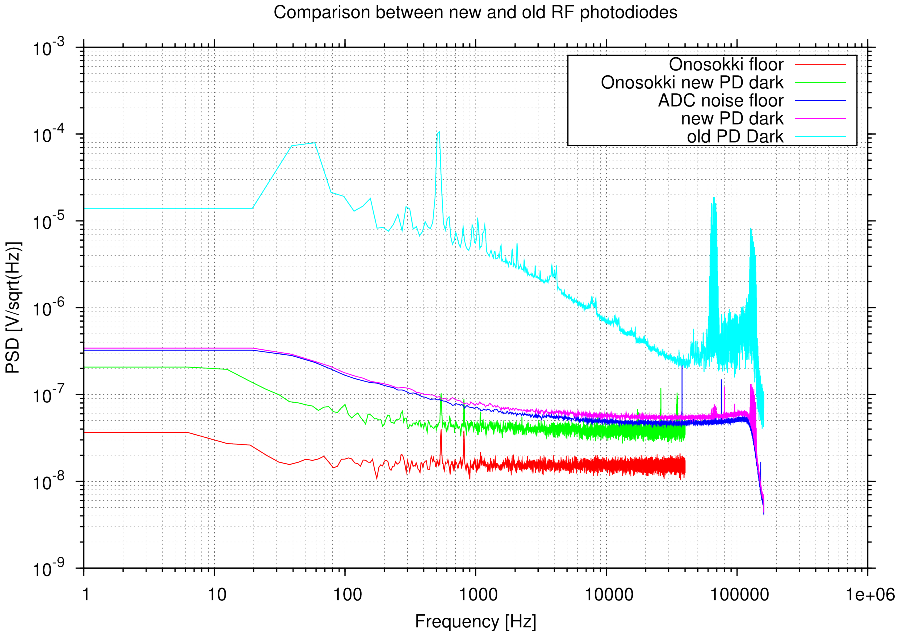

Figure 5.16: Dark noise of the old RF photodiode and demodulation stage compared with the dark noise of the new RF photodiode with embedded demodulation stage.

After these steps, the cavity is almost aligned; it can then be turned around and placed in the correct position. The residual high order modes that are present while adjusting the incoupling mirror (step 3), can now be further suppressed acting on the two steering mirror in front of the cavity.

All these actions must be performed at a crystal temperature where the infrared to green conversion is low. This is because the conversion from IR to green can be seen as a loss in the IR field, therefore, the impedance matching of the cavity changes as function of the conversion efficiency. For the case of negligible second harmonic conversion efficiency, the usual reflection function can be defined as follow

$$F = \frac{E_{refl}}{E_{inc}} = \frac{-r_1 + r_2(r_1^2 + t_1^2)e^{\imath\omega/\omega_{FSR}}}{1 - r_1 r_2 e^{\imath\omega/\omega_{FSR}}} \tag{5.4.1}$$

For negligible second harmonic conversion, the SHG cavity is strongly overcoupled, see Fig.5.17. In this situation, if we suppose the input IR beam to be a perfect TEM_{00}, the cavity mode matching can be measured in the following way: the cavity length is varied by few FSRs and the transmitted light is recorded, the mode matching is computed as the ratio between the area of a TEM_{00} over the total area of a FSR. Fig.5.18 shows the best mode matching obtained: ≈ 98 %.

5.4.2 High efficiency SHG

To increase the efficiency of a nonlinear conversion, the nonlinear crystal is usually inserted inside an optical resonator. As in [44], we define the conversion efficiency

$$\epsilon = \frac{P_2}{P_1} \tag{5.4.2}$$

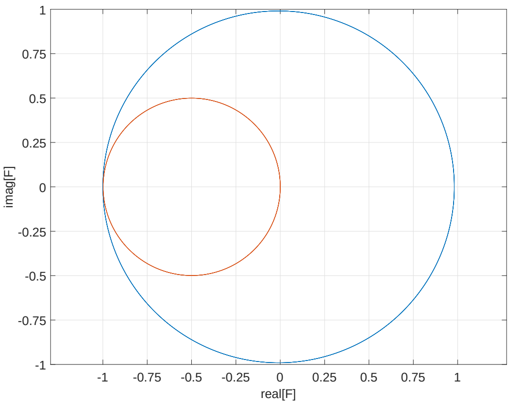

Figure 5.17: Plot of the F function for the SHG in the imaginary plane in blue. As reference, a perfectly impedence matched cavity with no losses in orange.

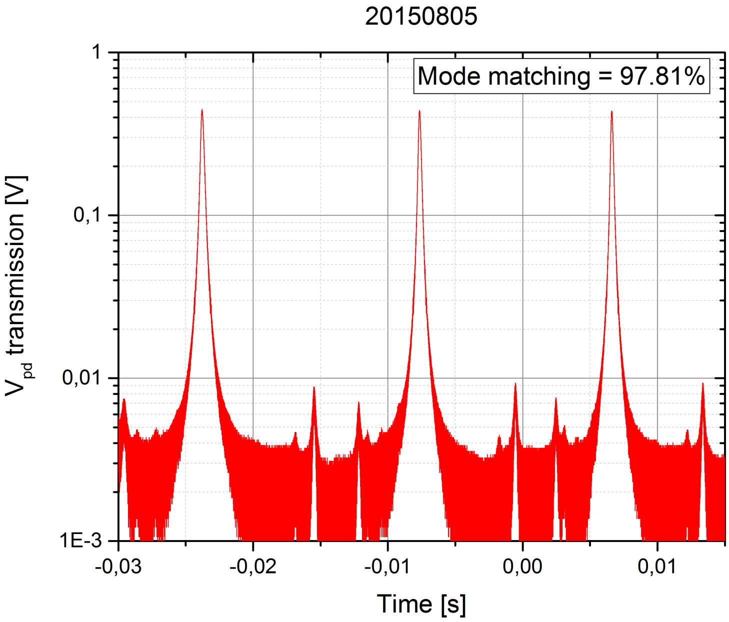

Figure 5.18: SHG mode matching. A mode matching of ≈ 98 % has been achieved. Most of the mismatch is due to TEM_{01} and TEM_{02}.

with P_1 the fundamental input power and P_2 the harmonic output power. Using this definition, a simple calculation from [49] yelds

$$\sqrt{\epsilon} = \frac{4T_1\sqrt{E_{NL}P_1}}{\left[2-\sqrt{1-T_1}\left(2-\sigma-\sqrt{\epsilon E_{NL}P_1}\right)\right]^2} \tag{5.4.3}$$

where E_{NL} is the single-pass nonlinear conversion efficiency (eq.(5.3.1)), T_1 is the transmission coefficient of the input coupler and σ describes all the linear losses in the cavity exclusive of T_1 (σ and T_1 both refer to the fundamental field). As in the case of the single- and double-pass second harmonic conversion, also for the in-cavity conversion, the quasi-phase matching condition must be fulfilled to obtain the optimal conversion efficiency. The temperature of the PPKTP crystal is thus an important parameter to be optimized and stabilized.

In the setup developed for this work, the temperature stabilization is performed using a standard PID loop implemented into the PXI system. The temperature loop uses a NTC thermistor as temperature sensor of the crystal temperature and a Peltier cell as heater. Another thermistor is used as out of loop monitor of the crystal temperature. Other two thermistors are also acquired to monitor the optical bench and the room temperatures. The data acquired over a weekend with the temperature control ON and the locked SHG are shown in Fig.5.19. In the first two top strip charts which show the environmental temperatures (room and bench), the day-night alternation is clearly visible. The third strip represents the in loop temperature: the FWHM of the histogram is 1.1 mK. The bottom strip is the out of loop temperature monitor; also this trace evidences the day-night alternation, but the fluctuation is suppressed by a factor of 30, compared to the bench temperature.

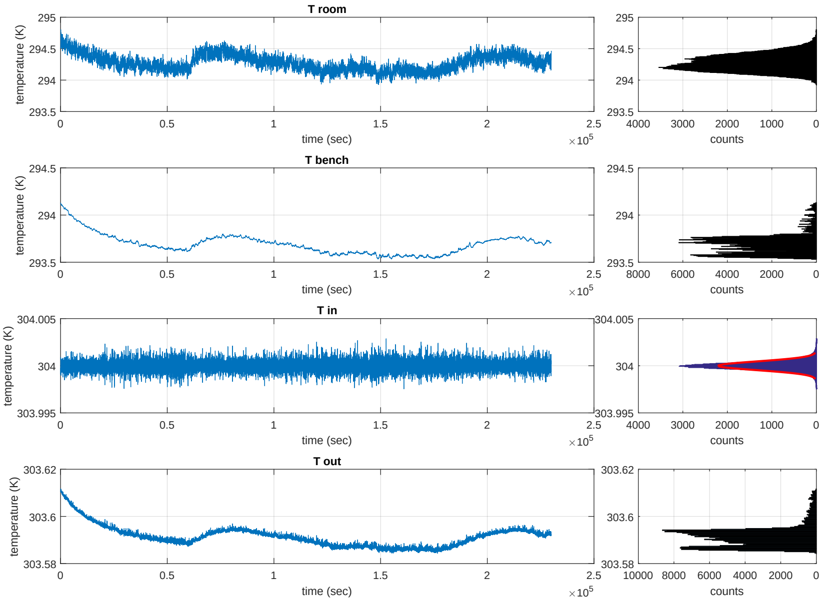

Figure 5.19: Temperature variation over time when temperature control i ON.

With the stabilized temperature, the green production has been measured for several input power P_1 and for several crystal temperatures, so to map the green production and therefore the in cavity conversion efficiency. A scheme of the measurement is in Fig.5.20.

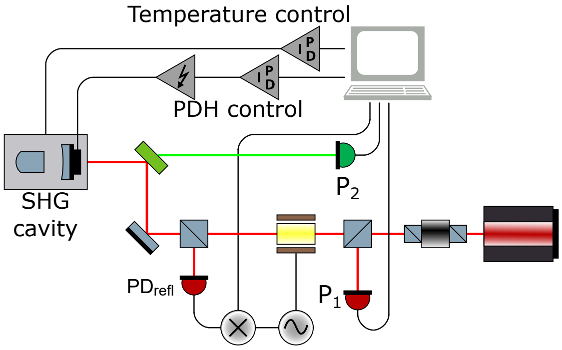

Figure 5.20: In cavity measurement scheme.

Fig.5.24 shows the results of a typical measurements at fixed input power: they are fully automated using the digital controls. The PPKTP crystal temperature is fixed and, after readying the steady state the input power and the produced green are measured. This procedure is repeated at different crystal temperatures, between 298 K and 314 K.

Another set of measurements were taken: the crystal temperature is fixed and the IR input power is manually changed between 30 mW to 0.5 W, and for each IR input power, the produced green is recorded. The data collected for $T = 304.6$ K are presented in Fig.5.22. In this figure also the numerical solution of eq.(5.4.3) is shown (red line). The parameter used to obtain this solution are $E_{NL} = 0.028\ \mathrm{W}^{-1}$ and $\sigma = 0.005$. The value of E_{NL} found is comparable to the one found in section 5.3 with another kind of measurement. In the figure are clearly visible four data point that differ quite a lot from the computed curve (marked as star). Those data show that there exists a process that limits the maximum green produced power. This process will be exploited in the next section.

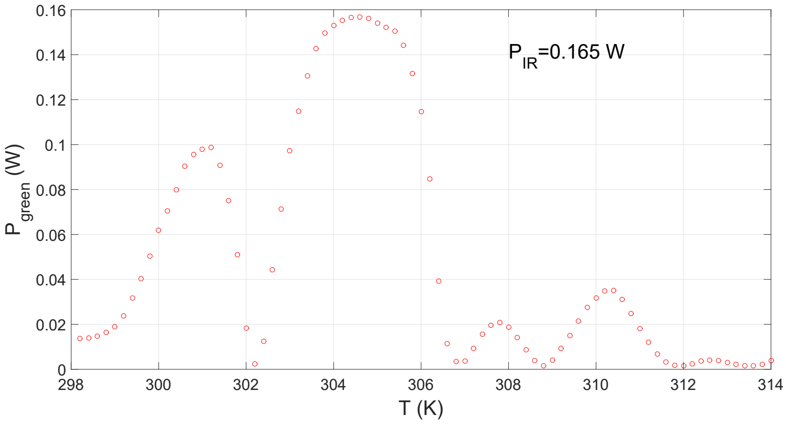

Figure 5.21: In cavity produced green at fixed input IR power for different temperature of the crystal.

The same measurement presented in Fig.5.22 has been done for different temperatures between 300 K and 310 K and for each set of data, eq.(5.4.3) has been solved with different E_{NL} (σ is considered constant over this temperature range). Fig.5.23 shows the results of these computation: E_{NL} changes as function of the crystal temperature, as expected. This is due to the

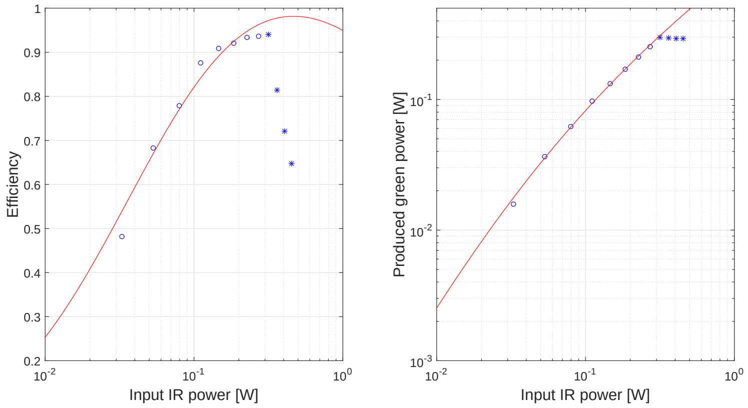

Figure 5.22: In cavity produced green at fixed crystal temperature ($T = 304.6$ K) for different IR input power. The red line on the left panel is the numerical solution of eq.(5.4.3), while the right panel red line is the one of the left panel multiplied by the input IR power. The parameter used to compute the solution are: $E_{NL} = 0.028$ W^{-1} and $\sigma = 0.005$.

quasi phase matching condition.

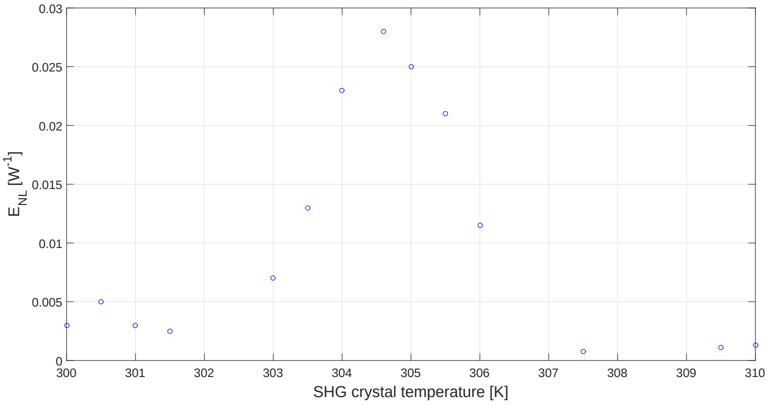

Figure 5.23: E_{NL} as function of the PPKTP crystal temperature.

Fig.5.24 summarizes the measurements collected and presented in Fig.5.21 and in Fig.5.22. As clear from the right panel of this figure, there is a set of parameter (P_1 and T) for which the conversion efficiency is extremely high. The maximum conversion efficiency found is at a crystal temperature $T = 304.6$ K, with an input power $P_1 = 0.165$ W that produces $P_2 = 0.1568$ W of green power with a conversion efficiency of $\epsilon = 0.95$. The result obtained is not corrected for the green reflectivity of the first dichroic beam splitter that is used to extract the green beam from the IR light path; the amount of IR power at the sideband frequencies has also been negleced. Both effects would point to even higher efficiencies. As far as I know, this is the highest Second Harmonic Generation efficiency present in the literature.

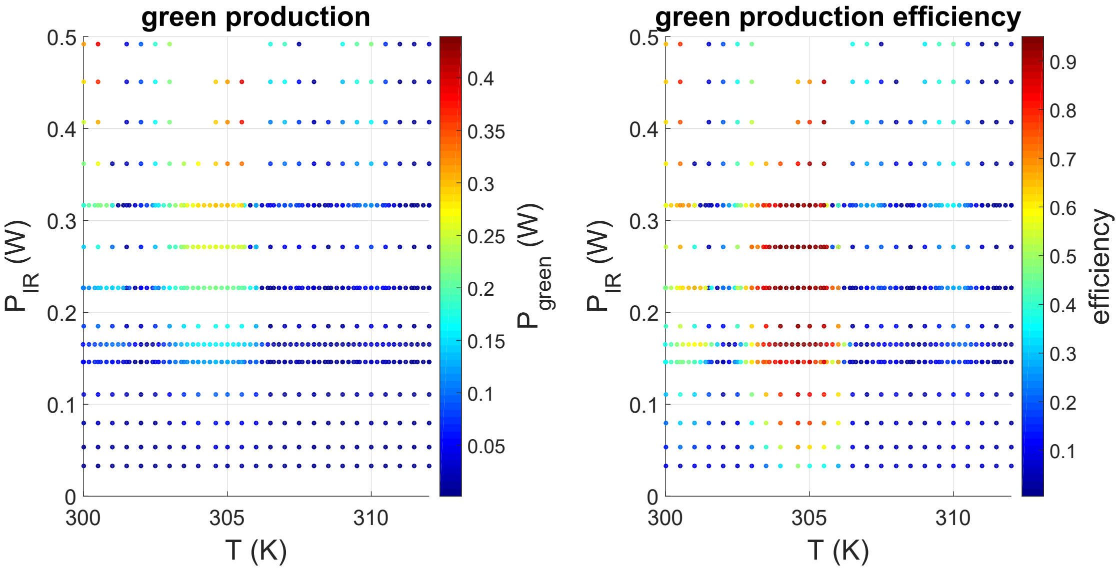

Figure 5.24: In cavity green production and efficiency results.

5.4.3 Competitive non linear processes

The star points of Fig.5.22 shows that it exist a process that limits the maximum amount of green that can be produced by our SHG cavity. This process is the parametric down conversion of light. The parametric up and down conversion processes are well known and studied and they are the basis of the operations of the OPOs and OPAs. A crucial parameter for these processes is the threshold pump power. This threshold parameter depends on the crystal optical and geometrical parameter and also on the cavity optical parameters. For the case of a degenerate doubly resonant[3] OPO with optimized confocal near-field Gaussian beams and for optimized phase matching ($\Delta k = 0$), the pump threshold $P_{p,th}$ is [50]:

$$P_{p,th} = \frac{\epsilon_0 n_s^2 c \lambda_p^3}{2\pi^2 d_{eff}^2 L_{cr}} \ln^2(R) \tag{5.4.4}$$

where n_s is the refractive index for the signal (IR beam in our case), λ_p is the wavelength of the pump (532 nm), d_{eff} is the effective non linear coefficient, L_{cr} is the non linear crystal length and $R = \sqrt{R_1 R_2}$ is the terms that takes into account the reflectivities of the two cavity mirrors.

When an OPO cavity is operated below threshold, the signal suffers an amplification or a deamplification depending on the relative phase between the pump and the signal field; when is operated above threshold, the pump field is converted to the signal field with an high gain coefficient.

Also for a SHG cavity the threshold parameter can be defined, and in this case the pump field is the produced green itself. Therefore, if the amount of produced green exceed the pump threshold of the system, the green is down converted to IR before exiting the cavity.

This effect can be seen when operating the SHG in a steady state (i.e. nonlinear crystal temperature stabilized and cavity length locked) or while scanning the cavity length. An example

---

[3] Degenerate in the sense that the signal and the idler are at the same frequency, and doubly resonant means that both the signal and the idler are resonant at the same time, that is straightforward in the case of degenerate OPO.

of this last measurement is in Fig.5.25. Here each couple of green and red peaks represents a cavity length scan of the TEM_{00} for different IR input power. When below threshold the produced green amplitude increases as function of the IR power and both the produced green peak and the transmitted IR light (red curve) peak are Airy functions, as expected. When above threshold, the top of the green peak exhibit a jagged profile. This profile is due to the fact that, as steated in [51], the threshold also depends on the cavity detuning.

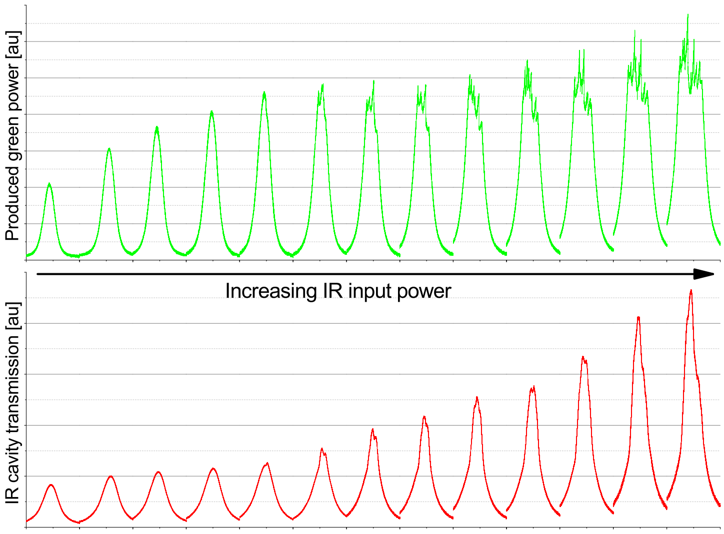

Figure 5.25: Produced green and transmitted IR TEM_{00} scans for different IR input power. When the produced green power exceeds the threshold of the system, the Airy function gets clipped and exhibit a jagged profile. The clipped value is the system threshold. The jagged profile is due to the fact that the threshold also depends on the cavity detuning. The IR input power ranges from 25 mW to 120 mW.

I measured the SHG threshold as function of the nonlinear crystal temperature for two different SHG cavities. The two SHG cavities differ only for the IR power reflectivity of the incoupling mirror, that is $R_{IR} = 0.96$ in the first case and $R_{IR} = 0.90$ in the second case. The threshold measurement reported in Fig.5.26 refers to the cavity with $R_{IR} = 0.96$ and was obtained with the cavity scanning technique. As it is clear from the plot, the maximum green power achievable with this cavity is 70 mW at a nonlinear crystal temperature of 310 K. On the other hand, the non linear gain E_{NL} is maximum at about 305 K as shown in Fig.5.23. Thus, this indicates that the maximum produced green power is not at the maximum nonlinear gain because there the threshold is relatively low. The maxium produced green power is for this SHG cavity is thus set as a compromise between the nonlinear gain and the threshold. In Fig.5.26, three different phase matching curves are also shown. It is clear that for the highest input power case (black curve), the pump threshold limits the green production in most of the crystal temperature range and in particular around 305 K.

Fig.5.27 shows the results for the SHG with low IR incoupling mirror reflectivity ($R_{IR} = 0.90$). As clear from eq(5.4.4), the threshold increases if the mirror reflectivity gets lower. In fact, for 305 K for example, the threshold changes from $\approx$ 20 mW for $R_{IR} = 0.96$ to $\approx$ 300 mW for

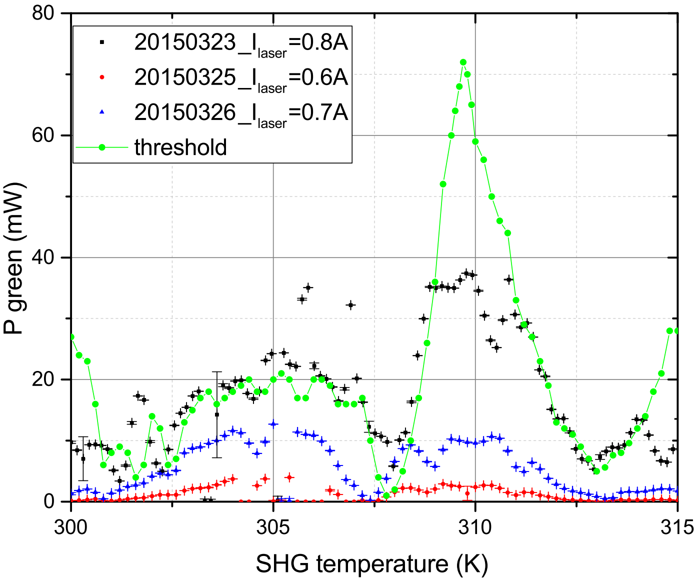

Figure 5.26: Phase matching curves and green pump threshold measured for a SHG with $R_{IR} = 0.96$ for the incoupling mirror. The input IR power for the three phase matching curve is respectively 45 mW for the black, 25 mW for the blue and 5 mW for the red curve.

$R_{IR} = 0.90$. In that figure the red star points represent the threshold measured with the cavity length scanning technique, while the blue dots are obtained with the measurement presented in Fig.5.22.

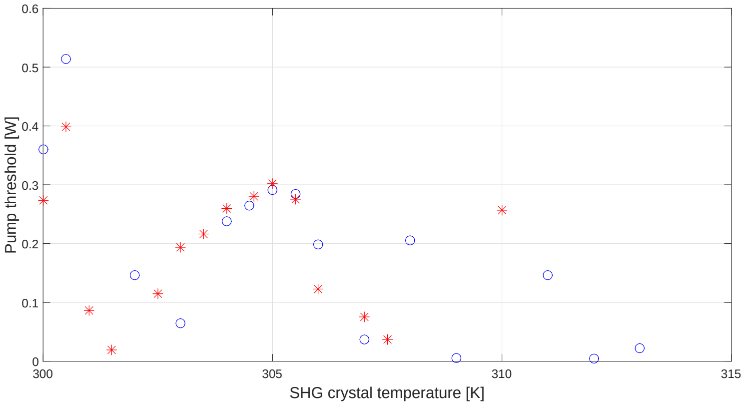

Figure 5.27: Green pump threshold measured for a SHG with $R_{IR} = 0.90$ for the incoupling mirror. Red star points are collected using the cavithy length scan technique, while, blue dots are obtained with the measurement presented in Fig.5.22.

From these measurements, it is evident that, if one wants to maximize the produced green power at low IR input power, the choice of the incoupling mirror reflectivity needs to be a tradeoff between conversion efficiency (see eq(5.4.3)) and threshold (see eq(5.4.4)). In our case, the choice of $R_{IR} = 0.90$ is good to produce 200 mW green power with ≈ 220 mW IR input power.

5.4.4 Birefringence and absorption losses

In this section I present a birefringence measurement on the SHG cavity and I propose a methodology to measure intracavity losses based on birefringence.

Birefringence measurements are crucial measurements in the case of the OPO cavity since we plan to lock the cavity length with p polarized light, therefore the frequency offset between the p pol and s pol resonance condition must be known exactly to proper set up the LO of the PLL between the main laser and the AUX2 laser. Since the nonlinear material is the same for both the OPO and the SHG cavity, we expect that, apart from a frequency offset, the slope of the effect should be the same. This phenomenon arises from the fact that for some material, the refractive index for ordinary and extraordinary rays is different.

Fig.5.28 shows the measurement of the frequency offset between p pol cavity resonance and s pol cavity resonance as function of the PPKTP crystal temperature. This measurement shows that the frequency offset between the two polarization resonances depends linearly on the temperature. The red line represents the linear fit of the data, the slope estimates the birefringence coefficient ((502 ± 2) MHz/K), while the intercept depends on the initial measurement setup and we are not interested in it.

The measurement has been performed at low IR input power to reduce self heating effects of the crystal and while scanning the cavity length feeding the piezoelectric actuator with a triangular signal. The calibration of the temporal axis is ensured by the sidebands imposed by the EOM.

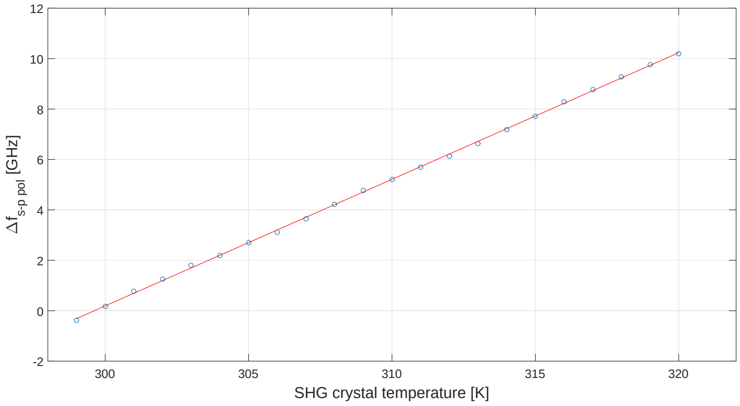

Figure 5.28: Measurement of the frequency offset between p pol cavity resonance and s pol cavity resonance. The results of the linear fit (red line) is a slope of (502 ± 2) MHz/K.

The proposed measurement is based on two assumption: the temperature gradient inside the crystal is defined uniquely by the spatial profile of the laser beam and the temperature we set with the control loops does not affect the spatial shape of this thermal gradient but just add an offset to the temperature profile inside the crystal. This two assumption have been tested and confirmed by finite element simulations of the system.

We lock the cavity as always on the s pol beam, but we inject a small portion of p pol light. Once the cavity is locked at low IR input power, a temperature for which the two polarization are both perfectly on resonance must be found. At this point, due to material absorption, an increase of IR input power, leads to a local heating of the crystal along the optical path. Due to this temperature change, the two polarization won't be both on resonance. In particular, since the length lock is performed on s pol, the p polarized light won't resonate perfectly. The convolution product between the Airy function of the cavity and the p pol laser line, allow us to know the frequency difference between the two polarization caused by the temperature change. Using Fig.5.28 the frequency offset can be translated into a local temperature change. From preliminary computation, the expected temperature sensitivity is ≈ 1.5 mK.

For simple systems, the heat transfer equation $\dot{Q} = kA\nabla T$ allow us to compute the total absorption coefficient α since $\dot{Q} = P_{in}\alpha$. In our case, we will use finite element simulation to solve the heat transfer equation in our system.

Chapter 6

Faraday Isolator

The injection losses are the main limiting factor which will limit the benefits of injecting a vacuum squeezed state into a GW interferometer. The experience of the LIGO and GEO groups indicates that one of the main contributors to the injection optical losses is the in vacuum Faraday isolator (FI) where the squeezed light field is injected into the interferometer at the detection bench. The FI installed in GEOO600 was characterized in air and showed transmission losses equal to $\approx 2\%$ [42]; however, once in vacuum, the inferred total losses due to the FI is $\approx 7\%$ (I remind that this FI is crossed twice by the squeezed vacuum field). In my opinion, the increase of transmission losses is mainly due to a variation in the temperature of the paramagnetic crystal used in the Faraday isolator, due to the absence of convective heat transfer. This variation leads to a difference in the angular rotation of the polarization plane after the paramagnetic crystal, with respect to the designed angular rotation which is tuned in air (ideally $45°$).

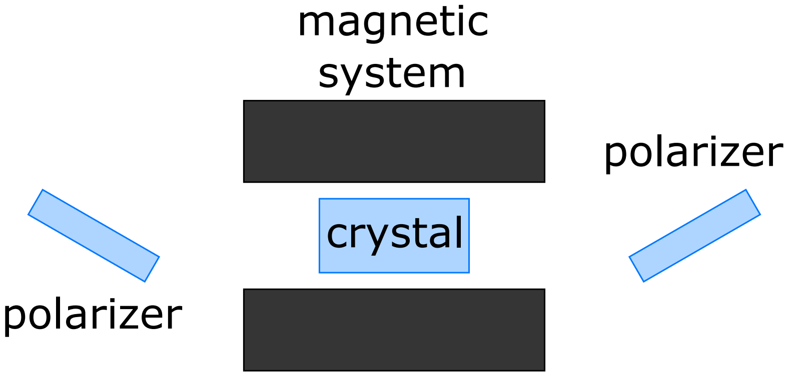

Figure 6.1: A Faraday isolator is constituted by two crossed polarizer and a paramagnetic crystal imbued into a magnetic field in the direction of the light propagation.

In this chapter I present the study and characterization of a low loss, high isolation, temperature tunable, vacuum compatible Faraday isolator. The measurements include the optical characterization of the main components of the FI (polarizers and TGG paramagnetic crystal), the study of the variation of the paramagnetic properties of the TGG crystal with temperature. This study is performed to characterize an AdV high power FI. I furthermore designed a new prototype of FI, improving in particular the thermal isolation of the TGG crystal with respect to the other components of the system (in particular from the magnets of the FI). This new design is suitable not only for the high power utilization in AdV, but it fits also the requirements for the squeezed vacuum injection.

The Faraday Isolator (FI) is a magneto-optical component widely used in optical setups to protect the laser system from the light which is back-reflected and back-scattered by an optical system. A FI is traditionally composed by two polarizers and a Faraday Rotator (FR), which is composed by a paramagnetic crystal immersed in a magnetic field (Fig.6.1).

The basic principle of a FR is the Faraday effect. Let us consider a linearly polarized beam that crosses a paramagnetic transparent medium placed in a homogeneous magnetic field parallel to the beam propagation direction; the beam polarization axis is rotated by an angle θ with respect to the input polarization:

$$\theta_{FR} = \mathcal{V} B n d \tag{6.0.1}$$

where d is the length of the paramagnetic crystal where the light and the magnetic field interact, n is the refractive index of the paramagnetic crystal, B is the magnetic field in the direction of the light propagation and $\mathcal{V}$ is the Verdet constant of the paramagnetic material (see Fig.6.2). The Verdet constant is defined empirically and varies with the crystal temperature and with the light's wavelength. For the terbium gallium garnet (TGG) the Verdet constant ranges from $\mathcal{V} = -134$ rad/Tm at room temperature and for a wavelength of 632 nm to $\mathcal{V} = -40$ rad/Tm at room temperature and for 1064 nm light.

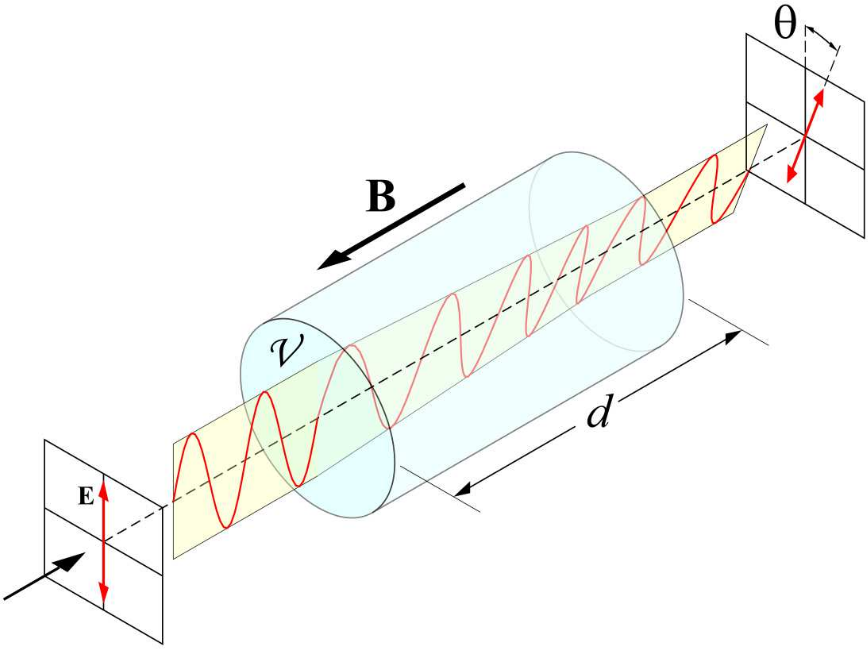

Figure 6.2: Scheme of the Faraday effect. E is the oscillating electric field, d is the geometrical length of the paramagnetic crystal, B is the magnetic field and θ is the angle rotation as in eq(6.0.1).

The performance of a FI are determined by the isolation ratio and the throughput or transmission losses (Σ_{tr}). The Σ_{tr} are defined by eq(6.0.2) where the first term represents the angular mismatch between the FR and the input polarizer ($\mathrm{d}\theta_{FR}/\,\mathrm{d}T$ is the derivate of the angular rotation due to the Faraday effect with respect to the temperature, ΔT is the temperature variation of the FR and $\theta_{FR} - \theta_p$ is the static or initial angular mismatch between the FR angular rotation and the output polarizer angle with respect to the input polarization angle) and the second and the third ones are the sum of all the losses due to non-perfect AR coating and material absorption (R_{AR} is the power reflectivity of a generic AR coated surface, while α is the material absorption coefficient per unit length).

$$\Sigma_{tr}(T) = \left(1 - \cos^2\left(\Delta T \frac{\mathrm{d}\theta_{FR}}{\mathrm{d}T} + \theta_{FR} - \theta_p\right)\right) + \sum_i R_{AR,i} + \sum_j \mathrm{e}^{\alpha_j \ell_j} \tag{6.0.2}$$

The isolation ratio is defined by eq(6.0.3) where the first term takes into account the angular mismatch between the FR and the polarizer, the second the polarizer quality and the third represents the thermal depolarization where $\gamma = \gamma(\delta T(r))$, $\delta T(r)$ is the temperature profile inside the TGG crystal, r is the radial distance from the optical axis of the TGG (our system has been considered having cylindrical symmetry) and P_{in} is the input power.

$$isolation(T, P_{in}) = -10 \cdot \log_{10}\left(\cos^2\left(\Delta T \frac{\mathrm{d}\theta_{FR}}{\mathrm{d}T} + \theta_{FR} + \theta_p\right) + p_q + \gamma P_{in}^2\right) \tag{6.0.3}$$

Fig.6.3 shows the analytical computation of (6.0.2) and (6.0.3). For this computation, the losses due to AR coatings and material absorption are not considered; the thermal depolarization is not considered as well. The computation is performed at fixed temperature.

In both isolation ratio and Σ_{tr} equations, the temperature dependence of the angular mismatch between polarizer and FR is mainly due to the thermal dependence of the Verdet constant of the crystal inside the FR. In particular from eq(6.0.1) we have

$$\frac{\mathrm{d}\theta_{FR}}{\mathrm{d}T} = \frac{\partial B}{\partial T}\mathcal{V}nd + \frac{\partial \mathcal{V}}{\partial T}Bnd + \frac{\partial n}{\partial T}\mathcal{V}Bd + \alpha_{th}\mathcal{V}Bnd \tag{6.0.4}$$

$$= \theta_{FR}\left(\frac{\partial B}{\partial T}\frac{1}{B} + \frac{\partial \mathcal{V}}{\partial T}\frac{1}{\mathcal{V}} + \frac{\partial n}{\partial T}\frac{1}{n} + \alpha_{th}\right) \tag{6.0.5}$$

in the last term of eq(6.0.5), α_{th} is the linear thermal expansion coefficient of the paramagnetic crystal.

A common material used in FR as paramagnetic crystal is the Terbium Gallium Garnet (TGG, $Tb_3Ga_5O_{12}$). For TGG at room temperature, the thermal expansion coefficient is of the order of $\alpha_{th} \approx 10^{-6}$ K^{-1} [52], $\dfrac{\partial n}{\partial T} = 2 \cdot 10^{-5}$ K^{-1} for nIR radiation (n_{TGG}@1064 nm $= 1.95$) and $\dfrac{1}{\mathcal{V}}\dfrac{\partial \mathcal{V}}{\partial T} = 3.5 \cdot 10^{-3}$ K^{-1} [53]. For commonly used magnets (SmCo magnets family) $\dfrac{\partial B}{\partial T} \approx 3\boldsymbol{\nabla} \cdot 5 \cdot 10^{-4}$ T/K. Thus, the main two contributors to eq(6.0.5) are the temperature dependence of the magnetic field and of the Verdet constant. Therefore we can write

$$\frac{1}{\theta_{FR}}\frac{\mathrm{d}\theta_{FR}}{\mathrm{d}T} = \frac{1}{B}\frac{\partial B}{\partial T} + \frac{1}{\mathcal{V}}\frac{\partial \mathcal{V}}{\partial T} \tag{6.0.6}$$

In the followings a thermal study of the system will be performed, demonstrating that the temperature gradients across the magnets can be minimized. Before going into details of the thermal study of the FR system, another crucial parameter will be studied.

6.1 Polarizers' polarization quality

A crucial component that defines both isolation ratio and Σ_{tr} are the polarizers. In this section three different polarizers are tested and characterized. The three sample are: the Virgo+ INJ FI

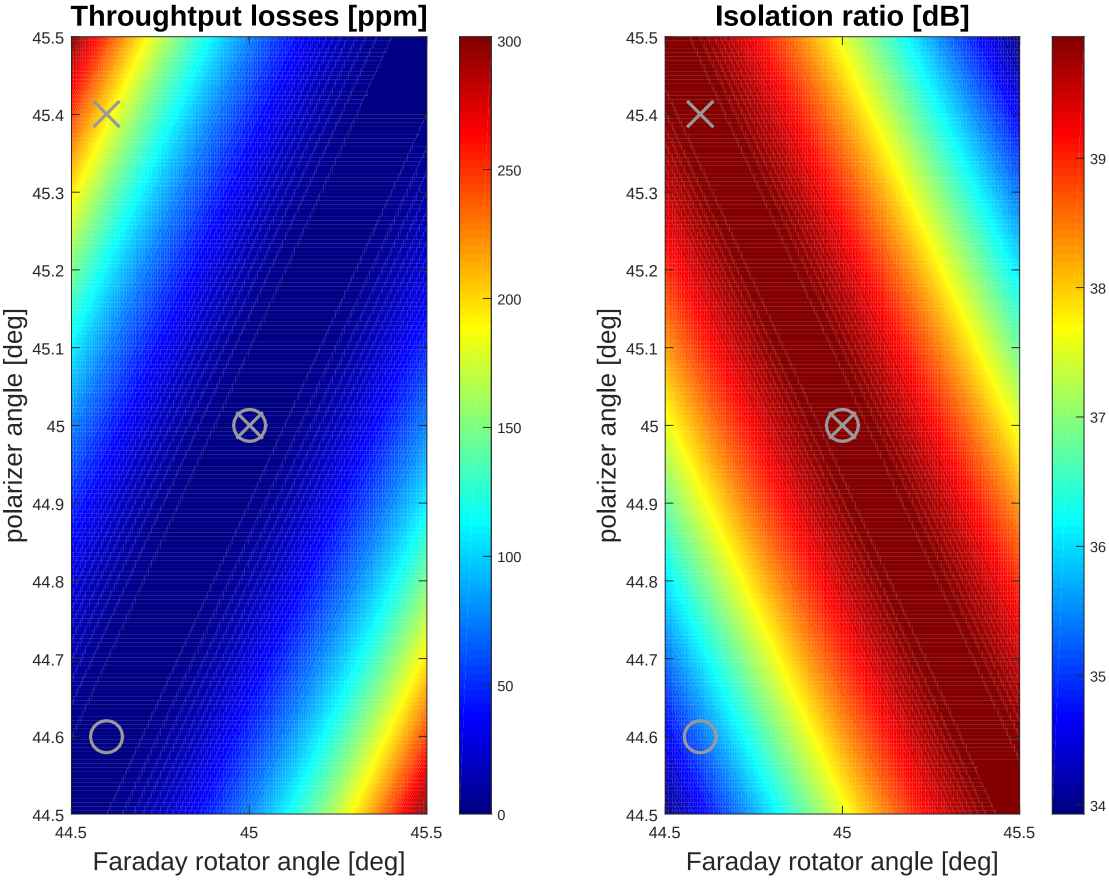

Figure 6.3: Analytical computation of (6.0.2) and (6.0.3). In the throughput losses the terms due to AR coatings and material absorption are neglected, while in the isolation ratio $p_q = 40$ dB and the thermal depolarization is ignored. All the calculation are performed at fixed temperature. The optimal performance is achievable only for rotation and polarization angle equal to 45°, while if the rotation angle is different from 45° the polarization angle can be tuned to recover the isolation despite the Σ_{tr} or vice-versa.

polarizer that is actually used in the AdV DET FI, the INJ input power control (IPC) polarizer and a fused silica, commercial polarizer that at present is not used in any of the AdV subsystem. The quantity that is commonly used to define the polarization quality is the extinction ratio (ER).

Let's define the power reflectivity of an interface as R_s for an s polarized beam and as R_p for a p polarized beam. Consequently, assuming lossless medium, the power transmittivity are $T_s = 1 - R_s$ for an s polarized beam and $T_p = 1 - R_p$ for a p polarized beam. The power reflectivity of a surface is defined by the Fresnel law (eq. (6.1.1) and (6.1.2)).

$$R_s = \left[\frac{\cos\theta_i - \sqrt{\left(\frac{n_2}{n_1}\right)^2 - \sin^2\theta_i}}{\cos\theta_i + \sqrt{\left(\frac{n_2}{n_1}\right)^2 - \sin^2\theta_i}} \right]^2 \tag{6.1.1}$$

$$R_p = \left[\frac{\left(\frac{n_2}{n_1}\right)^2 \cos\theta_i - \sqrt{\left(\frac{n_2}{n_1}\right)^2 - \sin^2\theta_i}}{\left(\frac{n_2}{n_1}\right)^2 \cos\theta_i + \sqrt{\left(\frac{n_2}{n_1}\right)^2 - \sin^2\theta_i}} \right]^2 \tag{6.1.2}$$

Fig. 6.4 (left) explains the variable used in eq. (6.1.1) and eq. (6.1.2): θ_i is the angle of incidence, θ_r is the reflection angle, θ_t is the transmission angle, n_1 and n_2 are the refractive indices of the materials. Fig. 6.4 (right) is an example of eq. (6.1.1) and eq. (6.1.2) with $n_1 = 1$ and $n_2 = 2$.

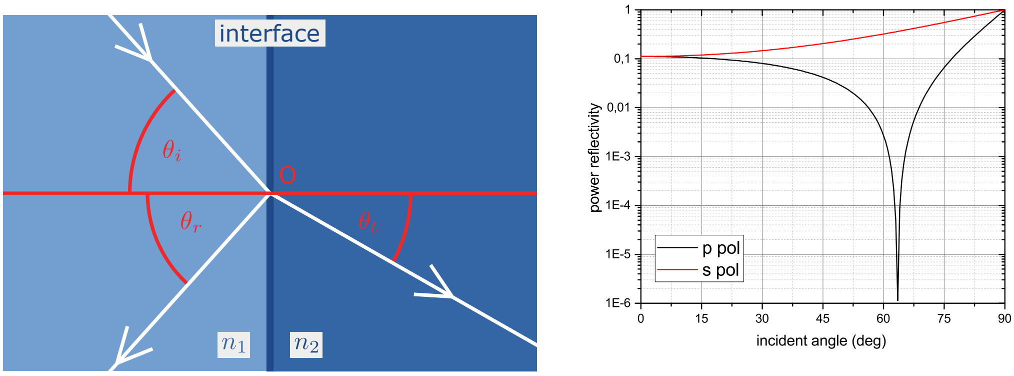

Figure 6.4: (left) Variables used in the Fresnel equations: θ_i is the angle of incidence, θ_r is the reflection angle, θ_t is the transmission angle, n_1 and n_2 are the refractive indices of the materials. (right) example of eq. (6.1.1) and eq. (6.1.2) with $n_1 = 1$ and $n_2 = 2$ as function of θ_i.

The Brewster angle θ_B is the angle at which $R_p(\theta_B) = 0$ and it is defined as

$$\tan\theta_B = \frac{n_2}{n_1} \tag{6.1.3}$$

Fig. 6.5 defines the main variables for the following. In our case the first medium is air, thus $n_1 = 1.0002740 \approx 1$ and $n_2 = n$ is the refractive index of the substrate. c_1 identifies the first interface (or coating) with respect to the impinging beam, while c_2 the second interface (or coating) with respect to the impinging beam. We define the power reflectivities of the first interface as $R_{p,1}$ and $R_{s,1}$ and the one of the second interface as $R_{p,2}$ and $R_{s,2}$. Transmission losses for p polarized light are

$$\Sigma_{T,p} = 1 - T_{p,1}(1 - \alpha\ell)\, T_{p,2} \tag{6.1.4}$$

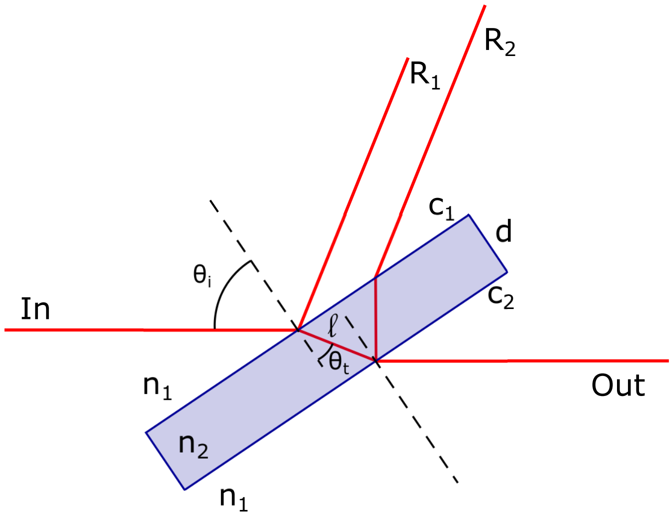

Figure 6.5: Sketch of the polarizer. θ_i and θ_t are the incidence and transmission angle respectively. n_1 is the refractive index of the material surrounding the polarizer, that in our case is air, thus $n_1 \approx 1$; n_2 is the refractive index of the polarizer material ($n_2 = 1.4496$ for fused silica and $n_2 = 1.5066$ for BK7). ℓ is the optical path length inside the polarizer and d is the thickness of the polarizer. R_1 identifies the first reflected ray, while R_2 identifies the second reflected ray; c_1 and c_2 identify respectively the first and the second interface with respect to the impinging beam.

where α is the material absorption per centimeter (e.g. $\alpha \approx 100$ ppm/cm for fused silica and $\alpha \approx 1000$ ppm/cm for BK7) and ℓ is the optical path inside the substrate. In the case of an uncoated substrate, transmission losses for p polarized light are minimal for $\theta_i = \theta_B$. In this case $\ell = d/n\,\sqrt{1+n^2}$, where d is the thickness of the substrate. Reflection losses for s polarized light are defined as the power transmittivity on s polarization of the first interface:

$$\Sigma_{R,s} = T_{s,1} \tag{6.1.5}$$

Eq. (6.1.5) is correct if there is no reflection at the second interface of the substrate (i.e. the R_2 beam of Fig. 6.5 can be neglected or properly stopped).

We define the extinction ratio in transmission (for p polarization) as

$$\mathrm{T}_{\mathrm{ER},p} = -10\log_{10}\left(\frac{T_s}{T_p}\right) \tag{6.1.6}$$

where $T_s = T_{s,1}(1-\alpha\ell)\;T_{s,2}$ is the total transmission of the polarizer on s polarized light and $T_p = T_{p,1}(1-\alpha\ell)\;T_{p,2}$ is the total transmission of the polarizer on p polarized light. In reflection, the extinction ratio (for s polarization) is

$$\mathrm{R}_{\mathrm{ER},s} = -10\log_{10}\left(\frac{R_p}{R_s}\right) \tag{6.1.7}$$

Expected target for an ideal polarizer are

$$T_{p,1} \to 1$$
$$R_{s,1} \to 1$$
$$T_{p,2} \to 1$$

Our requirements are transmission (for p pol) and reflection (for s pol) losses smaller than 0.5%, transmission extinction ratio for p polarized light greater than 40 dB and reflection extinction ratio for s polarized light greater than 30 dB.

6.1.1 Experimental setup

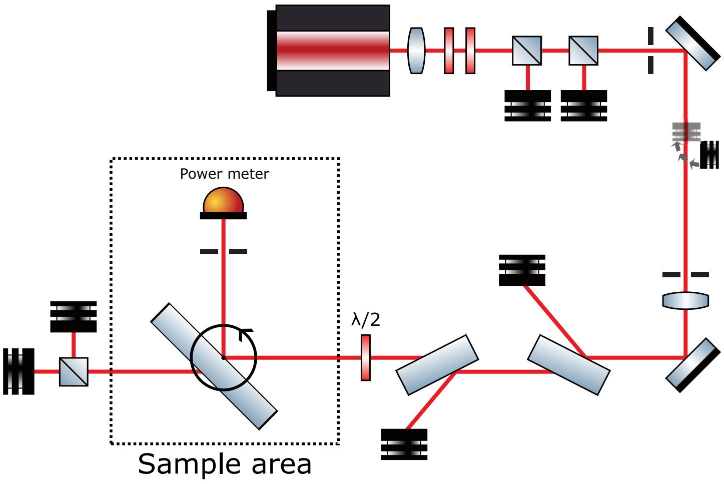

Figure 6.6: Experimental setup realized to characterize the transmission losses and the extinction ratio of various polarizers. To perform the study as function of the incidence angle θ_i, the sample is hosted on a rotating platform.

Fig. 6.6 shows the experimental setup realized to characterize the transmission losses and the extinction ratio of polarizers. The beam of the laser source (Lightwave M126N-1064-700) is folded twice before arriving to the "Sample area" where polarizer under study is placed. Since the mirrors degrade the polarization quality of the beam, before the sample area the beam polarization is cleaned using two Brewster polarizers. The measured polarization quality of the beam after the halfwave plate, just before the sample area, is 44.6 dB. The halfwave plate is placed on a high precision rotation mount (Thorlabs - PRM1/M). By rotating the waveplate before the sample area one can select different input polarization to the sample.

By placing the power meter as in Fig6.6 one can measure $R_{p,1}(\theta_i)$, $R_{s,1}(\theta_i)$, $R_{p,2}(\theta_i)$, $R_{p,2}(\theta_i)$, while, by placing the power meter on the transmitted beam of the sample $T_p(\theta_i)$ and $T_s(\theta_i)$ can be measured.

In the following a relative error of 5% is assumed for all the reflectivities and transmittivities.

6.1.2 Virgo+ INJ FI polarizer

In this section I present the characterization of the polarizer that was used in the Virgo+ INJ Faraday isolator. This polarizer is currently used in on the AdV DET Faraday isolator.

This polarizer is provided by the Electro-Optics Technology (EOT) company. It's formed by a BK7 rectangular substrated coated only on the surface c_1 (see Fig.6.5). The coating is a so called Brewster coating, that is high reflective for s polarized light and anti reflective for p polarized light, both at $\theta_i = \theta_B$. As said, c_2 is uncoated.

Fig.6.8 shows the c_1 surface reflectivity for p polarized light (left panel) and the c_2 surface reflectivities for s and p polarized light as function of the incident angle. Fitting $R_{2,p}(\theta_i)$ for this

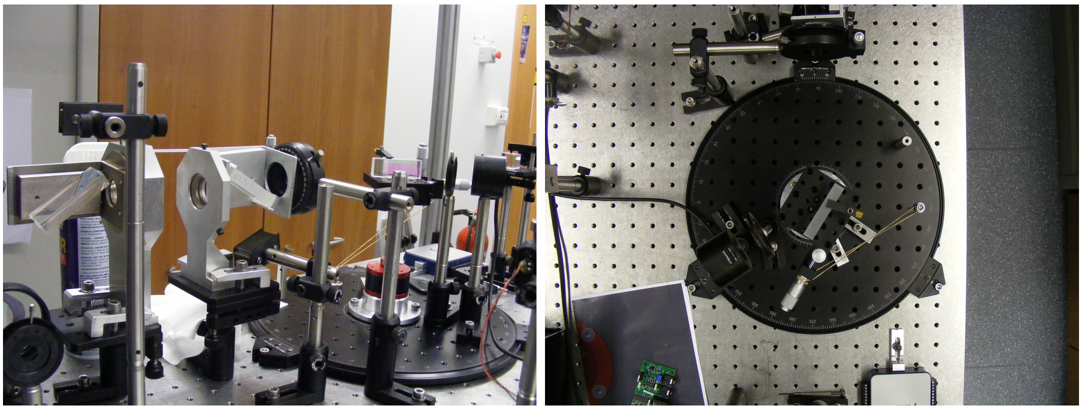

Figure 6.7: Images of the experimental setup realized to test the performances of several type of Brewster polarizers. (left) Photo of the sample area and of the two polarizers used to clean the polarization before the sample area. (right) Top view of the sample are with a sample in place.

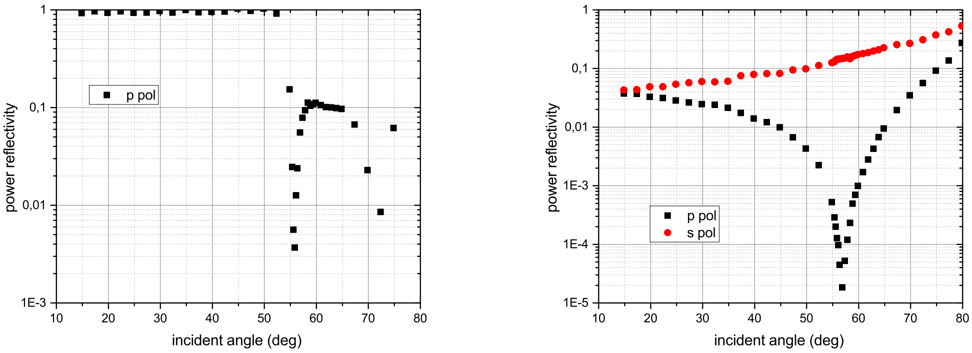

Figure 6.8: Coating characterization of the Virgo+ INJ FI polarizer. (left) c_1 surface reflectivity for p polarized light as function of the incident angle. (right) c_2 surface reflectivity for s and p polarized light as function of the incident angle. Fitting $R_{2,p}(\theta_i)$ using eq(6.1.2), the material refractive index estimated value is $n = 1.505 \pm 0.022$.

sample with eq. (6.1.2) results in $n = 1.505 \pm 0.022$ which is compatible with the tabulated data ($n = 1.5066$)[1] for BK7 glass.

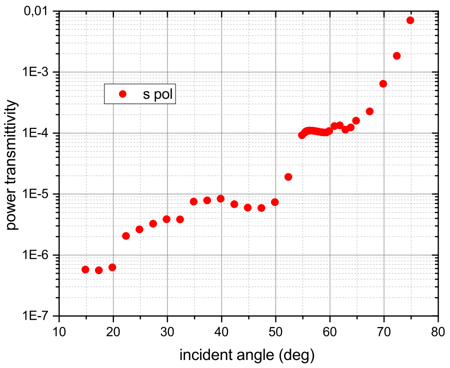

Figure 6.9: Total transmittivity for s polarized light as function of the incident angle. The total transmittivity takes into account the transmittivity of the first and the second surface and the material absorption.

Fig.6.9 shows the total transmittivity for s polarized light as function of the incident angle. Using the reflectivity of the c_1 surface for p polarized light ($R_{1,p}(\theta_i)$), the reflectivities for s and p polarized light at the c_2 surface ($R_{2,s}(\theta_i)$ and $R_{2,p}(\theta_i)$) and the polarizer total transmittivity ($T_s(\theta_i)$), the extinction ratio and the losses in transmission and in reflection are computed using equations from (6.1.4) to (6.1.7).

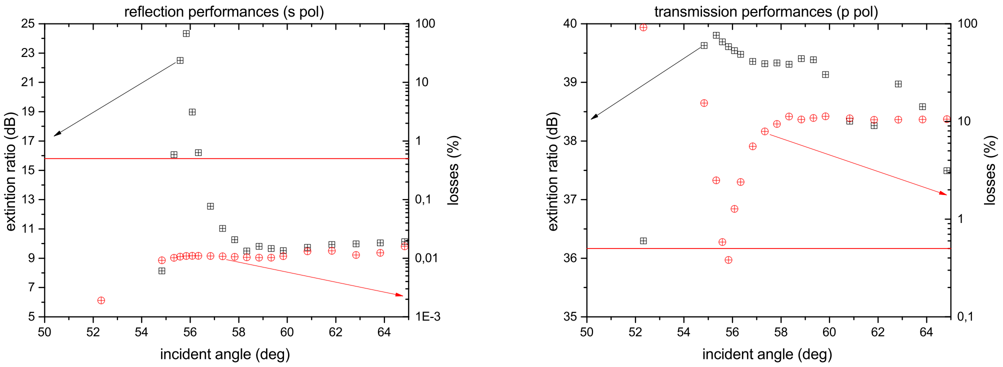

Figure 6.10: Performance of the Virgo+ INJ FI polarizer. The red horizontal line in both plots represents the 0.5% losses that are the target losses for this kind of optics. The black dots are the extinction ratio as function of the incident angle, while the red dots are the total losses as function of the incident angle. (left) Reflection performances for s polarized light. (right) Transmission performances for p polarized light.

Fig.6.10 shows the reflection and transmission performances of the Virgo+ INJ FI polarizer.

---

[1] `http://refractiveindex.info/?shelf=glass&book=BK7&page=SCHOTT`

This sample shows $39 - 40$ dB extinction ratio in transmission for p polarized light for a wide range of incident angles and the transmission losses for p polarized light are within the requirement in a small range of incident angles. The reflection losses are well within the requirements for all the incident angle, the reflection extinction ratio for s polarized light is not fulfilling the requirements at any incident angle.

When the AdV DET Faraday isolator has been installed on SDB1, the two polarizers have been characterized and the measured transmission losses are $\approx 2.5\%$. Thus I infer from Fig.6.10 (right) that the polarizer alignment is not optimized to minimize the transmission losses but to maximize the isolation ratio.

6.1.3 EOT polarizer

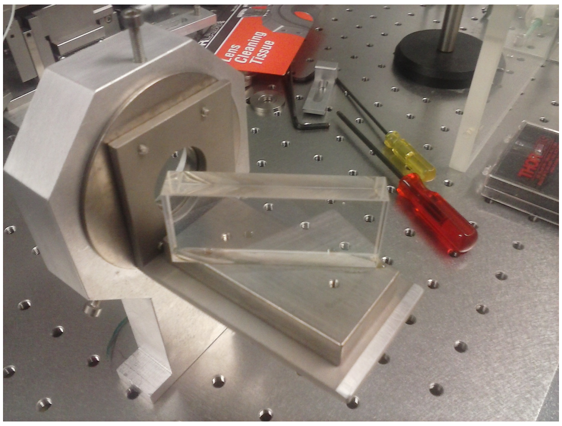

Figure 6.11: Picture of the mounted EOT polarizer (fused silica substrate).

The polarizer whose characterization is reported in this section is not presently used in any FI within the AdV collaboration. The polarizer substrate is a fused silica rectangular substrate and the polarizer surfaces have the same coating type of the Virgo+ INJ FI polarizer (i.e. c_1 has a Brewster coating and c_2 is uncoated). Note that since BK7 and fused silica have different refractive index, fused silica's θ_B is different from BK7's θ_B. The main advantage of fused silica is that this material shows absorption losses per unit length one order of magnitude smaller than the ones of BK7. Also this polarizer is provided by Electro-Optics Technology (EOT). Fig.6.11 shows a picture of the EOT polarizer.

Fig.6.12 shows the c_1 surface reflectivity for p polarized light (left panel) and the c_2 surface reflectivities for s and p polarized light as function of the incident angle. Fitting $R_{2,p}(\theta_i)$ for this sample with eq. (6.1.2) results in $n = 1.459 \pm 0.006$. The result of the fit is compatible in two σ with the tabulated refractive index $(n = 1.4496)^2$ for fused silica.

Fig.6.13 shows the total transmittivity for s polarized light as function of the incident angle. Using $R_{1,p}(\theta_i)$ from Fig.6.12 (left), $R_{2,s}(\theta_i)$ and $R_{2,p}(\theta_i)$ from Fig.6.12 (right) and $T_s(\theta_i)$ shown in Fig.6.13, the extinction ratio and the losses in transmission and in reflection are computed using equations from (6.1.4) to (6.1.7).

Fig.6.14 shows the performances of the EOT polarizer. This type of polarizer shows very low losses in both reflection and transmission; in particular, in reflection the requirements (that are $\Sigma_{R,s} < 0.5\%$ and $R_{\mathrm{ER},s} > 30$ dB) are fulfilled for $\theta_i \in [53°, 57°]$. In transmission, the losses

---

[2] `http://refractiveindex.info/?shelf=glass&book=fused_silica&page=Malitson`

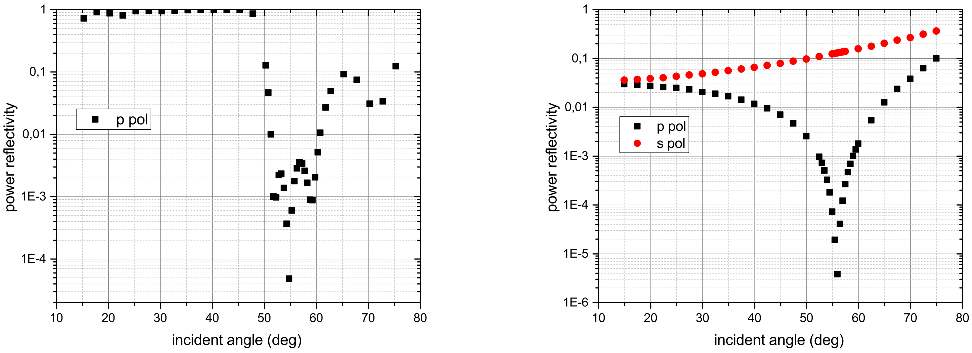

Figure 6.12: Coating characterization of the EOT polarizer. (left) c_1 surface reflectivity for p polarized light as function of the incident angle. (right) c_2 surface reflectivity for s and p polarized light as function of the incident angle.

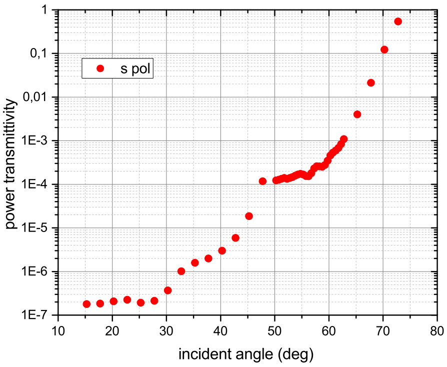

Figure 6.13: Total transmittivity for s polarized light as function of the incident angle $(T_s(\theta_i))$

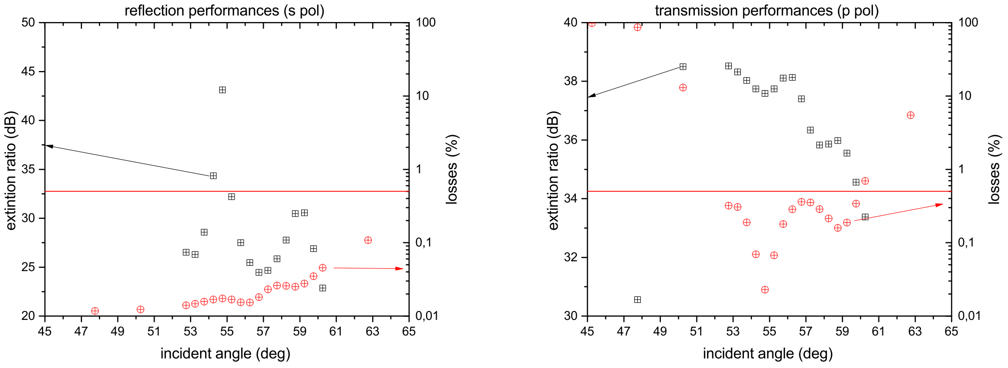

Figure 6.14: Performance of the EOT polarizer. In both plots the red horizontal line represents 0.5% of transmission (right) or reflection (left) losses. The black dots are the transmission and reflection extinction ratio, while the red dots are the transmission and reflection losses as function of the incident angle.

are within the requirement for a wide set of incident angles, but the extinction ratio is few dB below the requested value of 40 dB. As shown in this figure, for an incident angle of $\theta_i \approx 55°$, the transmission and reflection losses are smaller than 500ppm, the reflection extinction ratio is much higher than the requested 30 dB while the extinction ratio in transmission is near 38 dB.

6.1.4 INJ IPC polarizer

The polarizer presented in this section is used in the AdV INJ input power control (IPC). This system allows the control of the injected power into the interferometer and it's formed by three of this polarizers and a half-wave plate.

The polarizer is constituted by a rectangular fused silica substrate (20 mm × 55 mm × 10 mm) provided by SOLID company. The substrate has been coated from Laboratoire des Matriaux Avancs (LMA) in Lyon. This laboratory is part of the AdV collaboration. The coatings are a Brewster coating on the surface c_1, while the surface c_2 has been coated with an anti reflective coating for both the polarizations.

Fig.6.15 shows the coating's characterization of the INJ IPC polarizer. The main difference of this polarizer compared to the previous two is that the c_2 surface is coated with an antireflective coating instead of being uncoated. The right panel of the figure shows that the c_2 reflectivity for p polarized light is remarkably higher compared to the same quantity of the other two polarizers considered. Moreover, comparing the left and the right panel of Fig.6.15, the two coatings seems to be optimized for two different incident angle: the reflectivity for p polarized light of the c_1 surface has a minimum at $\theta_i = 58°$, while the reflectivities of c_2 surface have the minimum at $\theta_i = 53°$ for s polarized light and at $\theta_i = 48°$ for p polarized light.

As did for the previous two polarizers, using the quantities measured and showed in Fig.6.15 and Fig.6.16 and using the equations from (6.1.4) to (6.1.7), the extinction ratio and the losses in reflection and in transmission are computed.

Fig.6.17 shows the performances of the INJ IPC polarizer. As clear from the right panel of the figure, this polarizer shows very high transmission losses. This is mainly due to the high reflectivity for p polarized light of the antireflective coating of c_2 surface. In reflection, the losses

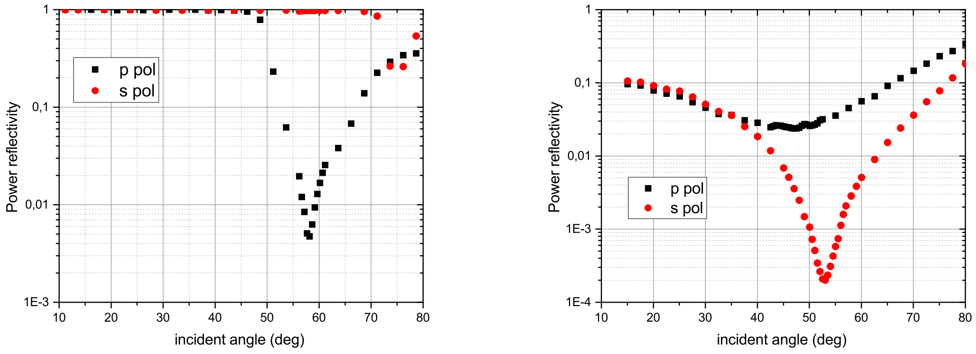

Figure 6.15: Characterization of the INJ IPC polarizer's coatings. (left) c_1 reflectivities for s and p polarized light. (right) c_2 reflectivity for s and p polarized light.

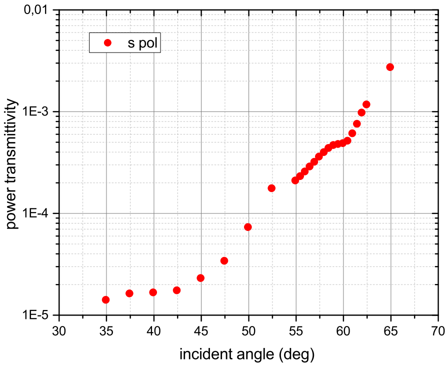

Figure 6.16: Total transmission for s polarized light measured on the INJ IPC polarizer.

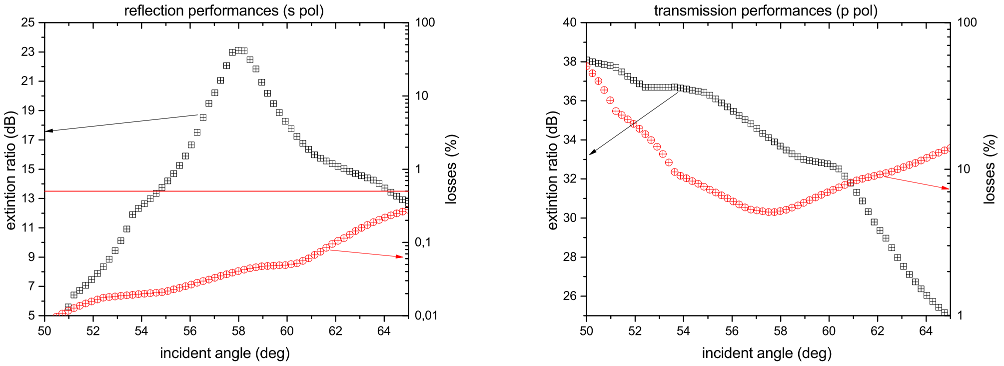

Figure 6.17: Reflection and transmission performances of the INJ IPC polarizer. The red horizontal line marks the required 0.5% of losses.

requirement is fulfilled, but the extinction ratio for s polarized light is 6 dB lower compared to the requirements. Also in transmission the extinction ratio is at best 2 dB below the requirements, and it drops to 34 dB for the incidence angle that minimizes the transmission losses ($\theta_i \approx 58°$).

6.1.5 Polarizers' summary

The polarizer with the best performances among the measured polarizers is the fused silica EOT polarizer 6.1.3. The INJ IPC polarizer exibits high losses, mainly due to the AR coating on c_2.

For the AdV squeezed light source FI, new polarizers will be realized: fused silica substates will be coated with the EOT polarizer configuration:

- c_1: Brewster coating (HR@θ_B for s pol, AR@θ_B for p pol)
- c_2: uncoated

To obtain high performance the request on the Brewster coating are:

- T_s@(55.4 ± 2)deg $< 0.01\%$
- R_p@(55.4 ± 2)deg $< 0.1\%$

The incidence angle is the less critical parameter since, for the uncoated surface, $R_p < 0.1\%$ for every incident angles $\theta_i = \theta_B \pm 3°$. With these numbers the polarizer should have transmission losses smaller than 1000ppm, reflection losses smaller than 100ppm, transmission extinction ratio higher than 40dB and reflection extinction ratio higher than 30dB.

6.2 Thermal design

In this section, the thermal study of a new vacuum compatible FR is performed. This FR I designed is shown in Fig.6.20 (left). The thermal isolation of the magnetic part of the system from the TGG crystal is crucial to reduce the polarization angle variation due to thermal fluctuation, as explained in eq(6.0.6).

The thermal characteristics of the TGG crystal have been numerically simulated with a commercial finite element modelling software. The crystal is a cylinder 12 mm in diameter and 18 mm in length. In the simulation the TGG crystal radiates from the two flat surfaces to the room at a temperature of 293 K; heat transfer via convection is neglected since the crystal is supposed to be in vacuum. The curved surface of the crystal is thermalized to a constant temperature T_b which is a variable of the simulations and ranges from $T_b = 280$ K to $T_b = 330$ K. The input beam has a waist of 600 µm placed at the center of the TGG crystal. The input power is also a variable and ranges from $P_{in} = 10$ W to $P_{in} = 200$ W.

To determine the absorption coefficient to be used in the simulations, I measured it in two different samples, resulting in $\alpha = 1800$ppm/cm.

Fig.6.18 shows a typical result of the simulations performed. In this case $T_b = 300$ K and $P_{in} = 100$ W. The left panel of the figure shows a color map of the temperature inside the crystal. The map has been calculated for a generic plane that contains the optical axis. On the right panel, the temperature profile and the temperature gradient are shown. Both these two quantities are computed at the middle of the crystal.

The performed simulations show that the thermal gradient has a weak dependance on T_b and it is mainly defined by P_{in} for any input power value in the analyzed range. As expected, the temperature profile mimic the gaussian beam spatial energy distribution and T_b only set a temperature offset between different temperature profiles (at fixed input power).

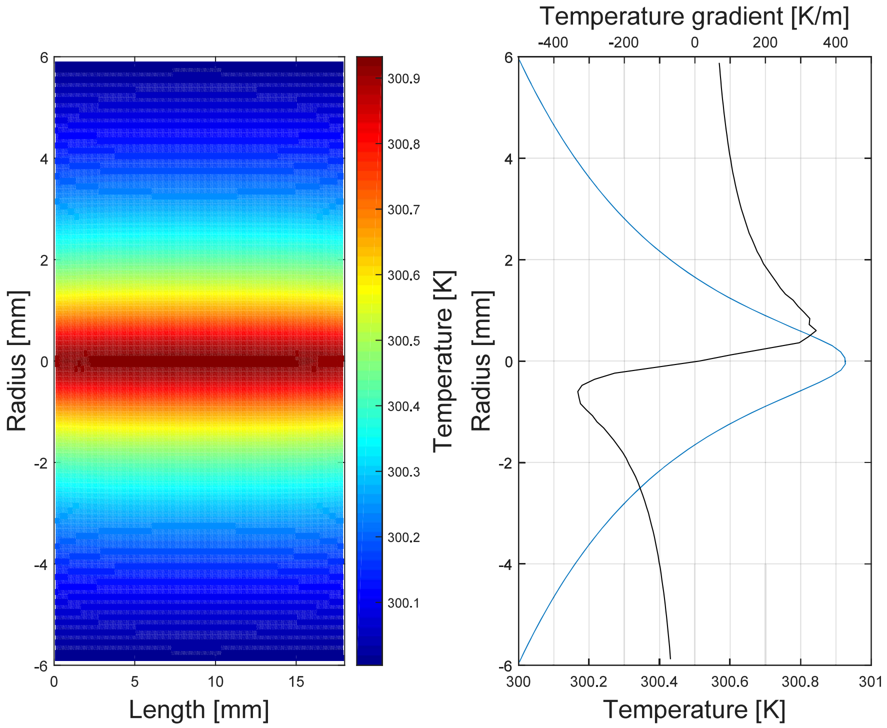

Figure 6.18: Thermal simulation of the TGG crystal. For this particular case $T_b = 300$ K and $P_{in} = 100$ W. (left) Temperature color map of a plane that contains the optical axis. (right) Temperature profile and thermal gradient computed at the center of the crystal.

The thermal study of the other components of the FR has been realized analytically.

There is an electrical analogy with conduction heat transfer that can be exploited in problem solving. The analog of $\dot{Q}$ is current, and the analog of the temperature difference, $T_1 - T_2$, is voltage difference. From this perspective a slab is a pure resistance to heat transfer and we can define

$$\dot{Q} = \frac{T_1 - T_2}{R} \tag{6.2.1}$$

where $R = L/kA$ is the thermal resistance of the slab, while L is its width, A its area and k is the thermal conductivity of the slab's material. Fig.6.19 shows two example of composite slabs.

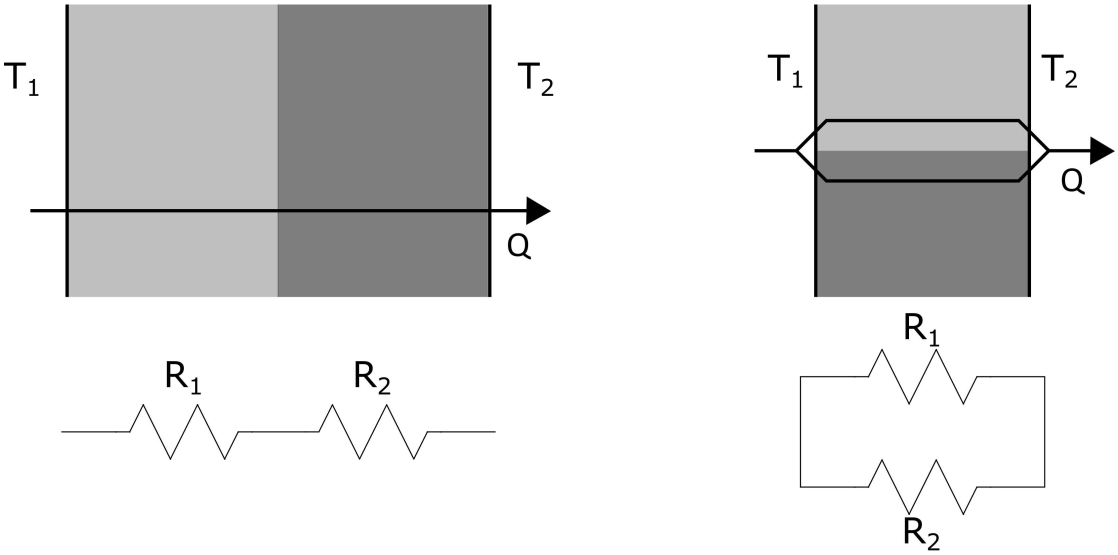

Figure 6.19: Series (left) and parallel (right) of thermal resistors.

For the FR of Fig.6.20(left) the computation of the thermal resistance between the TGG and the environment is not trivial as can be appreciate in Fig.6.20. In the left panel we have the crystal in blue, the copper crystal-holder in orange, the magnetic system in black, the peltier cell in gray and two spacers in yellow. Particular attention has been devoted to these two last components since, as shown in Fig.6.20 (right), to minimize the heat flux across the magnetic system, the parallel resistance of the two spacers R_{Sp} must be much higher than the resistance of the heat sink (R_{pillar}) between the peltier and the thermal bath (that, in vacuum, is the optical bench).

All the materials in use inside the magnetic field must exibit a magnetic permeability μ as close as possible to the vacuum one μ_0. In Tab.6.1 thermal and magnetic properties of the chosen material are reported.

The thermal connection between the peltier and the optical bench is performed by a 2 mm thick copper plate. The thermal resistance of this component is $R_{pillar} = 2.56$ K/W. The thermal resistance of the internal spacer R_{intSp} is the parallel between the resistance of the spacer itself and of the screw used to attach it to the copper holder. To maximize this resistance, titanium screws are used and the spacer is realized in Peek. Overall $R_{intSp} \approx 55$ K/W. Also for the external spacer the total resistance R_{extSp} is the parallel between screws and spacer itself. In this case $R_{extSp} \approx 20$ K/W. The parallel between these two resistances is $R_{Sp} \approx 15$ K/W that is a factor of 6 larger compared to R_{pillar}. The calculations are performed considering a

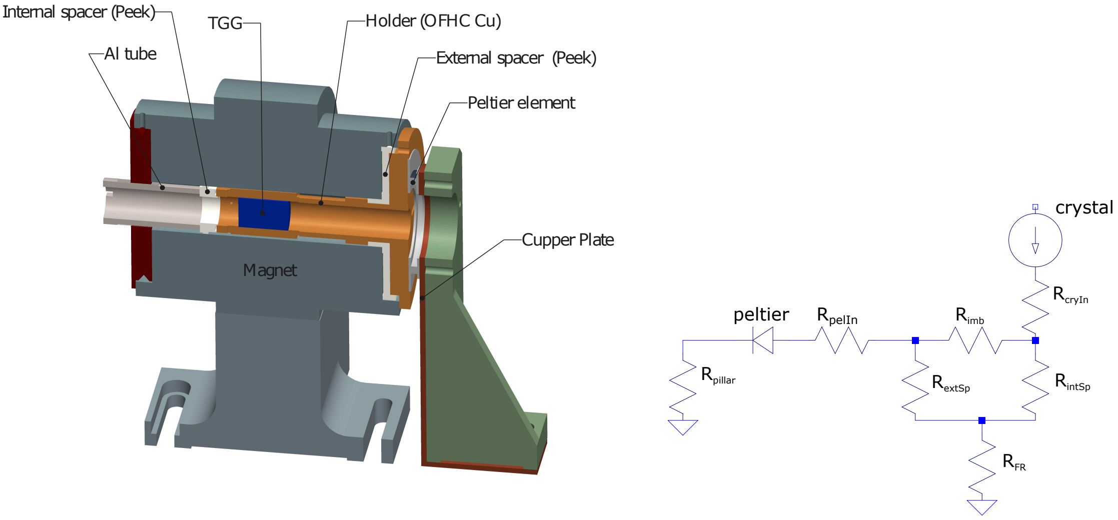

Figure 6.20: (left) Image of the vertical section of the FR. (right) FR thermal model.

Material	Thermal conductivity [W/Km]	$\mu/\mu_0 - 1$
Brass	125	$9 \cdot 10^{-5} \pm 3 \cdot 10^{-5}$
Titanium	6.7	$7.5 \cdot 10^{-5} \pm 2.5 \cdot 10^{-5}$
OFHC copper	391	$2 \cdot 10^{-5} \pm 2 \cdot 10^{-5}$
Al 7075	130	$2.2 \cdot 10^{-5}$
Macor	1.46	
Teflon	0.25	
Peek	0.25	
Indium	86	$10.2 \cdot 10^{-6}$
TGG	7.4	$0.88 \cdot 10^{-2}$

Table 6.1: Summary of thermal and magnetic properties of materials used in the FR.

perfect contact between interacting surfaces. This semplification holds true for R_{pillar} but not in the case of R_{Sp}, therefore $R_{Sp} \approx 15$ K/W is just a lower limit and the ratio between R_{Sp} and R_{pillar} can be much higher. The other resistances that are present in Fig.6.20 (right) are: the resistance $R_{cryIn} = 15.4$ mK/W of the indium sheet between the crystal and the copper support placed to ensure a good thermal conduction between them, the resistance $R_{imb} = 1.7$ K/W of the OFHC copper holder and the resistance $R_{pelIn} = 3.22$ mK/W of the indium sheet between the copper support and the peltier element again placed to ensure a good thermal conduction between them. The thermal resistance of the peltier is supposed to be zero.

Fig.6.21 shows a detail of the TGG crystal holder with the internal and external spacers.

6.3 In vacuum Faraday Isolator

In this section I present the results obtained on the developed in vacuum Faraday Isolator prototype.

The prototype is composed by a commercial magnet (provided by EOT), a wedged TGG

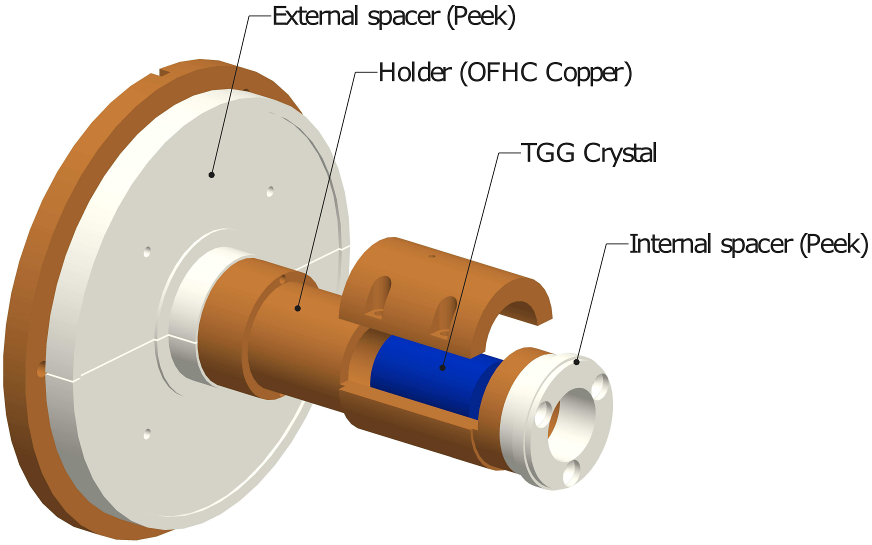

Figure 6.21: Detail of the TGG crystal holder with the internal and external spacers.

crystal with anti reflective coating on both sides, and two fused silica EOT polarizers (see 6.1.3). I measured the residual reflectivity of the TGG's AR coating, finding $R_{TGG} = 0.8\%$ on each surface. This value is not within the requirements ($R_{TGG} < 0.25\%$).

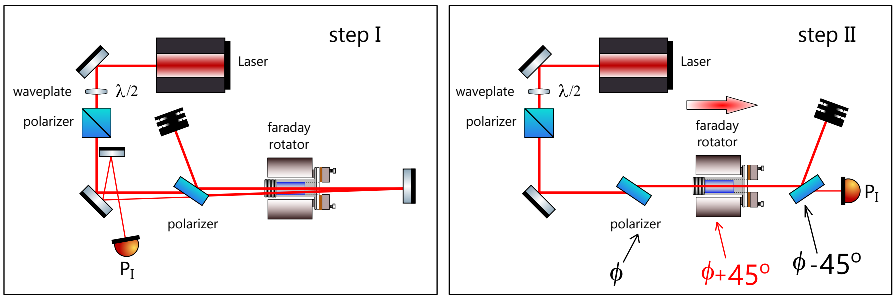

Figure 6.22: Optical set-up for the tuning of the FI. The tuning is performed in two steps. The first step involves optimizing the rotation angle for the FR by tuning the TGG crystal position in the magnetic field. The optimal TGG crystal position is achieved when the signal in reflection is minimum, regardless of the orientation of the input polarizer. For this particular optical configuration, in which the isolation is performed in transmission, the second step involves finely tuning the angle of the output polarizer to be precisely at 45° with respect to the input polarizer. In black, the angles of the polarizer axes are detailed, while in red, the beam polarization orientation after the Faraday rotator is shown.

The TGG and the polarizers have been aligned on air to maximize the isolation of the FI. The first step (left panel of Fig.6.22) involves the optimization of the TGG longitudinal axial position within the magnet of the FR. To perform this optimization, the transmitted beam of the FR is reflected back through the FR again, and the transmission through the input polarizer is collected at the photodetector P_I. Regardless the orientation of the input polarizer, the signal at P_I is minimum when the light polarization experience a 90° rotation after the two passages through the FR, therefore, the longitudinal axial position of the TGG crystal has been optimized minimizing the signal at P_I. Furthermore, the input polarizer has been rotated to have the maximum transmission through it. The second step (right panel of Fig.6.22) is performed to obtain the angular orientation of the output polarizer with respect to the input one. For this particular measurements, output polarizer has been aligned so to have the minimum transmission (i.e. to minimize the signal of P_I photodetector as in the right panel of Fig.6.22). All these action have been performed with relatively low input power ($P_{in} = 10W$) and resulted into an isolation ratio of ≈ 40 dB.

All the following measurements have been performed with the FR in vacuum (10^{-5}mbar) using the optical setup of Fig.6.23. The TGG temperature is stabilized using a PI loop. The temperature range allowed is $\pm 2°$ and this is limited by the vacuum wires dimensions that limit the maximum current that can be fed to the Peltier. For this setup the FI isolation is $-10\log(P_I/P_{in})$ and $(P_{in} - P_T)/2P_{in}$, where P_T is the transmitted power detected as in Fig.6.23, is very close to the transmission losses defined in eq(6.0.2).

Fig.6.24 shows the result of the FI isolation variation as function of the TGG crystal temperature. The input power for this measurement has been set to 10 W so to neglect the contribution to this measurement of the thermal depolarization (i.e. $\gamma = \gamma(\delta T(r)) \approx 0$). Moreover, $\partial B/\partial T$ has also been considered negligible thanks to the thermal isolation of the TGG crystal from the magnetic part of the FR. Given the stated approximations, the isolation variation data have been fitted using eq(6.0.3). The fit outcome of $\frac{1}{V}\frac{\partial V}{\partial T} = 4.0 \cdot 10^{-3}\mathrm{K}^{-1}$is in good agreement with

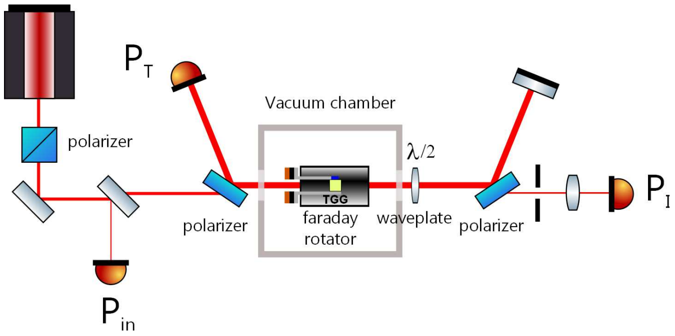

Figure 6.23: Optical set-up for characterization of the FI. The isolation ratio is computed using the transmission power measured by P_I, P_T is used to compute the losses after a double pass through the FI and P_{in} is a measurement of the input power.

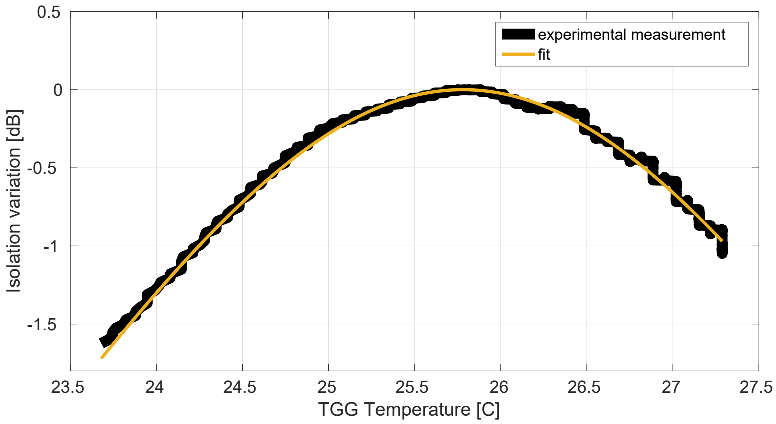

Figure 6.24: Variation of the isolation ratio with respect to the highest value reached in air as a function of the mean crystal temperature. The curve fit is done using eq(6.0.3).

the reported value of $3.5 \cdot 10^{-3}\mathrm{K}^{-1}$ [53].

This last measurement demonstrate that the isolation ratio of the FI can be tuned modifying the mean temperature of the TGG crystal. Since the mechanism that allow us this tuning is the same that appear in eq(6.0.2), we are confident that also the transmission losses can be tuned adjusting the TGG temperature. Future measurements will be performed to demonstrate this effect.

Appendix A

Optical simulation

In this appendix I'll put Finesse optical simulation and if possible analytical solutions.

A.1 Second Harmonic Generator

The Second Harmonic Generator (SHG) is an hemilitc cavity composed by a meniscous (or incoupling mirror) and a PPKTP crystal (see Fig.A.1).

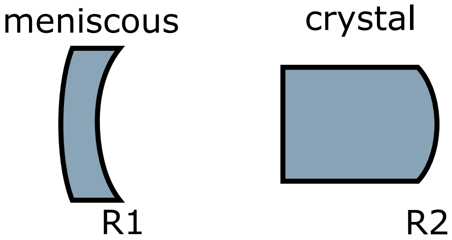

Figure A.1: Sketch of the SHG

A.1.1 Analytic results

Using the notation of "Laser" Siegman (chapter 19), we define the "resonator **g** parameters":

$$g_1 \equiv 1 - \frac{L_{opt}}{R_{1,opt}} \qquad g_2 \equiv 1 - \frac{L_{opt}}{R_{2,opt}} \tag{A.1.1}$$

where L_{opt} is the optical length of the cavity, R_1 and R_2 are the radii of curvature of the cavity's mirror normalized over the refractive index of the medium. In the case of the SHG cavity,

$$\begin{aligned} L_{opt} &= L_{air} + L_{crystal}/n_{crystal} \\ R_{1,opt} &= R_1 \\ R_{2,opt} &= R_2/n_{crystal} \end{aligned}$$

In term of the g parameters, many useful quantities can be defined. First of all, a cavity is stable if $0 \leq g_1 g_2 \leq 0$. The parameter's region where this disequation is fulfilled is called *stability region*. In Fig.A.2(a) is plotted the g_1 and g_2 product as function of L_{air}.

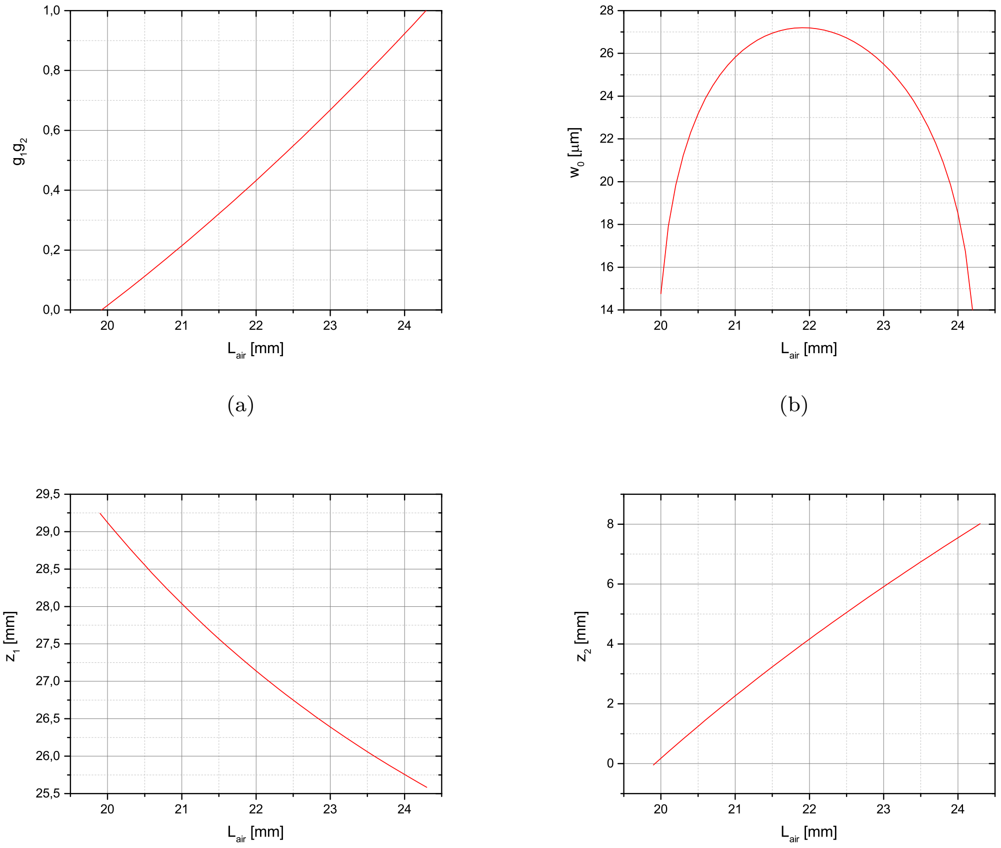

(a) (b)

(c) (d)

Figure A.2: SHG properties as function of L_{air}: (a) stability region, (b) beam waist size, (c) beam waist geometrical distance from the inner face of the meniscous and (d) beam waist geometrical distance from the curved surface of the PPKTP crystal.

Another useful parameter that can be written as function of g_1 and g_2 is the beam waist spot size, which is given by

$$w_0^2 = \frac{L_{opt}\lambda}{\pi}\sqrt{\frac{g_1 g_2(1-g_1 g_2)}{(g_1+g_2-2g_1 g_2)^2}} \tag{A.1.2}$$

where $\lambda = 1064$nm. EqA.1.2 has finite and real solution if the stability condition is fulfilled. In Fig.A.2(b) is plotted the beam waist spot size as function of L_{air}.

Other two interesting parameters are the distances of the beam waist location from the two mirrors. They are given by

$$z_{1,opt} = \frac{g_2(1-g_1)}{g_1+g_2-2g_1 g_2} \qquad \text{and} \qquad z_{2,opt} = \frac{g_1(1-g_2)}{g_1+g_2-2g_1 g_2} \tag{A.1.3}$$

FigA.2(c) and FigA.2(d) show the geometrical distances of the beam waist from the two mirrors of the cavity.

A.1.2 Finesse simulation

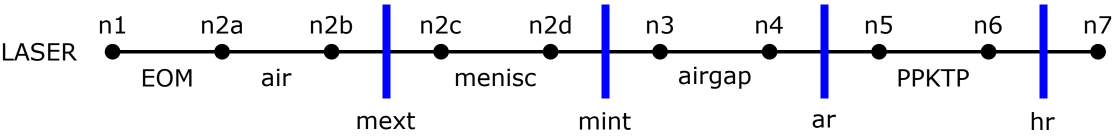

Figure A.3: Visual representation of the finesse code.

Fig.A.3 shows a representation of the components and nodes used in the finesse code. In Tab.A.1 are summarized the property of the main components.

Component name	length [mm]	refractive index	R	T	RoC [mm]
mext	—	—	0.002	0.998	-20
menisc	5.7	1.4495	—	—	—
mint	—	—	0.9	0.1	-25
airgap	$20.0\boldsymbol{\nabla}\cdot 24.2$	1	—	—	—
ar	—	—	0.005	0.995	∞
PPKTP	9.3	1.8306	—	—	—
hr	—	—	0.9997	0.0003	8

Table A.1: Property of the component used in the SHG finesse simulation

FigA.4 show a summary of the SHG finesse simulation. For the final SHG cavity the airgap chosen is $L_{air} = 22$mm. The main quantities of the cavity are summarized in TabA.2.

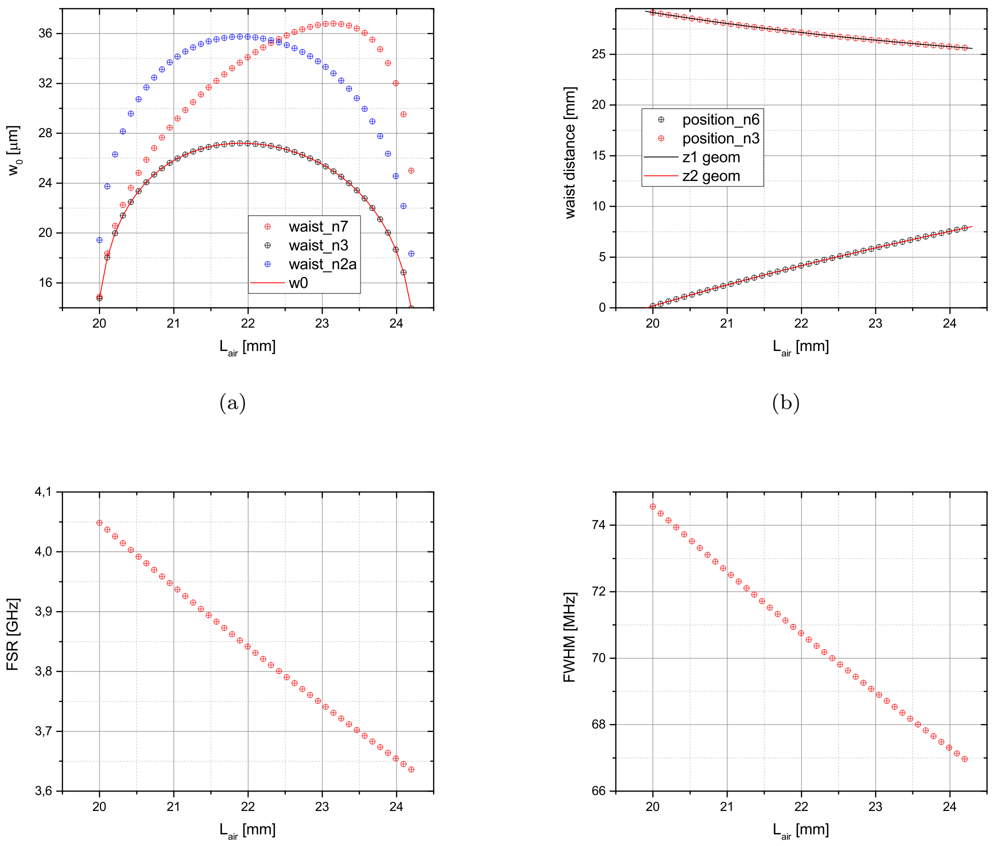

(a) (b)

(c) (d)

Figure A.4: SHG properties as function of L_{air} simulated using a Finesse code: (a) cavity waist size as seen from different nodes, Fig.A.2(b) is shown as comparison; (b) geometrical distance of the cavity waist from node n3 and node n6, FigA.2(c) and FigA.2(d) are shown as comparison; (c) cavity free spectral range (FSR); (d) cavity full width half maximum (FWHM).

L_{air}	22mm
w_0^{n2a}	35.7µm
w_0^{n3}	27.2µm
w_0^{n7}	34.1µm
waist geometrical distance from n3	27.14mm
waist geometrical distance from n6	4.15mm
FSR	3.84GHz
FWHM	70.75MHz

Table A.2: Summary of the SHG finesse simulation

Conclusions

In the next few months, Advanced Virgo will join the LIGO observatory for the second observation run (O2), making (once again) a world wide network of GW detectors. After the end of O2 and before the starting of the next observation run (O3), the Advanced Virgo detector will undertake major upgrades. One of such upgrades will be the injection of a squeezed vacuum state into the interferometer dark port. This thesis was devoted to the development of a prototype of a frequency independent squeezed vacuum source.

I studied the effect of injecting a squeezed vacuum state on the performances of the AdV detector. In particular in Chapter 3 different detector configurations, namely, power recycled Michelson interferometer, dual recycled interferometer with tuned signal recycling cavity and dual recycled interferometer with detuned signal recycling cavity are discussed. For each configuration I computed the detection ranges of binary neutron star and binary black hole coalescences as a function of the input power and of the signal recycling detuning with and without squeezing injection. For the case of no squeezing injection, the best AdV configuration for detecting binary neutron star coalescences ($M_{NS} = 1.3M_{\odot}$) is the dual recycled interferometer with 125 W of input power and 0.26 rad detuned signal recycling cavity: in this case the detection range is 146 Mpc. The best AdV configuration for detecting binary black hole coalescences ($M_{BH} = 30M_{\odot}$) is the dual recycled interferometer with 10 W of input power and 1.28 rad detuned signal recycling cavity: in this case the detection range is 1381 Mpc.

The coalescing binary ranges for AdV with squeezing has been investigate in the following detector configurations.

- Power recycled interferometer with 25 W of input power. The binary neutron star detection range is maximized with squeezing level of 3.6 dB and squeezing ellipse angle of 62° and results in 113 Mpc, which is a 5% increase with respect to the same configuration but without squeezing and still larger than the highest range obtainable with power recycled interferometer (110 Mpc with 125 W of input power). For the binary black holes, the range improvement with squeezing is 20% reaching 1183 Mpc with squeezing level of 7.8 dB and squeezing ellipse angle of 87°; this detection ranges is ≈ 100 Mpc larger compared to the highest range obtainable with power recycled interferometer (1078 Mpc with 10 W of input power).

- In the case of dual recycled interferometer with 25 W of input power and tuned signal recycling cavity, the binary neutron star detection range is maximized with squeezing level of 8.5 dB and squeezing ellipse angle of 6° and results in 119 Mpc, which is a 23% increase with respect to the same configuration but without squeezing. For the binary black holes, the range improvement with squeezing is 16% reaching 1198 Mpc with squeezing level of 8 dB and squeezing ellipse angle of 18°.

- In addition, injecting frequency independent squeezing in dual recycled AdV with tuned signal recycling cavity results in an improvement of detection ranges with respect to the ranges without squeezing in the entire range of input power.

I also investigated the benefit of injecting frequency dependent squeezed vacuum in dual recycled AdV with tuned signal recycling cavity which may be foreseen for a future upgrade. My study highlights the importance of reducing the noises other than of quantum origin that limits the sensitivity at low frequencies so to take fully advantages from the squeezed-state technique.

Since I joined the AdV squeezing working group from its start, I had the opportunity to fully contribute to the design of the squeezed vacuum source prototype. This prototype consists of three infrared laser, four Fabry-Perot cavities, a Mach-Zehnder interferometer, two phase locked loops, an homodyne detector and several other minor components. Two of the four cavities, the SHG and the OPO, are linear cavities and contain a nonlinear crystal, while the other two cavities are triangular cavities used as mode cleaners. The mechanical design adopted for the SHG and the OPO was targeted to grant high mechanical stability and therefore reduce the squeezing phase fluctuations.

I took care of the integration of many of the components installed on the prototype. In particular I personally designed and integrated the SHG cavity and the infrared mode cleaner. I realized all the *phase one* control loops, that are: the thermal control of the SHG crystal, the length control of the SHG and MCIR cavities and the Mach-Zehnder length control.

A major part of my PhD work was devoted to the second harmonic generation process. The study of the SHG process is not only important to define the SHG cavity design, but also for the design of the OPO cavity.

In Chapter 5, the characterization of the PPKTP non linear crystal performing double pass conversion measurements is presented. In this configuration I measured the second harmonic efficiency enhancement due to laser mode hop. This enhancement is explained by multiple frequency second harmonic generation, and the measurements confirms the 1.5 enhancement factor expected from theory. Using this process I realized a map of the laser mode hop as function of the laser diode pump current and of the laser NPRO crystal temperature. This map is used to define the laser crystal temperature working point and the PLLs actuation ranges.

To obtain a stable second harmonic production I realized a thermal stabilization of the nonlinear crystal by a digital control loop. This thermal loop demonstrated a residual in loop temperature fluctuation of ≈ 1 mK and an out of loop suppression of the room temperature fluctuation by a factor of 30. I defined an alignment procedure for the SHG cavity and, using this procedure, I was able to obtain a mode matching of 97.8%. I characterized the second harmonic conversion efficiency as function of the input infrared power and PPKTP crystal temperature. The highest conversion efficiency measured of 95% was achieved with an input power of 165 mW and a PPKTP crystal temperature of 304.6 K. This value represents the highest second harmonic conversion efficiency present in literature. Moreover, I found several SHG working points that fulfill the requirements for this cavity, that is the production of at least 200 mW of green power in the TEM_{00}.

To produce a squeezed state of light from an optical parametric oscillator, the pump power must be below the threshold of the OPO cavity. A precise measurement of the threshold is crucial to know the squeezing level that can be produced with an OPO. I demonstrated on two different SHG cavities that the competitive non linear processes that define the threshold in the OPO also limit the maximum second harmonic power production in the SHG cavity. The two SHG cavities differ just by the incoupling mirror reflectivity and allowed measurements of the threshold as function of the nonlinear crystal temperature.

On the SHG cavity I also measured the frequency difference of the s pol and p pol cavity resonances as function of the nonlinear crystal temperature finding a linear relation between these two quantities with a slope of 502 ± 2 MHz/K. Using the temperature dependence of the s pol and p pol resonance condition, I found a new method to measure the crystal absorption.

To inject a squeezed vacuum state into the dark port of the interferometer, Faraday isolators are necessary. They will provide both the isolation needed to avoid a seed injection from the interferometer to the OPO and also the isolation needed to avoid backscattered light from the OPO to the interferometer. In collaboration with the EGO optics group, I designed a low losses, tunable, in vacuum Faraday isolator. In particular, I performed measurements on various polarizers samples, defining the coatings requirements to have high isolation ratio as well as low transmission and reflection losses. These coatings requirements have been adopted by the collaboration.

The temperature dependence of the TGG Verdet constant is used to finely tune the isolation ratio and the transmission losses. Therefore, I performed the thermal design of the Faraday rotator with particular care to the thermal isolation of the TGG with respect to the magnets and to reduce the thermal resistance between the TGG and the Peltier element. A prototype Faraday rotator has been realized and it is currently under tests in vacuum.

Acknowledgements

I want to thank my supervisor professor Giovanni Andrea Prodi for the opportunity he gave me, for his support and for his time.

I also want to thank Jean-Pierre Zendri and Livia Conti for their support and their patience.

A great thank to my family for their support over the last years and especially to Giulia for her love. Thank you for always be there for me.

A great thank also to Marco, Sheon, Claudia, and all the people that helped me during these years.

Bibliography

[1] B. P. Abbott, R. Abbott, T. D. Abbott, M. R. Abernathy, F. Acernese, K. Ackley, C. Adams, T. Adams, P. Addesso, R. X. Adhikari, V. B. Adya, C. Affeldt, M. Agathos, K. Agatsuma, N. Aggarwal, O. D. Aguiar, L. Aiello, A. Ain, P. Ajith, B. Allen, A. Allocca, P. A. Altin, S. B. Anderson, W. G. Anderson, K. Arai, M. A. Arain, M. C. Araya, C. C. Arceneaux, J. S. Areeda, N. Arnaud, K. G. Arun, S. Ascenzi, G. Ashton, M. Ast, S. M. Aston, P. Astone, P. Aufmuth, C. Aulbert, S. Babak, P. Bacon, M. K. M. Bader, P. T. Baker, F. Baldaccini, G. Ballardin, S. W. Ballmer, J. C. Barayoga, S. E. Barclay, B. C. Barish, D. Barker, F. Barone, B. Barr, L. Barsotti, M. Barsuglia, D. Barta, J. Bartlett, M. A. Barton, I. Bartos, R. Bassiri, A. Basti, J. C. Batch, C. Baune, V. Bavigadda, M. Bazzan, B. Behnke, M. Bejger, C. Belczynski, A. S. Bell, C. J. Bell, B. K. Berger, J. Bergman, G. Bergmann, C. P. L. Berry, D. Bersanetti, A. Bertolini, J. Betzwieser, S. Bhagwat, R. Bhandare, I. A. Bilenko, G. Billingsley, J. Birch, R. Birney, O. Birnholtz, S. Biscans, A. Bisht, M. Bitossi, C. Biwer, M. A. Bizouard, J. K. Blackburn, C. D. Blair, D. G. Blair, R. M. Blair, S. Bloemen, O. Bock, T. P. Bodiya, M. Boer, G. Bogaert, C. Bogan, A. Bohe, P. Bojtos, C. Bond, F. Bondu, R. Bonnand, B. A. Boom, R. Bork, V. Boschi, S. Bose, Y. Bouffanais, A. Bozzi, C. Bradaschia, P. R. Brady, V. B. Braginsky, M. Branchesi, J. E. Brau, T. Briant, A. Brillet, M. Brinkmann, V. Brisson, P. Brockill, A. F. Brooks, D. A. Brown, D. D. Brown, N. M. Brown, C. C. Buchanan, A. Buikema, T. Bulik, H. J. Bulten, A. Buonanno, D. Buskulic, C. Buy, R. L. Byer, M. Cabero, L. Cadonati, G. Cagnoli, C. Cahillane, J. C. Bustillo, T. Callister, E. Calloni, J. B. Camp, K. C. Cannon, J. Cao, C. D. Capano, E. Capocasa, F. Carbognani, S. Caride, J. C. Diaz, C. Casentini, S. Caudill, M. Cavaglià, F. Cavalier, R. Cavalieri, G. Cella, C. B. Cepeda, L. C. Baiardi, G. Cerretani, E. Cesarini, R. Chakraborty, T. Chalermsongsak, S. J. Chamberlin, M. Chan, S. Chao, P. Charlton, E. Chassande-Mottin, H. Y. Chen, Y. Chen, C. Cheng, A. Chincarini, A. Chiummo, H. S. Cho, M. Cho, J. H. Chow, N. Christensen, Q. Chu, S. Chua, S. Chung, G. Ciani, F. Clara, J. A. Clark, F. Cleva, E. Coccia, P.-F. Cohadon, A. Colla, C. G. Collette, L. Cominsky, M. Constancio, A. Conte, L. Conti, D. Cook, T. R. Corbitt, N. Cornish, A. Corsi, S. Cortese, C. A. Costa, M. W. Coughlin, S. B. Coughlin, J.-P. Coulon, S. T. Countryman, P. Couvares, E. E. Cowan, D. M. Coward, M. J. Cowart, D. C. Coyne, R. Coyne, K. Craig, J. D. E. Creighton, T. D. Creighton, J. Cripe, S. G. Crowder, A. M. Cruise, A. Cumming, L. Cunningham, E. Cuoco, T. D. Canton, S. L. Danilishin, S. D'Antonio, K. Danzmann, N. S. Darman, C. F. Da Silva Costa, V. Dattilo, I. Dave, H. P. Daveloza, M. Davier, G. S. Davies, E. J. Daw, R. Day, S. De, D. DeBra, G. Debreczeni, J. Degallaix, M. De Laurentis, S. Deléglise, W. Del Pozzo, T. Denker, T. Dent, H. Dereli, V. Dergachev, R. T. DeRosa, R. De Rosa, R. DeSalvo, S. Dhurandhar, M. C. Díaz, L. Di Fiore, M. Di Giovanni, A. Di Lieto, S. Di Pace, I. Di Palma, A. Di Virgilio, G. Dojcinoski, V. Dolique, F. Donovan, K. L. Dooley, S. Doravari, R. Douglas, T. P. Downes, M. Drago, R. W. P. Drever, J. C. Driggers, Z. Du, M. Ducrot, S. E. Dwyer, T. B. Edo, M. C. Edwards, A. Effler, H.-B. Eggenstein, P. Ehrens, J. Eichholz, S. S. Eikenberry, W. Engels,

R. C. Essick, T. Etzel, M. Evans, T. M. Evans, R. Everett, M. Factourovich, V. Fafone, H. Fair, S. Fairhurst, X. Fan, Q. Fang, S. Farinon, B. Farr, W. M. Farr, M. Favata, M. Fays, H. Fehrmann, M. M. Fejer, D. Feldbaum, I. Ferrante, E. C. Ferreira, F. Ferrini, F. Fidecaro, L. S. Finn, I. Fiori, D. Fiorucci, R. P. Fisher, R. Flaminio, M. Fletcher, H. Fong, J.-D. Fournier, S. Franco, S. Frasca, F. Frasconi, M. Frede, Z. Frei, A. Freise, R. Frey, V. Frey, T. T. Fricke, P. Fritschel, V. V. Frolov, P. Fulda, M. Fyffe, H. A. G. Gabbard, J. R. Gair, L. Gammaitoni, S. G. Gaonkar, F. Garufi, A. Gatto, G. Gaur, N. Gehrels, G. Gemme, B. Gendre, E. Genin, A. Gennai, J. George, L. Gergely, V. Germain, A. Ghosh, A. Ghosh, S. Ghosh, J. A. Giaime, K. D. Giardina, A. Giazotto, K. Gill, A. Glaefke, J. R. Gleason, E. Goetz, R. Goetz, L. Gondan, G. González, J. M. G. Castro, A. Gopakumar, N. A. Gordon, M. L. Gorodetsky, S. E. Gossan, M. Gosselin, R. Gouaty, C. Graef, P. B. Graff, M. Granata, A. Grant, S. Gras, C. Gray, G. Greco, A. C. Green, R. J. S. Greenhalgh, P. Groot, H. Grote, S. Grunewald, G. M. Guidi, X. Guo, A. Gupta, M. K. Gupta, K. E. Gushwa, E. K. Gustafson, R. Gustafson, J. J. Hacker, B. R. Hall, E. D. Hall, G. Hammond, M. Haney, M. M. Hanke, J. Hanks, C. Hanna, M. D. Hannam, J. Hanson, T. Hardwick, J. Harms, G. M. Harry, I. W. Harry, M. J. Hart, M. T. Hartman, C.-J. Haster, K. Haughian, J. Healy, J. Heefner, A. Heidmann, M. C. Heintze, G. Heinzel, H. Heitmann, P. Hello, G. Hemming, M. Hendry, I. S. Heng, J. Hennig, A. W. Heptonstall, M. Heurs, S. Hild, D. Hoak, K. A. Hodge, D. Hofma, "Observation of gravitational waves from a binary black hole merger," *Phys. Rev. Lett.*, vol. 116, p. 061102, Feb 2016.

[2] B. P. Abbott, R. Abbott, T. D. Abbott, M. R. Abernathy, F. Acernese, K. Ackley, C. Adams, T. Adams, P. Addesso, R. X. Adhikari, V. B. Adya, C. Affeldt, M. Agathos, K. Agatsuma, N. Aggarwal, O. D. Aguiar, L. Aiello, A. Ain, P. Ajith, B. Allen, A. Allocca, P. A. Altin, S. B. Anderson, W. G. Anderson, K. Arai, M. C. Araya, C. C. Arceneaux, J. S. Areeda, N. Arnaud, K. G. Arun, S. Ascenzi, G. Ashton, M. Ast, S. M. Aston, P. Astone, P. Aufmuth, C. Aulbert, S. Babak, P. Bacon, M. K. M. Bader, P. T. Baker, F. Baldaccini, G. Ballardin, S. W. Ballmer, J. C. Barayoga, S. E. Barclay, B. C. Barish, D. Barker, F. Barone, B. Barr, L. Barsotti, M. Barsuglia, D. Barta, J. Bartlett, I. Bartos, R. Bassiri, A. Basti, J. C. Batch, C. Baune, V. Bavigadda, M. Bazzan, M. Bejger, A. S. Bell, B. K. Berger, G. Bergmann, C. P. L. Berry, D. Bersanetti, A. Bertolini, J. Betzwieser, S. Bhagwat, R. Bhandare, I. A. Bilenko, G. Billingsley, J. Birch, R. Birney, O. Birnholtz, S. Biscans, A. Bisht, M. Bitossi, C. Biwer, M. A. Bizouard, J. K. Blackburn, C. D. Blair, D. G. Blair, R. M. Blair, S. Bloemen, O. Bock, M. Boer, G. Bogaert, C. Bogan, A. Bohe, C. Bond, F. Bondu, R. Bonnand, B. A. Boom, R. Bork, V. Boschi, S. Bose, Y. Bouffanais, A. Bozzi, C. Bradaschia, P. R. Brady, V. B. Braginsky, M. Branchesi, J. E. Brau, T. Briant, A. Brillet, M. Brinkmann, V. Brisson, P. Brockill, J. E. Broida, A. F. Brooks, D. A. Brown, D. D. Brown, N. M. Brown, S. Brunett, C. C. Buchanan, A. Buikema, T. Bulik, H. J. Bulten, A. Buonanno, D. Buskulic, C. Buy, R. L. Byer, M. Cabero, L. Cadonati, G. Cagnoli, C. Cahillane, J. Calderón Bustillo, T. Callister, E. Calloni, J. B. Camp, K. C. Cannon, J. Cao, C. D. Capano, E. Capocasa, F. Carbognani, S. Caride, J. Casanueva Diaz, C. Casentini, S. Caudill, M. Cavaglià, F. Cavalier, R. Cavalieri, G. Cella, C. B. Cepeda, L. Cerboni Baiardi, G. Cerretani, E. Cesarini, S. J. Chamberlin, M. Chan, S. Chao, P. Charlton, E. Chassande-Mottin, B. D. Cheeseboro, H. Y. Chen, Y. Chen, C. Cheng, A. Chincarini, A. Chiummo, H. S. Cho, M. Cho, J. H. Chow, N. Christensen, Q. Chu, S. Chua, S. Chung, G. Ciani, F. Clara, J. A. Clark, F. Cleva, E. Coccia, P.-F. Cohadon, A. Colla, C. G. Collette, L. Cominsky, M. Constancio, A. Conte, L. Conti, D. Cook, T. R. Corbitt, N. Cornish, A. Corsi, S. Cortese, C. A. Costa, M. W. Coughlin, S. B. Coughlin, J.-P. Coulon, S. T. Countryman, P. Couvares, E. E. Cowan, D. M. Coward, M. J. Cowart, D. C. Coyne, R. Coyne, K. Craig, J. D. E. Creighton,

J. Cripe, S. G. Crowder, A. Cumming, L. Cunningham, E. Cuoco, T. Dal Canton, S. L. Danilishin, S. D'Antonio, K. Danzmann, N. S. Darman, A. Dasgupta, C. F. Da Silva Costa, V. Dattilo, I. Dave, M. Davier, G. S. Davies, E. J. Daw, R. Day, S. De, D. DeBra, G. Debreczeni, J. Degallaix, M. De Laurentis, S. Deléglise, W. Del Pozzo, T. Denker, T. Dent, V. Dergachev, R. De Rosa, R. T. DeRosa, R. DeSalvo, R. C. Devine, S. Dhurandhar, M. C. Díaz, L. Di Fiore, M. Di Giovanni, T. Di Girolamo, A. Di Lieto, S. Di Pace, I. Di Palma, A. Di Virgilio, V. Dolique, F. Donovan, K. L. Dooley, S. Doravari, R. Douglas, T. P. Downes, M. Drago, R. W. P. Drever, J. C. Driggers, M. Ducrot, S. E. Dwyer, T. B. Edo, M. C. Edwards, A. Effler, H.-B. Eggenstein, P. Ehrens, J. Eichholz, S. S. Eikenberry, W. Engels, R. C. Essick, T. Etzel, M. Evans, T. M. Evans, R. Everett, M. Factourovich, V. Fafone, H. Fair, S. Fairhurst, X. Fan, Q. Fang, S. Farinon, B. Farr, W. M. Farr, M. Favata, M. Fays, H. Fehrmann, M. M. Fejer, E. Fenyvesi, I. Ferrante, E. C. Ferreira, F. Ferrini, F. Fidecaro, I. Fiori, D. Fiorucci, R. P. Fisher, R. Flaminio, M. Fletcher, H. Fong, J.-D. Fournier, S. Frasca, F. Frasconi, Z. Frei, A. Freise, R. Frey, V. Frey, P. Fritschel, V. V. Frolov, P. Fulda, M. Fyffe, H. A. G. Gabbard, J. R. Gair, L. Gammaitoni, S. G. Gaonkar, F. Garufi, G. Gaur, N. Gehrels, G. Gemme, P. Geng, E. Genin, A. Gennai, J. George, L. Gergely, V. Germain, A. Ghosh, A. Ghosh, S. Ghosh, J. A. Giaime, K. D. Giardina, A. Giazotto, K. Gill, A. Glaefke, E. Goetz, R. Goetz, L. Gondan, G. González, J. M. Gonzalez Castro, A. Gopakumar, N. A. Gordon, M. L. Gorodetsky, S. E. Gossan, M. Gosselin, R. Gouaty, A. Grado, C. Graef, P. B. Graff, M. Granata, A. Grant, S. Gras, C. Gray, G. Greco, A. C. Green, P. Groot, H. Grote, S. Grunewald, G. M. Guidi, X. Guo, A. Gupta, M. K. Gupta, K. E. Gushwa, E. K. Gustafson, R. Gustafson, J. J. Hacker, B. R. Hall, E. D. Hall, H. Hamilton, G. Hammond, M. Haney, M. M. Hanke, J. Hanks, C. Hanna, M. D. Hannam, J. Hanson, T. Hardwick, J. Harms, G. M. Harry, I. W. Harry, M. J. Hart, M. T. Hartman, C.-J. Haster, K. Haughian, J. Healy, A. Heidmann, M. C. Heintze, H. Heitmann, P. Hello, G. Hemming, M. Hendry, I. S. Heng, J. Hennig, J. Henry, A. W. Heptonstall, M. Heurs, S. Hild, D. Hoak, D. Hofman, K. Holt, D. E. Holz, P. Hopkins, J. Hough, E. A. Houston, E. J. Howell, Y. M. Hu, S. Huang, E. A. Huerta, D. Huet, B. Hughey, S. Husa, S. H. Huttner, T. Huynh-Dinh, N. Indik, D. R. Ingram, R. Inta, H, "Gw151226: Observation of gravitational waves from a 22-solar-mass binary black hole coalescence," *Phys. Rev. Lett.*, vol. 116, p. 241103, Jun 2016.

[3] C. M. Caves, "Quantum-mechanical noise in an interferometer," *Phys. Rev. D*, vol. 23, pp. 1693–1708, Apr 1981.

[4] L. S. Collaboration *et al.*, "A gravitational wave observatory operating beyond the quantum shot-noise limit," *Nature Physics*, vol. 7, no. 12, pp. 962–965, 2011.

[5] AasiJ., AbadieJ., A. P., AbbottR., A. D., A. R., AdamsC., AdamsT., AddessoP., A. X., AffeldtC., A. D., AjithP., AllenB., A. CeronE., AmariuteiD., A. B., A. G., AraiK., A. C., ArceneauxC., AstS., A. M., AtkinsonD., AufmuthP., AulbertC., AustinL., A. E., BabakS., B. T., BallmerS., BaoY., B. C., BarkerD., BarrB., BarsottiL., B. A., BartosI., BassiriR., BatchJ., BauchrowitzJ., BehnkeB., B. S., BellC., BergmannG., B. M., BertoliniA., BetzwieserJ., BeveridgeN., B. T., BhadbhadeT., B. A., BillingsleyG., BirchJ., BiscansS., BlackE., B. K., BlackburnL., BlairD., BlandB., BockO., B. P., BoganC., BondC., BorkR., BornM., BoseS., BowersJ., B. R., B. B., B. E., BreyerJ., B. O., BrinkmannM., BritzgerM., B. F., B. A., B. D., BucklandK., BrucknerF., B. C., BuonannoA., Burguet-CastellJ., B. L., CadonatiL., C. B., CampsieP., CannonK., CaoJ., C. D., CarboneL., CarideS., C. D., CaudillS., CavagliaM., CepedaC., ChalermsongsakT., ChaoS., CharltonP., ChenX., ChenY., ChoH-S., C. H., ChristensenN., ChuQ., C. S. Y, C. T. Y., CianiG., ClaraF., C. E., C. A., C. JuniorM., CookD.,

C. R., CordierM., CornishN., CorsiA., C. A., C. W., CountrymanS., CouvaresP., C. M., CowartM., C. C., CraigK., C. D. E., C. D., CummingA., CunninghamL., DahlK., DamjanicM., D. L., DanzmannK., DaudertB., DavelozaH., D. S., D. J., DayangaT., DeleeuwE., DenkerT., DentT., DergachevV., DeRosaR., DeSalvoR., DhurandharS., D. PalmaI., DiazM., DietzA., DonovanF., D. L., DoravariS., DrascoS., D. W. P., D. C., DuZ., DumasJ-C., DwyerS., EberleT., EdwardsM., EfflerA., EhrensP., E. S., EngelR., EssickR., EtzelT., EvansK., EvansM., EvansT., FactourovichM., FairhurstS., FangQ., F. F., FarrW., FavataM., FaziD., FehrmannH., FeldbaumD., F. S., F. P., FoleyS., ForsiE., FotopoulosN., FredeM., F. A., FreiZ., FreiseA., FreyR., F. T., FriedrichD., FritschelP., F. V., FujimotoM-K., F. J., FyffeM., GairJ., GarciaJ., GehrelsN., GelencserG., G. A., GhoshS., G. A., GiampanisS., G. D., Gil-CasanovaS., GillC., GleasonJ., GoetzE., GonzalezG., GordonN., G. L., GossanS., GoszlerS., GraefC., G. B., GrantA., GrasS., GrayC., G. J. S., G. M., GriffoC., GroteH., GroverK., GrunewaldS., GuidoC., G. K., GustafsonR., HammerD., HammondG., HanksJ., HannaC., HansonJ., HarisK., HarmsJ., H. M., H. W., H. D., H. T., HaughianK., HayamaK., HeefnerJ., H. C., H. A., H. S., H. W., HeursM., HewitsonM., HildS., HoakD., H. A., HoltK., HoltropM., HongT., HooperS., HoughJ., H. J., HuangV., H. A., HugheyB., H. H., HuynhM., Huynh-DinhT., I. R., IntaR., IsogaiT., IvanovA., I. R., IzumiK., JacobsonM., JamesE., JangH., J. J., JesseE., J. W., JonesD., J. I., JonesR., JuL., KalmusP., KalogeraV., KandhasamyS., KangG., K. B., KasturiR., KatsavounidisE., KatzmanW., KauferH., KawabeK., KawamuraS., KawazoeF., KeitelD., K. B., KellsW., K. G., KhalaidovskiA., K. Y., K. A., K. K., KimC., KimK., KimN., KimY-M., K. J., K. L., K. S., KlimenkoS., KlineJ., KokeyamaK., KondrashovV., KorandaS., K. Z., KozakD., KozamehC., KreminA., KringelV., KrishnanB., KucharczykC., KuehnG., KumarP., KumarR., K. J., KurdyumovR., KweeP., L. K., LandryM., LantzB., L. D., LawrieC., LazzariniA., L. RouxA., LeaciP., LeeC-H., L. K., L. M., LeeJ., L. R., LevineB., LhuillierV., L. C., LitvineV., LiuY., LiuZ., L. A., LodhiaD., LoewK., LogueJ., L. L., LormandM., LoughJ., LubinskiM., LuckH., L. P., MacarthurJ., MacdonaldE., MachenschalkB., MacInnisM., M. M., Magana-SandovalF., MageswaranM., MailandK., MancaG., MandelI., MandicV., MarkaS., MarkaZ., M. S., MarosE., M. W., M. M., MartinovD., M. N., MasonK., MatichardF., MatoneL., M. A., MavalvalaN., MayG., MazzoloG., McAuleyK., McCarthyR., M. E., M. C., McIntyreG., McIverJ., M. D., MehmetM., MeierT., MelatosA., MendellG., M. A., MeshkovS., MessengerC., M. S., MiaoH., MillerJ., M. M. F., MitraS., M. P., MitselmakherG., MittlemanR., MoeB., MoklerF., M. R. P., MoraruD., MorenoG., MoriT., M. R., MossaviK., M.-L. M., M. L., MuellerG., MukherjeeS., MullaveyA., MunchJ., MurphyD., M. G., MytidisA., N. KumarD., NashT., NayakR., NeculaV., NewtonG., NguyenT., NishidaE., NishizawaA., NitzA., NoltingD., N. E., N. K., O'DellJ., O'ReillyB., O'ShaughnessyR., OchsnerE., OelkerE., O. H., O. J., O. H., OhmeF., OppermannP., OsthelderC., O. D., O. J., O. S., OuJ., OvermierH., O. J., PadillaC., PaiA., PanY., PankowC., P. A., ParisH., ParkinsonW., PedrazaM., PennS., PeraltaC., PerrecaA., PhelpsM., PickenpackM., PierroV., P. M., PitkinM., P. J., PoldJ., PostiglioneF., PouxC., PredoiV., PrestegardT., P. R., PrijateljM., PrivíteraS., P. G., PunckenO., QuetschkeV., QuinteroE., Quitzow-JamesR., R. J., RadkinsH., RaffaiP., RajaS., RakhmanovM., RametC., RaymondV., R. M., ReedT., ReidS., R. H., RiesenR., RilesK., RobertsM., R. A., R. L., RoddyS., RodriguezC., RodriguezL., RodruckM., R. G., R. H., RoverC., RowanS., RudigerA., RyanK., SalemiF., SammutL., SandbergV., SandersJ., SankarS., SannibaleV., SantamariaL., Santiago-PrietoI., SantostasiG., S. S., S. R., S. L., SchillingR., SchnabelR., S. M. S., SchuetteD., SchulzB., S. F., SchwinbergP., ScottJ., , “Enhanced sensitivity of the ligo gravitational wave detector by using squeezed states of light,” *Nat Photon*, vol. 7, pp. 613–619, Aug 2013. Letter.

[6] A. R. Wade, G. L. Mansell, S. S. Y. Chua, R. L. Ward, B. J. J. Slagmolen, D. A. Shaddock, and D. E. McClelland, “A squeezed light source operated under high vacuum,” *Scientific Reports*, vol. 5, pp. 18052 EP –, Dec 2015. Article.

[7] T. Isogai, E. Oelker, J. Miller, M. Tse, L. Barsotti, N. Mavalvala, and M. Evans, “Demonstration of frequency dependent squeezing in the audio frequency band,” in *Frontiers in Optics 2015*, p. FW4D.3, Optical Society of America, 2015.

[8] E. Oelker, T. Isogai, J. Miller, M. Tse, L. Barsotti, N. Mavalvala, and M. Evans, “Audio-band frequency-dependent squeezing for gravitational-wave detectors,” *Phys. Rev. Lett.*, vol. 116, p. 041102, Jan 2016.

[9] E. M. L. Lev L. Landau, *Teoria dei campi. Fisica teorica 2.* Editori Riuniti, 1976.

[10] J. Abadie, B. P. Abbott, R. Abbott, M. Abernathy, T. Accadia, F. Acernese, C. Adams, R. Adhikari, P. Ajith, B. Allen, G. Allen, E. A. Ceron, R. S. Amin, S. B. Anderson, W. G. Anderson, F. Antonucci, S. Aoudia, M. A. Arain, M. Araya, M. Aronsson, K. G. Arun, Y. Aso, S. Aston, P. Astone, D. E. Atkinson, P. Aufmuth, C. Aulbert, S. Babak, P. Baker, G. Ballardin, S. Ballmer, D. Barker, S. Barnum, F. Barone, B. Barr, P. Barriga, L. Barsotti, M. Barsuglia, M. A. Barton, I. Bartos, R. Bassiri, M. Bastarrika, J. Bauchrowitz, T. S. Bauer, B. Behnke, M. G. Beker, M. Benacquista, A. Bertolini, J. Betzwieser, N. Beveridge, P. T. Beyersdorf, S. Bigotta, I. A. Bilenko, G. Billingsley, J. Birch, S. Birindelli, R. Biswas, M. Bitossi, M. A. Bizouard, E. Black, J. K. Blackburn, L. Blackburn, D. Blair, B. Bland, M. Blom, A. Blomberg, C. Boccara, O. Bock, T. P. Bodiya, R. Bondarescu, F. Bondu, L. Bonelli, R. Bork, M. Born, S. Bose, L. Bosi, M. Boyle, S. Braccini, C. Bradaschia, P. R. Brady, V. B. Braginsky, J. E. Brau, J. Breyer, D. O. Bridges, A. Brillet, M. Brinkmann, V. Brisson, M. Britzger, A. F. Brooks, D. A. Brown, R. Budzyski, T. Bulik, H. J. Bulten, A. Buonanno, J. Burguet-Castell, O. Burmeister, D. Buskulic, R. L. Byer, L. Cadonati, G. Cagnoli, E. Calloni, J. B. Camp, E. Campagna, P. Campsie, J. Cannizzo, K. C. Cannon, B. Canuel, J. Cao, C. Capano, F. Carbognani, S. Caride, S. Caudill, M. Cavagli, F. Cavalier, R. Cavalieri, G. Cella, C. Cepeda, E. Cesarini, T. Chalermsongsak, E. Chalkley, P. Charlton, E. C. Mottin, S. Chelkowski, Y. Chen, A. Chincarini, N. Christensen, S. S. Y. Chua, C. T. Y. Chung, D. Clark, J. Clark, J. H. Clayton, F. Cleva, E. Coccia, C. N. Colacino, J. Colas, A. Colla, M. Colombini, R. Conte, D. Cook, T. R. Corbitt, C. Corda, N. Cornish, A. Corsi, C. A. Costa, J. P. Coulon, D. Coward, D. C. Coyne, J. D. E. Creighton, T. D. Creighton, A. M. Cruise, R. M. Culter, A. Cumming, L. Cunningham, E. Cuoco, K. Dahl, S. L. Danilishin, R. Dannenberg, S. D'Antonio, K. Danzmann, A. Dari, K. Das, V. Dattilo, B. Daudert, M. Davier, G. Davies, A. Davis, E. J. Daw, R. Day, T. Dayanga, R. D. Rosa, D. DeBra, J. Degallaix, M. del Prete, V. Dergachev, R. DeRosa, R. DeSalvo, P. Devanka, S. Dhurandhar, L. D. Fiore, A. D. Lieto, I. D. Palma, M. D. P. Emilio, A. D. Virgilio, M. Daz, A. Dietz, F. Donovan, K. L. Dooley, E. E. Doomes, S. Dorsher, E. S. D. Douglas, M. Drago, R. W. P. Drever, J. C. Driggers, J. Dueck, J. C. Dumas, T. Eberle, M. Edgar, M. Edwards, A. Effler, P. Ehrens, R. Engel, T. Etzel, M. Evans, T. Evans, V. Fafone, S. Fairhurst, Y. Fan, B. F. Farr, D. Fazi, H. Fehrmann, D. Feldbaum, I. Ferrante, F. Fidecaro, L. S. Finn, I. Fiori, R. Flaminio, M. Flanigan, K. Flasch, S. Foley, C. Forrest, E. Forsi, N. Fotopoulos, J. D. Fournier, J. Franc, S. Frasca, F. Frasconi, M. Frede, M. Frei, Z. Frei, A. Freise, R. Frey, T. T. Fricke, D. Friedrich, P. Fritschel, V. V. Frolov, P. Fulda, M. Fyffe, L. Gammaitoni, J. A. Garofoli, F. Garufi, G. Gemme, E. Genin, A. Gennai, I. Gholami, S. Ghosh, J. A. Giaime, S. Giampanis, K. D. Giardina, A. Giazotto, C. Gill, E. Goetz, L. M. Goggin, G. Gonzlez, M. L. Gorodetsky, S. Goler, R. Gouaty, C. Graef, M. Granata, A. Grant, S. Gras, C. Gray, R. J. S. Greenhalgh, A. M. Gretarsson, C. Greverie, R. Grosso,

H. Grote, S. Grunewald, G. M. Guidi, E. K. Gustafson, R. Gustafson, B. Hage, P. Hall, J. M. Hallam, D. Hammer, G. Hammond, J. Hanks, C. Hanna, J. Hanson, J. Harms, G. M. Harry, I. W. Harry, E. D. Harstad, K. Haughian, K. Hayama, J. Heefner, H. Heitmann, P. Hello, I. S. Heng, A. Heptonstall, M. Hewitson, S. Hild, E. Hirose, D. Hoak, K. A. Hodge, K. Holt, D. J. Hosken, J. Hough, E. Howell, D. Hoyland, D. Huet, B. Hughey, S. Husa, S. H. Huttner, T. Huynh-Dinh, D. R. Ingram, R. Inta, T. Isogai, A. Ivanov, P. Jaranowski, W. W. Johnson, D. I. Jones, G. Jones, R. Jones, L. Ju, P. Kalmus, V. Kalogera, S. Kandhasamy, J. Kanner, E. Katsavounidis, K. Kawabe, S. Kawamura, F. Kawazoe, W. Kells, D. G. Keppel, A. Khalaidovski, F. Y. Khalili, E. A. Khazanov, C. Kim, H. Kim, P. J. King, D. L. Kinzel, J. S. Kissel, S. Klimenko, V. Kondrashov, R. Kopparapu, S. Koranda, I. Kowalska, D. Kozak, T. Krause, V. Kringel, S. Krishnamurthy, B. Krishnan, A. Krlak, G. Kuehn, J. Kullman, R. Kumar, P. Kwee, M. Landry, M. Lang, B. Lantz, N. Lastzka, A. Lazzarini, P. Leaci, J. Leong, I. Leonor, N. Leroy, N. Letendre, J. Li, T. G. F. Li, H. Lin, P. E. Lindquist, N. A. Lockerbie, D. Lodhia, M. Lorenzini, V. Loriette, M. Lormand, G. Losurdo, P. Lu, J. Luan, M. Lubinski, A. Lucianetti, H. Lck, A. Lundgren, B. Machenschalk, M. MacInnis, J. M. Mackowski, M. Mageswaran, K. Mailand, E. Majorana, C. Mak, N. Man, I. Mandel, V. Mandic, M. Mantovani, F. Marchesoni, F. Marion, S. Mrka, Z. Mrka, E. Maros, J. Marque, F. Martelli, I. W. Martin, R. M. Martin, J. N. Marx, K. Mason, A. Masserot, F. Matichard, L. Matone, R. A. Matzner, N. Mavalvala, R. McCarthy, D. E. McClelland, S. C. McGuire, G. McIntyre, G. McIvor, D. J., "Predictions for the rates of compact binary coalescences observable by ground-based gravitational-wave detectors," *Classical and Quantum Gravity*, vol. 27, no. 17, p. 173001, 2010.

[11] R. A. Hulse and J. H. Taylor, "Discovery of a pulsar in a binary system," *Astrophysical Journal, Letters*, vol. 195, pp. L51–L53, Jan. 1975.

[12] J. H. Taylor and J. M. Weisberg, "A new test of general relativity - Gravitational radiation and the binary pulsar PSR 1913+16," *Astrophysical Journal*, vol. 253, pp. 908–920, Feb. 1982.

[13] J. H. Taylor and J. M. Weisberg, "Further experimental tests of relativistic gravity using the binary pulsar PSR 1913 + 16," *Astrophysical Journal*, vol. 345, pp. 434–450, Oct. 1989.

[14] M. Maggiore, "Gravitational wave experiments and early universe cosmology," *Physics Reports*, vol. 331, no. 6, pp. 283 – 367, 2000.

[15] C. D. Ott, "Probing the core-collapse supernova mechanism with gravitational waves," *Classical and Quantum Gravity*, vol. 26, no. 20, p. 204015, 2009.

[16] J. Logue, C. D. Ott, I. S. Heng, P. Kalmus, and J. H. C. Scargill, "Inferring Core-Collapse Supernova Physics with Gravitational Waves," *Phys. Rev.*, vol. D86, p. 044023, 2012.

[17] T. V. Collaboration, "Advanced virgo technical design report," *Virgo internal note*, no. VIR-0128A-12, 2012.

[18] F. Acernese, M. Agathos, K. Agatsuma, D. Aisa, N. Allemandou, A. Allocca, J. Amarni, P. Astone, G. Balestri, G. Ballardin, F. Barone, J.-P. Baronick, M. Barsuglia, A. Basti, F. Basti, T. S. Bauer, V. Bavigadda, M. Bejger, M. G. Beker, C. Belczynski, D. Bersanetti, A. Bertolini, M. Bitossi, M. A. Bizouard, S. Bloemen, M. Blom, M. Boer, G. Bogaert, D. Bondi, F. Bondu, L. Bonelli, R. Bonnand, V. Boschi, L. Bosi, T. Bouedo, C. Bradaschia, M. Branchesi, T. Briant, A. Brillet, V. Brisson, T. Bulik, H. J. Bulten, D. Buskulic, C. Buy, G. Cagnoli, E. Calloni, C. Campeggi, B. Canuel, F. Carbognani, F. Cavalier, R. Cavalieri,

G. Cella, E. Cesarini, E. Chassande-Mottin, A. Chincarini, A. Chiummo, S. Chua, F. Cleva, E. Coccia, P.-F. Cohadon, A. Colla, M. Colombini, A. Conte, J.-P. Coulon, E. Cuoco, A. Dalmaz, S. DAntonio, V. Dattilo, M. Davier, R. Day, G. Debreczeni, J. Degallaix, S. Delglise, W. D. Pozzo, H. Dereli, R. D. Rosa, L. D. Fiore, A. D. Lieto, A. D. Virgilio, M. Doets, V. Dolique, M. Drago, M. Ducrot, G. Endrczi, V. Fafone, S. Farinon, I. Ferrante, F. Ferrini, F. Fidecaro, I. Fiori, R. Flaminio, J.-D. Fournier, S. Franco, S. Frasca, F. Frasconi, L. Gammaitoni, F. Garufi, M. Gaspard, A. Gatto, G. Gemme, B. Gendre, E. Genin, A. Gennai, S. Ghosh, L. Giacobone, A. Giazotto, R. Gouaty, M. Granata, G. Greco, P. Groot, G. M. Guidi, J. Harms, A. Heidmann, H. Heitmann, P. Hello, G. Hemming, E. Hennes, D. Hofman, P. Jaranowski, R. J. G. Jonker, M. Kasprzack, F. Kflian, I. Kowalska, M. Kraan, A. Krlak, A. Kutynia, C. Lazzaro, M. Leonardi, N. Leroy, N. Letendre, T. G. F. Li, B. Lieunard, M. Lorenzini, V. Loriette, G. Losurdo, C. Magazz, E. Majorana, I. Maksimovic, V. Malvezzi, N. Man, V. Mangano, M. Mantovani, F. Marchesoni, F. Marion, J. Marque, F. Martelli, L. Martellini, A. Masserot, D. Meacher, J. Meidam, F. Mezzani, C. Michel, L. Milano, Y. Minenkov, A. Moggi, M. Mohan, M. Montani, N. Morgado, B. Mours, F. Mul, M. F. Nagy, I. Nardecchia, L. Naticchioni, G. Nelemans, I. Neri, M. Neri, F. Nocera, E. Pacaud, C. Palomba, F. Paoletti, A. Paoli, A. Pasqualetti, R. Passaquieti, D. Passuello, M. Perciballi, S. Petit, M. Pichot, F. Piergiovanni, G. Pillant, A. Piluso, L. Pinard, R. Poggiani, M. Prijatelj, G. A. Prodi, M. Punturo, P. Puppo, D. S. Rabeling, I. Rcz, P. Rapagnani, M. Razzano, V. Re, T. Regimbau, F. Ricci, F. Robinet, A. Rocchi, L. Rolland, R. Romano, D. Rosiska, P. Ruggi, E. Saracco, B. Sassolas, F. Schimmel, D. Sentenac, V. Sequino, S. Shah, K. Siellez, N. Straniero, B. Swinkels, M. Tacca, M. Tonelli, F. Travasso, M. Turconi, G. Vajente, N. van Bakel, M. van Beuzekom, J. F. J. van den Brand, C. V. D. Broeck, M. V. van der Sluys, J. van Heijningen, M. Vasth, G. Vedovato, J. Veitch, D. Verkindt, F. Vetrano, A. Vicer, J.-Y. Vinet, G. Visser, H. Vocca, R. Ward, M. Was, L.-W. Wei, M. Yvert, A. Z. ny, and J.-P. Zendri, “Advanced virgo: a second-generation interferometric gravitational wave detector,” *Classical and Quantum Gravity*, vol. 32, no. 2, p. 024001, 2015.

[19] I. Fiori, “Reference seismic data for virgo,” *Virgo internal note*, no. VIR-0390A-15, 2015.

[20] A. H. Mroué, M. A. Scheel, B. Szilágyi, H. P. Pfeiffer, M. Boyle, D. A. Hemberger, L. E. Kidder, G. Lovelace, S. Ossokine, N. W. Taylor, A. i. e. i. f. Zenginoğlu, L. T. Buchman, T. Chu, E. Foley, M. Giesler, R. Owen, and S. A. Teukolsky, “Catalog of 174 binary black hole simulations for gravitational wave astronomy,” *Phys. Rev. Lett.*, vol. 111, p. 241104, Dec 2013.

[21] M. Campanelli, C. O. Lousto, P. Marronetti, and Y. Zlochower, “Accurate evolutions of orbiting black-hole binaries without excision,” *Phys. Rev. Lett.*, vol. 96, p. 111101, Mar 2006.

[22] B. P. Abbott, R. Abbott, T. D. Abbott, M. R. Abernathy, F. Acernese, K. Ackley, C. Adams, T. Adams, P. Addesso, R. X. Adhikari, V. B. Adya, C. Affeldt, M. Agathos, K. Agatsuma, N. Aggarwal, O. D. Aguiar, L. Aiello, A. Ain, P. Ajith, B. Allen, A. Allocca, P. A. Altin, S. B. Anderson, W. G. Anderson, K. Arai, M. C. Araya, C. C. Arceneaux, J. S. Areeda, N. Arnaud, K. G. Arun, S. Ascenzi, G. Ashton, M. Ast, S. M. Aston, P. Astone, P. Aufmuth, C. Aulbert, S. Babak, P. Bacon, M. K. M. Bader, P. T. Baker, F. Baldaccini, G. Ballardin, S. W. Ballmer, J. C. Barayoga, S. E. Barclay, B. C. Barish, D. Barker, F. Barone, B. Barr, L. Barsotti, M. Barsuglia, D. Barta, J. Bartlett, I. Bartos, R. Bassiri, A. Basti, J. C. Batch, C. Baune, V. Bavigadda, M. Bazzan, B. Behnke, M. Bejger, A. S. Bell, C. J. Bell, B. K. Berger, J. Bergman, G. Bergmann, C. P. L. Berry, D. Bersanetti, A. Bertolini, J. Betzwieser, S. Bhagwat, R. Bhandare, I. A. Bilenko, G. Billingsley, J. Birch, R. Birney, O. Birnholtz,

S. Biscans, A. Bisht, M. Bitossi, C. Biwer, M. A. Bizouard, J. K. Blackburn, C. D. Blair, D. G. Blair, R. M. Blair, S. Bloemen, O. Bock, T. P. Bodiya, M. Boer, G. Bogaert, C. Bogan, A. Bohe, P. Bojtos, C. Bond, F. Bondu, R. Bonnand, B. A. Boom, R. Bork, V. Boschi, S. Bose, Y. Bouffanais, A. Bozzi, C. Bradaschia, P. R. Brady, V. B. Braginsky, M. Branchesi, J. E. Brau, T. Briant, A. Brillet, M. Brinkmann, V. Brisson, P. Brockill, A. F. Brooks, D. A. Brown, D. D. Brown, N. M. Brown, C. C. Buchanan, A. Buikema, T. Bulik, H. J. Bulten, A. Buonanno, D. Buskulic, C. Buy, R. L. Byer, L. Cadonati, G. Cagnoli, C. Cahillane, J. Calderón Bustillo, T. Callister, E. Calloni, J. B. Camp, K. C. Cannon, J. Cao, C. D. Capano, E. Capocasa, F. Carbognani, S. Caride, J. Casanueva Diaz, C. Casentini, S. Caudill, M. Cavaglià, F. Cavalier, R. Cavalieri, G. Cella, C. B. Cepeda, L. Cerboni Baiardi, G. Cerretani, E. Cesarini, R. Chakraborty, T. Chalermsongsak, S. J. Chamberlin, M. Chan, S. Chao, P. Charlton, E. Chassande-Mottin, H. Y. Chen, Y. Chen, C. Cheng, A. Chincarini, A. Chiummo, H. S. Cho, M. Cho, J. H. Chow, N. Christensen, Q. Chu, S. Chua, S. Chung, G. Ciani, F. Clara, J. A. Clark, F. Cleva, E. Coccia, P.-F. Cohadon, A. Colla, C. G. Collette, L. Cominsky, M. Constancio, A. Conte, L. Conti, D. Cook, T. R. Corbitt, N. Cornish, A. Corsi, S. Cortese, C. A. Costa, M. W. Coughlin, S. B. Coughlin, J.-P. Coulon, S. T. Countryman, P. Couvares, E. E. Cowan, D. M. Coward, M. J. Cowart, D. C. Coyne, R. Coyne, K. Craig, J. D. E. Creighton, J. Cripe, S. G. Crowder, A. Cumming, L. Cunningham, E. Cuoco, T. Dal Canton, S. L. Danilishin, S. D'Antonio, K. Danzmann, N. S. Darman, V. Dattilo, I. Dave, H. P. Daveloza, M. Davier, G. S. Davies, E. J. Daw, R. Day, D. DeBra, G. Debreczeni, J. Degallaix, M. De Laurentis, S. Deléglise, W. Del Pozzo, T. Denker, T. Dent, H. Dereli, V. Dergachev, R. De Rosa, R. T. DeRosa, R. DeSalvo, C. Devine, S. Dhurandhar, M. C. Díaz, L. Di Fiore, M. Di Giovanni, A. Di Lieto, S. Di Pace, I. Di Palma, A. Di Virgilio, G. Dojcinoski, V. Dolique, F. Donovan, K. L. Dooley, S. Doravari, R. Douglas, T. P. Downes, M. Drago, R. W. P. Drever, J. C. Driggers, Z. Du, M. Ducrot, S. E. Dwyer, T. B. Edo, M. C. Edwards, A. Effler, H.-B. Eggenstein, P. Ehrens, J. Eichholz, S. S. Eikenberry, W. Engels, R. C. Essick, Z. Etienne, T. Etzel, M. Evans, T. M. Evans, R. Everett, M. Factourovich, V. Fafone, H. Fair, S. Fairhurst, X. Fan, Q. Fang, S. Farinon, B. Farr, W. M. Farr, E. Fauchon-Jones, M. Favata, M. Fays, H. Fehrmann, M. M. Fejer, I. Ferrante, E. C. Ferreira, F. Ferrini, F. Fidecaro, I. Fiori, D. Fiorucci, R. P. Fisher, R. Flaminio, M. Fletcher, J.-D. Fournier, S. Franco, S. Frasca, F. Frasconi, Z. Frei, A. Freise, R. Frey, V. Frey, T. T. Fricke, P. Fritschel, V. V. Frolov, P. Fulda, M. Fyffe, H. A. G. Gabbard, S. M. Gaebel, J. R. Gair, L. Gammaitoni, S. G. Gaonkar, F. Garufi, A. Gatto, G. Gaur, N. Gehrels, G. Gemme, B. Gendre, E. Genin, A. Gennai, J. George, L. Gergely, V. Germain, A. Ghosh, S. Ghosh, J. A. Giaime, K. D. Giardina, A. Giazotto, K. Gill, A. Glaefke, E. Goetz, R. Goetz, L. Gondan, G. González, J. M. Gonzalez Castro, A. Gopakumar, N. A. Gordon, M. L. Gorodetsky, S. E. Gossan, M. Gosselin, R. Gouaty, C. Graef, P. B. Graff, M. Granata, A. Grant, S. Gras, C. Gray, G. Greco, A. C. Green, P. Groot, H. Grote, S. Grunewald, G. M. Guidi, X. Guo, A. Gupta, M. K. Gupta, K. E. Gushwa, E. K. Gustafson, R. Gustafson, J. J. Hacker, B. R. Hall, E. D. Hall, G. Hammond, M. Haney, M. M. Hanke, J. Hanks, C. Hanna, M. D. Hannam, J. Hanson, T. Hardwick, J. Harms, G. M. Harry, I. W. Harry, M. J. Hart, M. T. Hartman, C.-J. Haster, K. Haughian, J. Healy, A. Heidmann, M. C. Heintze, H. Heitmann, P. Hello, G. Hemming, M. Hendry, I. S. Heng, J. Hennig, A. W. Heptonstall, M. Heurs, S. Hild, D. Hoak, K. A. Hodge, D. Hofman, S. E. Hollitt, K. Holt, D. E. Holz, P. Hopkins, D. J. Hosken, J. Hough, E. A. Houston, E. J. Howell, Y. M. Hu, S. Huang, E. A. Huerta, D. Huet, "Properties of the binary black hole merger gw150914," *Phys. Rev. Lett.*, vol. 116, p. 241102, Jun 2016.

[23] N. J. Cornish and T. B. Littenberg, "Bayeswave: Bayesian inference for gravitational wave

bursts and instrument glitches," *Classical and Quantum Gravity*, vol. 32, no. 13, p. 135012, 2015.

[24] B. P. Abbott, R. Abbott, T. D. Abbott, M. R. Abernathy, F. Acernese, K. Ackley, C. Adams, T. Adams, P. Addesso, R. X. Adhikari, V. B. Adya, C. Affeldt, M. Agathos, K. Agatsuma, N. Aggarwal, O. D. Aguiar, L. Aiello, A. Ain, P. Ajith, B. Allen, A. Allocca, P. A. Altin, S. B. Anderson, W. G. Anderson, K. Arai, M. C. Araya, C. C. Arceneaux, J. S. Areeda, N. Arnaud, K. G. Arun, S. Ascenzi, G. Ashton, M. Ast, S. M. Aston, P. Astone, P. Aufmuth, C. Aulbert, S. Babak, P. Bacon, M. K. M. Bader, P. T. Baker, F. Baldaccini, G. Ballardin, S. W. Ballmer, J. C. Barayoga, S. E. Barclay, B. C. Barish, D. Barker, F. Barone, B. Barr, L. Barsotti, M. Barsuglia, D. Barta, J. Bartlett, I. Bartos, R. Bassiri, A. Basti, J. C. Batch, C. Baune, V. Bavigadda, M. Bazzan, B. Behnke, M. Bejger, A. S. Bell, C. J. Bell, B. K. Berger, J. Bergman, G. Bergmann, C. P. L. Berry, D. Bersanetti, A. Bertolini, J. Betzwieser, S. Bhagwat, R. Bhandare, I. A. Bilenko, G. Billingsley, J. Birch, R. Birney, S. Biscans, A. Bisht, M. Bitossi, C. Biwer, M. A. Bizouard, J. K. Blackburn, L. Blackburn, C. D. Blair, D. G. Blair, R. M. Blair, S. Bloemen, O. Bock, T. P. Bodiya, M. Boer, G. Bogaert, C. Bogan, A. Bohe, P. Bojtos, C. Bond, F. Bondu, R. Bonnand, B. A. Boom, R. Bork, V. Boschi, S. Bose, Y. Bouffanais, A. Bozzi, C. Bradaschia, P. R. Brady, V. B. Braginsky, M. Branchesi, J. E. Brau, T. Briant, A. Brillet, M. Brinkmann, V. Brisson, P. Brockill, A. F. Brooks, D. A. Brown, D. D. Brown, N. M. Brown, C. C. Buchanan, A. Buikema, T. Bulik, H. J. Bulten, A. Buonanno, D. Buskulic, C. Buy, R. L. Byer, L. Cadonati, G. Cagnoli, C. Cahillane, J. Calderón Bustillo, T. Callister, E. Calloni, J. B. Camp, K. C. Cannon, J. Cao, C. D. Capano, E. Capocasa, F. Carbognani, S. Caride, J. Casanueva Diaz, C. Casentini, S. Caudill, M. Cavaglià, F. Cavalier, R. Cavalieri, G. Cella, C. B. Cepeda, L. Cerboni Baiardi, G. Cerretani, E. Cesarini, R. Chakraborty, S. Chatterji, T. Chalermsongsak, S. J. Chamberlin, M. Chan, S. Chao, P. Charlton, E. Chassande-Mottin, H. Y. Chen, Y. Chen, C. Cheng, A. Chincarini, A. Chiummo, H. S. Cho, M. Cho, J. H. Chow, N. Christensen, Q. Chu, S. Chua, S. Chung, G. Ciani, F. Clara, J. A. Clark, M. Clark, F. Cleva, E. Coccia, P.-F. Cohadon, A. Colla, C. G. Collette, L. Cominsky, M. Constancio, A. Conte, L. Conti, D. Cook, T. R. Corbitt, N. Cornish, A. Corsi, S. Cortese, C. A. Costa, M. W. Coughlin, S. B. Coughlin, J.-P. Coulon, S. T. Countryman, P. Couvares, E. E. Cowan, D. M. Coward, M. J. Cowart, D. C. Coyne, R. Coyne, K. Craig, J. D. E. Creighton, J. Cripe, S. G. Crowder, A. Cumming, L. Cunningham, E. Cuoco, T. Dal Canton, S. L. Danilishin, S. D'Antonio, K. Danzmann, N. S. Darman, V. Dattilo, I. Dave, H. P. Daveloza, M. Davier, G. S. Davies, E. J. Daw, R. Day, D. DeBra, G. Debreczeni, J. Degallaix, M. De Laurentis, S. Deléglise, W. Del Pozzo, T. Denker, T. Dent, H. Dereli, V. Dergachev, R. T. DeRosa, R. De Rosa, R. DeSalvo, S. Dhurandhar, M. C. Díaz, L. Di Fiore, M. Di Giovanni, A. Di Lieto, S. Di Pace, I. Di Palma, A. Di Virgilio, G. Dojcinoski, V. Dolique, F. Donovan, K. L. Dooley, S. Doravari, R. Douglas, T. P. Downes, M. Drago, R. W. P. Drever, J. C. Driggers, Z. Du, M. Ducrot, S. E. Dwyer, T. B. Edo, M. C. Edwards, A. Effler, H.-B. Eggenstein, P. Ehrens, J. Eichholz, S. S. Eikenberry, W. Engels, R. C. Essick, T. Etzel, M. Evans, T. M. Evans, R. Everett, M. Factourovich, V. Fafone, H. Fair, S. Fairhurst, X. Fan, Q. Fang, S. Farinon, B. Farr, W. M. Farr, M. Favata, M. Fays, H. Fehrmann, M. M. Fejer, I. Ferrante, E. C. Ferreira, F. Ferrini, F. Fidecaro, I. Fiori, D. Fiorucci, R. P. Fisher, R. Flaminio, M. Fletcher, J.-D. Fournier, S. Franco, S. Frasca, F. Frasconi, Z. Frei, A. Freise, R. Frey, V. Frey, T. T. Fricke, P. Fritschel, V. V. Frolov, P. Fulda, M. Fyffe, H. A. G. Gabbard, J. R. Gair, L. Gammaitoni, S. G. Gaonkar, F. Garufi, A. Gatto, G. Gaur, N. Gehrels, G. Gemme, B. Gendre, E. Genin, A. Gennai, J. George, L. Gergely, V. Germain, A. Ghosh, S. Ghosh, J. A. Giaime, K. D. Giardina, A. Giazotto, K. Gill, A. Glaefke, E. Goetz, R. Goetz, L. Gondan, G. González,

J. M. Gonzalez Castro, A. Gopakumar, N. A. Gordon, M. L. Gorodetsky, S. E. Gossan, M. Gosselin, R. Gouaty, C. Graef, P. B. Graff, M. Granata, A. Grant, S. Gras, C. Gray, G. Greco, A. C. Green, P. Groot, H. Grote, S. Grunewald, G. M. Guidi, X. Guo, A. Gupta, M. K. Gupta, K. E. Gushwa, E. K. Gustafson, R. Gustafson, R. Haas, J. J. Hacker, B. R. Hall, E. D. Hall, G. Hammond, M. Haney, M. M. Hanke, J. Hanks, C. Hanna, M. D. Hannam, J. Hanson, T. Hardwick, J. Harms, G. M. Harry, I. W. Harry, M. J. Hart, M. T. Hartman, C.-J. Haster, K. Haughian, J. Healy, A. Heidmann, M. C. Heintze, H. Heitmann, P. Hello, G. Hemming, M. Hendry, I. S. Heng, J. Hennig, A. W. Heptonstall, M. Heurs, S. Hild, I. Hinder, D. Hoak, K. A. Hodge, D. Hofman, S. E. Hollitt, K. Holt, D. E. Holz, P. Hopkins, D. J. Hosken, J. Hough, E. A. Houston, E. J. Howell, Y. M. Hu, S. Huang, E. A. Huerta, D. Huet, B. Hughey, "Observing gravitational-wave transient gw150914 with minimal assumptions," *Phys. Rev. D*, vol. 93, p. 122004, Jun 2016.

[25] S. Chatterji, L. Blackburn, G. Martin, and E. Katsavounidis, "Multiresolution techniques for the detection of gravitational-wave bursts," *Classical and Quantum Gravity*, vol. 21, no. 20, p. S1809, 2004.

[26] D. V. Martynov, E. D. Hall, B. P. Abbott, R. Abbott, T. D. Abbott, C. Adams, R. X. Adhikari, R. A. Anderson, S. B. Anderson, K. Arai, M. A. Arain, S. M. Aston, L. Austin, S. W. Ballmer, M. Barbet, D. Barker, B. Barr, L. Barsotti, J. Bartlett, M. A. Barton, I. Bartos, J. C. Batch, A. S. Bell, I. Belopolski, J. Bergman, J. Betzwieser, G. Billingsley, J. Birch, S. Biscans, C. Biwer, E. Black, C. D. Blair, C. Bogan, R. Bork, D. O. Bridges, A. F. Brooks, C. Celerier, G. Ciani, F. Clara, D. Cook, S. T. Countryman, M. J. Cowart, D. C. Coyne, A. Cumming, L. Cunningham, M. Damjanic, R. Dannenberg, K. Danzmann, C. F. D. S. Costa, E. J. Daw, D. DeBra, R. T. DeRosa, R. DeSalvo, K. L. Dooley, S. Doravari, J. C. Driggers, S. E. Dwyer, A. Effler, T. Etzel, M. Evans, T. M. Evans, M. Factourovich, H. Fair, D. Feldbaum, R. P. Fisher, S. Foley, M. Frede, P. Fritschel, V. V. Frolov, P. Fulda, M. Fyffe, V. Galdi, J. A. Giaime, K. D. Giardina, J. R. Gleason, R. Goetz, S. Gras, C. Gray, R. J. S. Greenhalgh, H. Grote, C. J. Guido, K. E. Gushwa, E. K. Gustafson, R. Gustafson, G. Hammond, J. Hanks, J. Hanson, T. Hardwick, G. M. Harry, J. Heefner, M. C. Heintze, A. W. Heptonstall, D. Hoak, J. Hough, A. Ivanov, K. Izumi, M. Jacobson, E. James, R. Jones, S. Kandhasamy, S. Karki, M. Kasprzack, S. Kaufer, K. Kawabe, W. Kells, N. Kijbunchoo, E. J. King, P. J. King, D. L. Kinzel, J. S. Kissel, K. Kokeyama, W. Z. Korth, G. Kuehn, P. Kwee, M. Landry, B. Lantz, A. Le Roux, B. M. Levine, J. B. Lewis, V. Lhuillier, N. A. Lockerbie, M. Lormand, M. J. Lubinski, A. P. Lundgren, T. MacDonald, M. MacInnis, D. M. Macleod, M. Mageswaran, K. Mailand, S. Márka, Z. Márka, A. S. Markosyan, E. Maros, I. W. Martin, R. M. Martin, J. N. Marx, K. Mason, T. J. Massinger, F. Matichard, N. Mavalvala, R. McCarthy, D. E. McClelland, S. McCormick, G. McIntyre, J. McIver, E. L. Merilh, M. S. Meyer, P. M. Meyers, J. Miller, R. Mittleman, G. Moreno, C. L. Mueller, G. Mueller, A. Mullavey, J. Munch, L. K. Nuttall, J. Oberling, J. O'Dell, P. Oppermann, R. J. Oram, B. O'Reilly, C. Osthelder, D. J. Ottaway, H. Overmier, J. R. Palamos, H. R. Paris, W. Parker, Z. Patrick, A. Pele, S. Penn, M. Phelps, M. Pickenpack, V. Pierro, I. Pinto, J. Poeld, M. Principe, L. Prokhorov, O. Puncken, V. Quetschke, E. A. Quintero, F. J. Raab, H. Radkins, P. Raffai, C. R. Ramet, C. M. Reed, S. Reid, D. H. Reitze, N. A. Robertson, J. G. Rollins, V. J. Roma, J. H. Romie, S. Rowan, K. Ryan, T. Sadecki, E. J. Sanchez, V. Sandberg, V. Sannibale, R. L. Savage, R. M. S. Schofield, B. Schultz, P. Schwinberg, D. Sellers, A. Sevigny, D. A. Shaddock, Z. Shao, B. Shapiro, P. Shawhan, D. H. Shoemaker, D. Sigg, B. J. J. Slagmolen, J. R. Smith, M. R. Smith, N. D. Smith-Lefebvre, B. Sorazu, A. Staley, A. J. Stein, A. Stochino, K. A. Strain, R. Taylor, M. Thomas, P. Thomas, K. A. Thorne, E. Thrane, C. I. Torrie, G. Traylor, G. Vajente,

G. Valdes, A. A. van Veggel, M. Vargas, A. Vecchio, P. J. Veitch, K. Venkateswara, T. Vo, C. Vorvick, S. J. Waldman, M. Walker, R. L. Ward, J. Warner, B. Weaver, R. Weiss, T. Welborn, P. Weßels, C. Wilkinson, P. A. Willems, L. Williams, B. Willke, L. Winkelmann, C. C. Wipf, J. Worden, G. Wu, H. Yamamoto, C. C. Yancey, H. Yu, L. Zhang, M. E. Zucker, and J. Zweizig, "Sensitivity of the advanced ligo detectors at the beginning of gravitational wave astronomy," *Phys. Rev. D*, vol. 93, p. 112004, Jun 2016.

[27] J. Veitch, V. Raymond, B. Farr, W. Farr, P. Graff, S. Vitale, B. Aylott, K. Blackburn, N. Christensen, M. Coughlin, W. Del Pozzo, F. Feroz, J. Gair, C.-J. Haster, V. Kalogera, T. Littenberg, I. Mandel, R. O'Shaughnessy, M. Pitkin, C. Rodriguez, C. Röver, T. Sidery, R. Smith, M. Van Der Sluys, A. Vecchio, W. Vousden, and L. Wade, "Parameter estimation for compact binaries with ground-based gravitational-wave observations using the lalinference software library," *Phys. Rev. D*, vol. 91, p. 042003, Feb 2015.

[28] M. S. Z. Marlan O. Scully, *Quantum Optics.* Cambridge University Press, 1997.

[29] T. C. R. Hans-A. Bachor, ed., *A Guide to Experiments in Quantum Optics, Second Edition.* WILEY-VCH Verlag GmbH & Co. KGaA, 2008.

[30] W. Heisenberg, "Über den anschaulichen inhalt der quantentheoretischen kinematik und mechanik," *Zeitschrift für Physik*, vol. 43, no. 3, pp. 172–198, 1927.

[31] P. A. Franken, A. E. Hill, C. W. Peters, and G. Weinreich, "Generation of optical harmonics," *Phys. Rev. Lett.*, vol. 7, pp. 118–119, Aug 1961.

[32] R. W. Boyd, *Nonlinear Optics - Third edition.* Academic Press - Elsevier, 2007.

[33] R. E. Slusher, L. W. Hollberg, B. Yurke, J. C. Mertz, and J. F. Valley, "Observation of squeezed states generated by four-wave mixing in an optical cavity," *Phys. Rev. Lett.*, vol. 55, pp. 2409–2412, Nov 1985.

[34] L.-A. Wu, H. J. Kimble, J. L. Hall, and H. Wu, "Generation of squeezed states by parametric down conversion," *Phys. Rev. Lett.*, vol. 57, pp. 2520–2523, Nov 1986.

[35] H.-X. Miao, *Exploring Macroscopic Quantum Mechanics in Optomechanical Devices.* PhD thesis, Western Australia U., 2010.

[36] W. Unruh, *Quantum Optics, Experimental Gravitation and Measurement Theory.* Plenum, 1982.

[37] B. Eric, "Notes on the pound-drever-hall technique," 1998.

[38] K. McKenzie, M. B. Gray, P. K. Lam, and D. E. McClelland, "Technical limitations to homodyne detection at audio frequencies," *Appl. Opt.*, vol. 46, pp. 3389–3395, Jun 2007.

[39] K. Schneider, M. Bode, I. Freitag, S. Schiller, and J. Mlynek, "1.1-w single-frequency 532-nm radiation by second-harmonic generation of a miniature nd:yag ring laser," *Opt. Lett.*, vol. 21, pp. 1999–2001, Dec 1996.

[40] L. collaboration, "Document g1300967-v1: Geo600 squeezer status. lvc meeting," September 2013.

[41] S. Wang, *Fabrication and characterization of periodically-poled KTP and Rb-doped KTP for applications in the visible and UV* . PhD thesis, Stockholm, Royal Institute of Technology, 2005.

[42] A. Khalaidovski, *Beyond the Quantum Limit.* PhD thesis, Hannover, Max Planck Inst. Grav., 2011.

[43] W. J. Kozlovsky, C. D. Nabors, and R. L. Byer, "Efficient second harmonic generation of a diode-laser-pumped cw nd: yag laser using monolithic mgo: linbo/sub 3/external resonant cavities," *Quantum Electronics, IEEE Journal of*, vol. 24, no. 6, pp. 913–919, 1988.

[44] E. S. Polzik and H. J. Kimble, "Frequency doubling with knbo3 in an external cavity," *Opt. Lett.*, vol. 16, pp. 1400–1402, Sep 1991.

[45] V. Akulov, S. Babin, S. Kablukov, and K. Raspopin, "Intracavity frequency doubling of yb-doped fiber laser with 540-550 nm tuning," *Laser Physics*, vol. 21, no. 5, pp. 935–939, 2011.

[46] G. D. Boyd and D. A. Kleinman, "Parametric interaction of focused gaussian light beams," *Journal of Applied Physics*, vol. 39, no. 8, pp. 3597–3639, 1968.

[47] Y. Qu and S. Singh, "Second-harmonic generation and photon bunching in multimode laser beams," *Phys. Rev. A*, vol. 47, pp. 3259–3263, Apr 1993.

[48] K. Kato and E. Takaoka, "Sellmeier and thermo-optic dispersion formulas for ktp," *Appl. Opt.*, vol. 41, pp. 5040–5044, Aug 2002.

[49] A. Ashkin, G. Boyd, and J. Dziedzic, "Resonant optical second harmonic generation and mixing," *Quantum Electronics, IEEE Journal of*, vol. 2, pp. 109–124, Jun 1966.

[50] R. L. Sutherland, *Handbook of Nonlinear Optics.* CRC Press, 2003.

[51] A. G. White, P. K. Lam, M. S. Taubman, M. A. M. Marte, S. Schiller, D. E. McClelland, and H.-A. Bachor, "Classical and quantum signatures of competing $\chi^{(2)}$ nonlinearities," *Phys. Rev. A*, vol. 55, pp. 4511–4515, Jun 1997.

[52] E. Khazanov, *Advances in Solid-State Lasers: Development and Applications. Chapter 3.* Mikhai, 2010.

[53] N. P. Barnes and L. B. Petway, "Variation of the verdet constant with temperature of terbium gallium garnet," *J. Opt. Soc. Am. B*, vol. 9, pp. 1912–1915, Oct 1992.